

2013

Advances in Heat Transfer Through Coatings and Micro-scale Features

Richard William Bonner
Lehigh University

Follow this and additional works at: <http://preserve.lehigh.edu/etd>

 Part of the [Chemical Engineering Commons](#)

Recommended Citation

Bonner, Richard William, "Advances in Heat Transfer Through Coatings and Micro-scale Features" (2013). *Theses and Dissertations*. Paper 1432.

This Dissertation is brought to you for free and open access by Lehigh Preserve. It has been accepted for inclusion in Theses and Dissertations by an authorized administrator of Lehigh Preserve. For more information, please contact preserve@lehigh.edu.

Advances in Heat Transfer Through Coatings and
Micro-scale Features

by

Richard W. Bonner III

A Dissertation

Presented to the Graduate and Research Committee

of Lehigh University

in Candidacy for the Degree of

Doctor of Philosophy

in

Chemical Engineering

Lehigh University

May 2013

Certificate of Approval

Approved and recommended for acceptance as a dissertation in partial fulfillment of the requirements for the degree of Doctor of Philosophy.

Acceptance Date

Manoj K. Chaudhury
Dissertation Advisor/Committee Chair
Franklin J. Howes Jr. Distinguished
Professor of Chemical Engineering

Other Committee Members:

Kemal Tuzla
Associate Chair of the Department of
Chemical Engineering, Professor of Practice

Jeetain Mittal
P.C. Rossin Assistant Professor of Chemical
Engineering

Mayuresh Kothare
R. L. McCann Professor and Chair of
Chemical Engineering

Zhijun Jon Zuo
President and CTO of Advanced Cooling
Technologies, Inc.

Acknowledgements

There are several people from Lehigh University who I need to thank, starting with Prof. Manoj Chaudhury. Science aside, I am most grateful for his patience in allowing me the opportunity to pursue this degree while working and starting a family. I will especially appreciate his insistence on developing an "old school" model for my dropwise condensation correlation. I also can't forget Prof. John Chen and Prof. Kemal Tuzla, who started me on this path as an undergraduate research assistant and shaped my development through my Master's degree. I would also like to thank my other committee members, Prof. Mayuresh Kothare and Prof. Jeetain Mittal for their input as the work progressed.

I could not have finished the work without the fantastic support from my colleagues at Advanced Cooling Technologies. Special thanks to Jon Zuo for encouraging me to pursue this endeavor and serving on my committee. I would also like to thank a list of people who supported the fabrication, innovation, and various other parts of this effort, including Jesse Campbell, Jens Weyant, Angie Fan, Bill Napier, and Tapan Desai.

I could also have not performed this work without the support of my sponsors, including the National Science Foundation, National Reconnaissance Office, Defense Advanced Projects Research Agency, Navy, Intel, and Oracle.

Dedication

This thesis is dedicated to my wife, Jeanine, and our daughter, Theta, whose love, motivation, and patience allowed me the opportunity to pursue my doctorate in Chemical Engineering.

Table of Contents

Certificate of Approval	ii
Acknowledgements	iii
Dedication	iv
Table of Contents	v
List of Figures	ix
Abstract	1
Chapter 1 Introduction	4
1.1 Motivation for the Current Research	4
1.2 Review	6
<i>1.2.1 Dropwise Condensation.....</i>	<i>6</i>
<i>1.2.2 Self-Assembled Monolayer Coatings</i>	<i>7</i>
1.3 Applications	9
1.4 Synopsis	11
Part I Dropwise Condensation	14
Chapter 2 Condensation on Gradient Surfaces Experiments	15
2.1 Background and Introduction	15
2.2 Fabrication of Test Articles and Surface Preparation	17
2.3 Thermal Performance Testing.....	23
2.4 Conclusions and Future Work	29

Chapter 3 Hydrophobic Wick Structures Experiments.....	31
3.1 Background and Introduction	31
3.2 Nomenclature	33
3.3 Mechanism for Condensing on Wick Structures	33
3.4 Wick and Surface Preparation	36
3.5 Test Apparatus	40
3.6 Thermal Performance Testing.....	43
3.6.1 <i>Passive Loop System with Water</i>	44
3.6.2 <i>Pumped Loop System with Water</i>	46
3.6.3 <i>Passive Loop System with Methanol</i>	48
3.7 Conclusions and Future Work	49
Chapter 4 Heat Transfer Coefficient Modeling	51
4.1 Background and Introduction	51
4.2 Nomenclature	52
4.3 Introduction.....	53
4.4 Le Fevre and Rose Theory	57
4.5 Bonner Model	60
4.6 Comparison to Data	65
4.7 Surface Inclination	71
4.8 Considering the Promoter Resistance	73

4.9 Wettability or Surface Energy Gradients	74
4.10 Conclusions and Future Work	79
Chapter 5 Practical Applications of Dropwise Condensation.....	81
5.1 Vapor Chambers	82
5.2 Life Testing and Reliability	86
5.3 Conclusions and Future Work	88
Part II Micro- and Nano-scale Heat Transfer Topics.....	89
Chapter 6 Micro-channel Corrosion Prevention	90
6.1 Overview	90
6.2 Background Reliability Issues in Micro-channel Coolers	90
6.3 Corrosion and Erosion Mechanisms	92
6.4 Atomic Layer Deposition.....	94
6.5 Self-Assembled Monolayers	97
6.6 Coating Identification	99
6.7 Erosion, Corrosion, Thermal Cycling Experimental Results.....	99
6.8 Conclusions and Future Work	102
Chapter 7 Die Level Thermal Storage	105
7.1 Overview	106
7.2 Introduction.....	107
7.3 Background.....	108

7.4 Macroscale Finite-Element Analysis Modeling.....	110
7.5 Atomistic-Scale Modeling	114
7.5 Parasitic Capacitance Modeling.....	118
7.6 Conclusions and Future Work	122
Chapter 8 Jet Impingement of Flat Angled Sprays.....	123
8.1 Overview.....	123
8.2 Nomenclature	123
8.3 Background and Introduction	124
8.4 Modeling of Local Heat Transfer Coefficients with Flat Angled Sprays.....	126
8.5 Test Setup and Thermal Test Vehicle.....	129
8.6 Experimental Data	131
8.7 Conclusions and Future Work	136
Bibliography	138
Appendix A	138
Biography.....	158
Curriculum Vitae	159

List of Figures

- Figure 1.1**8
Illustration of non-wetting surface preparation using self-assembled monolayer technique. While one end of the molecule chemically reacts with the surface, the hydrophobic (non-wetting) side of the molecule points away from the surface creating a surface that is entirely non-wetting.
- Figure 2.1**16
The physics of droplet motion on a chemically induced surface gradient is illustrated. A constant supply of liquid droplets is supplied uniformly by condensation on the gradient surface. The droplets move towards the more hydrophilic region of the gradient surface due to the difference in contact angle experienced by opposing sides of the droplets.
- Figure 2.2**17
The fabrication of a chemically induced surface gradient is illustrated. Organosilanes are short polymer molecules of which one end reacts with a silicon surface and the other end can possess a desirable surface characteristic, in this case a low surface energy molecule is desired. These molecules are bonded in a diffusion controlled reaction to create a variation in concentration and therefore surface energy on a surface. Liquid droplets formed by condensation on the surface gradient will move towards the better wetting region.
- Figure 2.3**21
Photograph of water droplet on a polished copper surface that has been prepared with 1-octadecyl mercaptan, causing the surface to be hydrophobic.

Figure 2.4	22
A Photograph of the assembled test section is shown.	
Figure 2.5	24
Shows a side view of the test section. Thermocouples inserted in the 9 holes are used to measure the heat flux and surface temperature of the condensing surface. A gap was also machined to prevent heat from leaking in through the vapor/liquid ports.	
Figure 2.6	25
This figure shows the various orientations to be tested including the vertical (A), 45° angle (B), horizontal (C), against gravity (D).	
Figure 2.7	25
A plot of experimental measured heat transfer coefficient results for a non-wetting, gradient and wetting surface in the vertical orientation (Figure 2.6A) are shown. The filmwise data compared well to the Nusselt model, validating the acquired data from the test section.	
Figure 2.8	26
A plot of experimental measured heat transfer coefficient results for a non-wetting, gradient and wetting surface in the 45° orientation (Figure 2.6B) are shown. Performance degraded much more rapidly with the non-wetting surface as compared to the gradient.	
Figure 2.9	27
A plot of experimental measured heat transfer coefficient results for a gradient in the horizontal orientation (Figure 2.6C) are shown. The non-wetting and wetting surfaces flooded as liquid was not able to return to the boiling section.	

Figure 2.10	28
A plot of experimental measured heat transfer coefficient results for a gradient tilted 5° against gravity (Figure 2.6D) are shown. The non-wetting and wetting surfaces flooded as liquid was not able to return to the boiling section.	
Figure 3.1	35
Illustration of dropwise condensation promotion using non-wetting metal wick. Droplets remain in the wick as they grow (1) and coalesce (2). (3) Eventually the droplet grows match the radius of the wick. (4) Further growth forces the bubble into a non-spherical shape with two effective radii. (5) The Laplace pressure gradient causes by the two differing radii pushes the droplet out of the wick into the vapor core.	
Figure 3.2	37
Illustration of self-assembled monolayer surface preparation technique on a porous wick structure. The molecules with envelope the wick and wall, creating a non-wetting surface on all locations of the wick and wall.	
Figure 3.3	38
Photographs of a layer powder sintered onto test blocks.	
Figure 3.4	39
Photograph of water droplet on one layer of powder after treatment of the surface with a self assembled monolayer of hydrophobic octadecyl mercaptan.	
Figure 3.5	39
A droplet of a fluorinert (3m Novec Fluid HFE-72DE) is placed on a polished copper surface that has been prepared with a fluorinate self assembled monolayer. The contact angle is less than 10° .	

Figure 3.6	39
A droplet of methanol is placed on a polished copper surface that has been prepared with a fluorinate self-assembled monolayer. The contact angle is roughly 40°.	
Figure 3.7	43
A solids model picture of the passive flow loop test section is shown.	
Figure 3.8	43
A solids model picture of the pumped flow loop test section is shown.	
Figure 3.9	45
Experimental data for six test articles is shown: filmwise, dropwise on polished surface, dropwise on sintered fine powder surface, dropwise on sintered coarse powder surface, dropwise on single layer screen surface, and dropwise on double layer screen surface. Filmwise data is also compared to Nusselt condensation model.	
Figure 3.10	47
The heat transfer performance of the dropwise test articles versus the baseline filmwise test article with different flow rates are plotted.	
Figure 3.11	49
Experimental data for non-wetting polished test articles tested with water and with methanol. The saturation temperature was maintained at 100°C for water system and 70°C for methanol system.	
Figure 4.1	67
The relative heat flux contribution for all droplets of a given radius as a function of droplet radius as predicted by the Le Fevre and Rose model is plotted. The relative heat flux contribution of only the conduction and only the interfacial resistance is also plotted.	

The intersection of the two lines graphically depicts r_i . The Bonner model is derived by estimating that the maximum relative heat flux occurs at the droplet radius where the conduction and interface resistances are equal. The Bonner model also assumes that the relative heat flux contributed by droplets larger than r_i and smaller than r_i , are approximately equal. Therefore, the total dropwise condensation heat flux should be proportional to the value of either half of the integral.

Figure 4.268

Experimental heat transfer coefficients averaged with respect to heat flux (for data acquired at constant temperature) are plotted against a term in non heat flux dependent Bonner model with n equal to $2/3$. The slope of the regression line is equal to the dropwise condensation Nusselt number for the non heat flux dependent Bonner Model.

Figure 4.369

Experimental heat transfer coefficient data are plotted against a term in the non-heat flux dependent Bonner Model (similar to Figure 4.2, with all of the data, rather than averaged data plotted).

Figure 4.470

Experimental heat transfer coefficients are plotted against the term in the heat flux dependent Bonner model with m equal to $1/2$ [30][31]. The slope of the line is equal to the dropwise condensation Nusselt number for the heat flux dependent Bonner model.

Figure 4.572

Comparison of the derived $g \sin \phi^{1/3}$ term in the non-heat flux dependent Bonner model (Eq. 4.22) and the $g \sin \phi^{1/4}$ term used in the heat flux dependent Bonner model (Eq.

4.23) to relative (to completely vertical) heat transfer coefficient data acquired at various inclinations by Koch [32].

Figure 4.677

Gradient Data Horizontal versus Heat Flux

Figure 4.779

Gradient Data Versus Inclination

Figure 5.182

Droplets were placed at multiple locations on the vapor chamber lid to test for hydrophobicity.

Figure 5.283

A solid model showing the location of thermocouple required to measure the surface temperature and heat flux (through conduction calorimetry) are shown. Also shown is a thermocouple in the fluid space to measure the saturated fluid temperature.

Figure 5.384

A solid model of the tested 5.08cm by 5.08cm vapor chamber is shown.

Figure 5.485

Gravity aided condensation heat transfer coefficient data for a vapor chamber with a dropwise condensation surface is shown. Filmwise data are also compared to predictions from the Nusselt model for filmwise condensation.

Figure 5.587

Life test data for copper and gold surfaces prepared with SAM's are shown.

Figure 6.194

Schematic of turbulent eddy mechanism for downstream undercutting of erosion-

corrosion pits [51]. Defects in the coating surface allow turbulent eddies to form (a), which results in undercutting of the protective films (B-D).

Figure 6.296

Atomic Layer Deposition Process of Al₂O₃. For Al₂O₃-ALD to begin, the substrate must be prepared with OH groups (A). The first reaction in Al₂O₃-ALD uses Al(CH₃)₃ (B), which reacts with the hydroxyl groups and releases CH₄ (C). The second reaction in Al₂O₃-ALD uses water vapor (D). The water reacts with the remaining methyl groups, releasing more methane, and restores the surface chemistry to the initial OH condition (E).

Figure 6.3100

Illustration of coating: alumina coating deposited on a self assembled monolayer on a gold plated copper surface

Figure 6.4101

Illustration corrosion and erosion test apparatus.

Figure 6.5101

Illustration of corrosion test article.

Figure 6.6102

Thermal cycling results for copper and alumina coated samples.

Figure 6.7103

Results for corrosion testing of baseline copper samples are shown. The top left picture is before testing, the others are post testing.

Figure 6.8	103
Results for corrosion testing of gold plated samples are shown. The top left picture is before testing, the others are post testing.	
Figure 6.9	104
Results for corrosion testing of alumin (by ALD) on gold plated samples are shown. The top left picture is before testing, the others are post testing.	
Figure 7.1	110
Thermal model of a GaN Transistor Unit Cell with a PCM groove structure.	
Figure 7.2	111
Transient heat flux boundary condition.	
Figure 7.3	113
Transient thermal result for GaN device under pulsed operating conditions with and without PCM.	
Figure 7.4	114
Thermal result demonstrating increased power dissipation at constant maximum junction temperature.	
Figure 7.5	116
Density profile for a Si and In interface [63].	
Figure 7.6	117
Snapshot of silicon-indium atoms at 500K. The red strip represents the hot slab where energy is supplied and the cold strip where equal amount of energy is removed.	
Figure 7.7	118
Temperature profile across the simulation cell in the z-direction.	

Figure 7.8	119
Mesh result and material identification for electrostatic potential calculation.	
Figure 7.9	120
Normalized electrostatic potential for baseline case (without PCM).	
Figure 7.10	120
Normalized electrostatic potential for case with PCM.	
Figure 7.11	121
Parasitic capacitances for the source and drain are tabulated for the baseline case (no PCM) and PCM as a function of distance.	
Figure 7.12	121
Parasitic capacitances for the between the pad and PCM are tabulated.	
Figure 8.1	126
A diagram illustrating the spray cooling system studied in this paper is shown. Liquid exits an array of nozzles forming a flat spray. The spray impacts the surface of the silicon chip (shown as semi-transparent) at an angle to the surface, directly on the edge of the chip. The chip itself is held in place by a metal clamp, not shown.	
Figure 8.2	130
Photograph showing spray cooling system hardware. Not shown is the thermal test vehicle which sits above the nozzle arrays centered between the arrays. There is also a plate which created a liquid tight seal around the cooling solution and test vehicle.	
Figure 8.3	133
Summary plot of experimental local heat transfer coefficients for all three fluids. The highest heat transfer coefficients were measured for water. Methanol heat transfer	

coefficients were higher than that of HFE-7000 at the impact zone, but matched those of HFE-7000 near the end of the chip surface.

Figure 8.4134

Diagram illustrating the impact region location of the spray on the chip surface and direction of resulting flow. The coordinates referred to in Figure 8.3, Figure 8.5, Figure 8.6, and Figure 8.7 are also indicated.

Figure 8.5135

Local spray cooling data for water are shown, illustrating the decrease in heat transfer coefficient as a function of length. Comparison to model predictions is also shown.

Figure 8.6135

Local spray cooling data for methanol are shown, illustrating the decrease in heat transfer coefficient as a function of length. Comparison to model predictions is also shown.

Figure 8.7136

Local spray cooling data for HFE-7000 are shown, illustrating the decrease in heat transfer coefficient as a function of length. Comparison to model predictions is also shown.

Figure A.1146

Predictions from the heat flux and non-heat flux dependent Bonner models are plotted against experimental data acquired by Stylianou for steam at 374 K [30].

Figure A.2147

Predictions from the heat flux and non-heat flux dependent Bonner models are plotted against experimental data acquired by Stylianou for steam at 366 K [30].

Figure A.3	148
Predictions from the heat flux and non-heat flux dependent Bonner models are plotted against experimental data acquired by Stylianou for steam at 359 K [30].	
Figure A.4	149
Predictions from the heat flux and non-heat flux dependent Bonner models are plotted against experimental data acquired by Stylianou for steam at 348 K [30].	
Figure A.5	150
Predictions from the heat flux and non-heat flux dependent Bonner models are plotted against experimental data acquired by Stylianou for steam at 333K [30].	
Figure A.6	151
Predictions from the heat flux and non-heat flux dependent Bonner models are plotted against experimental data acquired by Stylianou for steam at 321 K [30].	
Figure A.7	152
Predictions from the heat flux and non-heat flux dependent Bonner models are plotted against experimental data acquired by Utaka for ethylene glycol at 428 K [31].	
Figure A.8	153
Predictions from the heat flux and non-heat flux dependent Bonner models are plotted against experimental data acquired by Utaka for propylene glycol at 408 K [31].	
Figure A.9	154
Predictions from the heat flux and non-heat flux dependent Bonner models are plotted against experimental data acquired by Utaka for propylene glycol at 388 K [31].	

Figure A.10	155
Predictions from the heat flux and non-heat flux dependent Bonner models are plotted against experimental data acquired by Utaka for ethylene glycol at 368 K [31].	
Figure A.11	156
Predictions from the heat flux and non-heat flux dependent Bonner models are plotted against experimental data acquired by Utaka for propylene glycol at 363 K [31].	
Figure A.12	157
Predictions from the heat flux and non-heat flux dependent Bonner models are plotted against experimental data acquired by Utaka extracted data for glycerol at 423 K [31].	

Abstract

For most of the twentieth century, advanced heat transfer research was geared towards solving the two-phase flow and thermal problems of the nuclear, chemical, and materials processing industries that emerged near the start and middle of the century. These applications demanded relatively large scale systems, with scale up being the challenge of the day. At these power levels and length scales, understanding the interactions between the respective shear, momentum, and body forces of the vapor and liquid were of critical importance. Fast forward to the end of the twentieth century and start of the twenty-first century, and advanced thermal research has shifted towards solving the "smaller" problems of the electronics cooling industry with scale down being the challenge of the day. In large, many of the benefits associated with two-phase heat transfer at these smaller length scales are consistent with the high convection coefficients and lower flow rate requirements observed at larger length scales.

Understanding two-phase heat transfer at these smaller length scales requires the understanding of the same macro-scale two-phase heat transfer physics along with additional physics such as capillary forces and wetting phenomenon. Perhaps this is most evident in heat pipes, where two-phase heat transfer in combination with capillary wick structures have emerged as a staple in the electronics cooling community. Increasing power density requirements have pushed the use of monolithic hydrophilic wick structures used in commodity heat pipes to their limits, including their power transport capabilities and their convection thermal resistances. One way to improve upon traditional wick structures is to manipulate large droplets on hydrophobic surfaces in the condenser portion of heat pipes. Fluid can be circulated more readily as a droplet on a

surface compared with fluid through small pores. Further, the convection resistance associated with dropwise condensation is an order of magnitude better than condensation on a hydrophilic wick structure. Surfaces with graded hydrophobicity have shown to be capable of passively moving condensing droplets while exhibiting the characteristic high heat transfer coefficient of dropwise condensation on hydrophobic surfaces.

Vapor-liquid two-phase heat transfer alone cannot solve all modern thermal problems. The electronics community has pushed transistor sizes to the nano-scale feature size levels, where more complicated physics such as phonon-phonon and electron-phonon interactions are required to understand heat transfer physics and engineer solutions at these levels. For communications applications where the chips operate in pulsed modes, thermal storage through freeze-thaw cycles of a solid-liquid phase change material is an attractive solution. However, the thermal storage effect at high pulse frequencies is only warranted if the phase change material is located in close proximity, within a few microns, of the active transistors where electron-phonon and phonon-phonon interactions dominate conventional Fourier conduction thermal resistances.

In high power density systems operating at 1,000's of W/cm^2 heat fluxes, such as high power laser diodes, compact micro-channel coolers using single phase coolants have emerged as a potentially viable cooling solution. The laminar flow and heat transfer physics involved in these devices are well understood. However, the compact nature of the micro-channel coolers along with the high flow rates needed to remove the required power have led to unavoidably high velocities. Copper is the only engineering material with thermal conductivities high enough to meet thermal performance requirements, but

suffers from erosion at the high velocities required. Meanwhile, ceramic thin films have the necessary properties to limit erosion under the high velocities required. Although conventional fabrication techniques cannot be used to apply ceramic coatings within the small micro-channel features, nano-scale coating methodologies such as Atomic Layer Deposition may hold the key to meeting the application demands.

Thermal testing at smaller length scales poses measurement challenges that are under development. One such challenge is encountered by CPU manufacturers during their development process, where optical inspection of active transistors is required while operating. The CPU dissipates heat at a rate equivalent to normal operation in these tests. The optical view requirement removes the possibility of using traditional heat sinks to remove this waste heat. The only way to remove heat and meet the optical view requirement is to use impingement cooling. The small sizes of the so called "fireball" processing cores push the limits of the measurement technology used to validate cooling solutions.

Interdisciplinary research is the key to meeting many emerging research challenges, thermal management included. The twenty-first century has brought a new set of thermal challenges, pushed largely by the demands of the electronic industry. This thesis addresses several of those challenges, where interdisciplinary research involving heat transfer, surface engineering, and small length scales are a common theme.

Chapter 1

Introduction

1.1 Motivation for the Current Research

The work performed in this dissertation can certainly not be attributed to one source of inspiration and probably not even two. My first exposure to Heat Transfer was in an undergraduate class taught by Prof. John Chen. I still remember in one of the last lectures of the semester long class, Prof. Chen played a movie showing condensing droplets moving on a gradient surface. I didn't know at that time or even after Prof. Chaudhury showed the exact same movie again in his Colloids and Surface Chemistry class a few semesters later, that I would have the opportunity to extend the work half a decade later. I found employment at Advanced Cooling Technologies, Inc. after finishing my master's level coursework, which has exposed me to a litany of advanced research and practical thermal management experiences. Through these experiences I was able to connect the academic research presented to me by Prof. Chen and Prof. Chaudhury during my undergraduate experiences with the need for enhanced condensation surfaces that I was experiencing from customers seeking help with electronics cooling issues. However, many questions about the technology remained before the technology could be implemented in practical applications, including: what is the life of the coatings, how far can droplets be moved uphill using gradient surfaces under condensation conditions, how is the heat transfer performance affected by gravity, and can dropwise condensation heat transfer be predicted for various operating conditions?

The collection of research problems investigated in Part II of the dissertation was primarily motivated by the application needs of the creative electronics and photonics engineers who continue to cram heat generating transistors and devices into smaller package sizes with what seems to be complete disregard for removal of the excess waste heat. The solutions to these problems were motivated by the collection of engineers at Advanced Cooling Technologies, Inc., and their openness in brainstorming sessions, discussions, and sharing of their knowledge and experiences. The passivation coating work was motivated by a Defense Advanced Research Projects Agency (DARPA) solicitation requesting solutions to erosion and corrosion problems in micro-channel coolers. Discussions with Jens Weyant had us wondering if ceramic coating deposited by Atomic Layer Deposition could be the solution. Can we perform ALD on copper? Will there be coefficient of thermal expansion issues? Will the initial water layers adsorb on the copper surface and conform to the micro-channels?

The die level thermal storage work was proposed to a National Reconnaissance Office (NRO) funded effort to investigate junction level cooling. The solicitation did not request cooling of transistors operating in pulsed mode. However, other customers interactions exposed situations where even though chips were often rated for steady state power, the transistors cycle very frequently causing high temperature spikes in locations in close proximity to the active transistors. In this instance, the concept of using phase change materials embedded at the die level was motivated by intimate the knowledge of the application needs. Necessity is indeed the mother of invention.

Impingement cooling has long been investigated for applications where relatively large high flux surfaces are cooled. What happens when a thin, small "fireball" heat

sources require impingement cooling by multiple streams? This is just what Intel engineers George Popov and Robert Wadell needed answered when they needed to impingement cool a silicon chip with 0.25mm^2 CPU's operating at $1000\text{W}/\text{cm}^2$ heat fluxes. To these design requirements in perspective, if the chips lost cooling for even a split second, the CPU temperatures would increase several hundred degrees. How does the temperature vary along the surface? How with the CPU temperatures change with time when using these turbulent impingement flows?

1.2 Review

This section contains a review of general content that is applicable to multiple chapters in the dissertation. The dropwise condensation review pertains to all chapters in Part I of the dissertation. A review is also provided at the start of each chapter in Part I where additional specific material is available. A background on self-assembled monolayer coatings is provided, since this research covers the dropwise condensation research performed in chapters 2, 3, and 5 of Part I and the passivation coatings investigated in chapter 6 of Part II.

1.2.1 Dropwise Condensation

For the past 60 years dropwise condensation has been studied for its ability to produce heat transfer coefficients an order of magnitude higher than filmwise condensation [1]. Dropwise condensation occurs on a surface when the surface energy of the condensing surface is low enough to inhibit wetting of the surface by the condensing fluid. On these so called "hydrophobic" (when the fluid is water) or "oleophobic" (when the fluid is a low surface tension oil or refrigerant) surfaces, the condensing fluid forms liquid droplets on the condensing surface. In filmwise condensation, the condensing fluid

wets the relatively high surface energy condensing surfaces creating a thin continuous film of liquid [2]. On these so called "hydrophilic" surfaces, the heat transfer to the condensing surface is many times lower, as the continuous liquid film acts as an insulator. In dropwise condensation modes, the droplets coalescence process keep the droplet sizes small (compared to the film thickness in filmwise condensation) over the majority of the surface, creating regions of high heat transfer. Although portions of the dropwise condensation surface are covered by large droplets (much larger than the film thickness in filmwise condensation), the small droplets transfer the majority of the power at an overall lower thermal resistance since the smaller size droplets transfer heat in parallel with the large droplets.

The ability of dropwise condensation to increase heat transfer coefficients over film condensation is well established. The continuing research in this topic is inspired by economic incentives attainable if the heat transfer coefficients of dropwise condensation can be sustained [3]. However, only recently have researchers been able to create surfaces which can maintain their properties and sustain the dropwise condensation mode over time [4]. Failure of the low surface energy coatings ultimately causes filmwise condensation to occur since the exposed surfaces are generally high in surface energy.

1.2.2 Self-Assembled Monolayer Coatings

Generally, self-assembled monolayers (SAM) are a family of coatings that spontaneously form one molecular layer thick coatings. The chemicals used in preparation consist of short polymer chains with one of the terminal end groups having reactive properties capable of forming a chemical bond with a surface. The other end group is engineered to have a desirable surface property, such as low surface energy.

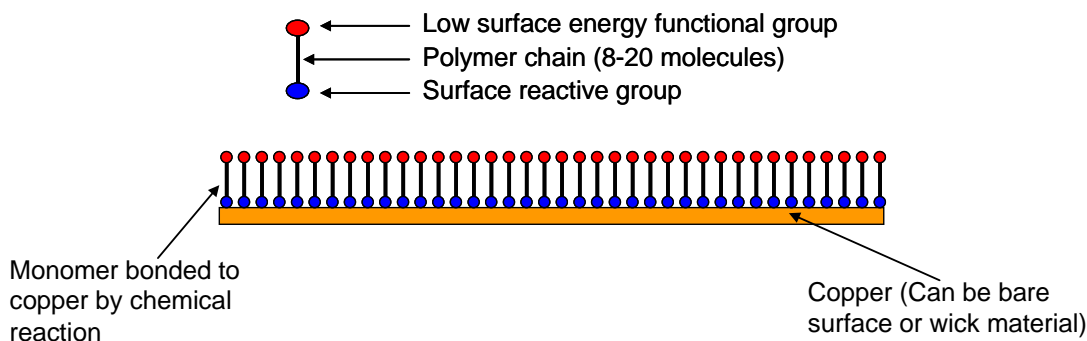


Figure 1.1 Illustration of non-wetting surface preparation using self-assembled monolayer technique. While one end of the molecule chemically reacts with the surface, the hydrophobic (non-wetting) side of the molecule points away from the surface creating a surface that is entirely non-wetting.

The surface preparation technique involves chemically reacting a molecule with a short polymer chain to a surface as demonstrated in Figure 1.1. The chemicals used in these types of surface preparations are typically polymer chains approximately 8-20 molecules long [5]. On one side of the polymer chain is a reactive functional group, capable of forming a chemical bond with a surface. In all of this research a thiol (-SH) functional group capable of creating a chemical bond with copper was used, although other materials such as gold and silver can be coated with thiols. Other end groups are also available to bond to other materials, with silicon and silane being one of the more popular tandems. It should be pointed out that the “coating” used in this process is more than just paint, as the chemical bond between the molecule and the metal surface is of a permanent nature. Since only one of the functional groups on the polymer chains reacts with the surface while the other functional group is non-reactive, the molecules tend to self-assemble on the surface, creating a layer of molecules that is one layer thick as

illustrated in Figure 1.1. The result is a surface which is chemically altered possessing only the surface properties of the functional end group of the molecule.

In the dropwise condensation research, low surface energy surfaces were desired. Surfaces with low energy are considered hydrophobic or non-wetting, which is required to form droplets. The functional groups used were typically $-\text{CH}_3$ or $-\text{CF}_3$ groups which tend to have the low surface energy desired [6; 7]. In the passivation coating research, SAM coatings were used to create a surface suitable for initiating the atomic layer deposition process. The chemicals used had high surface energy $-\text{OH}$ groups as the functional end groups, which allow the initial layers of water vapor to adsorb on the surface. The $-\text{OH}$ groups can also directly bond with the $\text{Al}(\text{CH}_3)_3$ groups to start the cyclic ALD process.

1.3 Applications

Thermodynamics dictates that some waste heat is generated when converting energy from one form to another. If not treated properly, waste heat can have detrimental impacts on the efficiency, reliability, and capability of many systems and devices. The applications are wide ranging. The dropwise condensation research presented in Part I of this thesis has applications in a number of industries where more efficient disposal and utilization of waste heat is parallel to increased efficiency. The collection of work performed in Part II is more focused on improving the reliability and capability of many systems where power density is of primary concern.

In the chemicals processing industry, cooling and heating of two-phase (vapor/liquid) mixtures is quite common. Distillation columns are a prime example where mixtures are separated through boiling and condensing processes. An important

consideration in the design of distillation columns is the size dependent upfront cost of the column. The promotion of dropwise condensation over filmwise condensation has potential to shrink the size and decrease the cost of the column. In the power industry, process steam used to rotate steam turbines is condensed before the liquid condensate is pumped up to pressure. The thermodynamic efficiency of the overall process can be improved if the condensate temperature is reduced. Dropwise condensation can be used in the condenser to improve the heat transfer rates resulting in higher efficiency steam powered turbine systems.

In various electronics cooling applications, waste heat disposal more strongly affects reliability and capability than efficiency. In central processing units (CPU's), all of the electrical energy used to process information is ultimately converted to waste heat in the high heat flux cores of the CPU. CPU reliability is strongly dependent on the operating temperature of the transistors. The operating temperature of the CPU's depends on many thermal elements, including the heat sink, heat spreader, thermal interface materials, and chip level packaging. The thermal methods used to cool CPUs is strongly dependent on the form, fit and function requirements of the application. In servers, large air cooled heat sinks suffice, as ample volume is available for heat sinking. The large heat sinks relative to the CPU heat source, create a need for heat spreaders to move heat from the CPU to the entire base of the heat sink. Using dropwise condensation in vapor chambers or heat pipes (see Chapter 5.1) is an appropriate strategy [8]. In mobile electronics devices, bulky heat sinks are too cumbersome, forcing advanced CPU packaging to be used in order to maintain the junction temperature within its operating range. Technologies such as the junction level cooling technology developed in Chapter

7 seem to be an appropriate fit for these mobile applications, such as cell phones and tablets.

Using dropwise condensation in heat pipes can also have meaningful impacts in a number of emerging applications. Light emitting diodes (LED) are an emerging lighting technology that is set to take over general purpose residential and commercial lighting in the next decade. LEDs require a high degree of thermal uniformity and cooling to maintain consistent light quality and maintain reliability [9]. In the medical industry, polymerase chain replicators (PCR) machines have an insatiable need for improved thermal management. PCR machines are used to replicate molecules, such as DNA, by rapidly cycling samples to precise temperatures that allow enzymes to facilitate the replication processes. The thermal uniformity of all samples is paramount to achieve uniform replication across all of the samples. Most importantly, the faster the samples can be cycled increases the throughput, and therefore the commercial value of the PCR machine.

Micro-channel cooling (Chapter 6) and jet impingement (Chapter 8) are appropriate for ultra high heat flux cooling. The system infrastructure required to implement these cooling solutions, including pump, tubing, radiators, controls, filters, etc, are often too costly and complex for applications other than military or specialized applications [10]. The technologies often find homes with high heat flux applications other than CPU cooling, including laser diodes and concentrated solar systems.

1.4 Synopsis

This dissertation contains research into several topics. All topics in this dissertation fit into the theme of advanced thermal management in micro- and nano-

length scales, where coatings are often used to manipulate heat transfer. The first part of this dissertation consists of the primary research effort into dropwise condensation heat transfer. The second part of the dissertation contains several thermal research efforts involving coatings for passivation in micro-channel coolers, micro-scale and molecular level modeling of die level phase change materials, and impingement cooling of high heat flux CPU's.

Dropwise condensation heat transfer was investigated from both experimental and theoretical perspectives. The initial efforts involved preparing and investigating dropwise condensation on gradient surfaces (Chapter 2) and on hydrophobic wick structures (Chapter 3). The more technology based experimental efforts lead to some investigations into the modeling of typical dropwise condensation surfaces (Chapter 4). Further, the collaboration between industry and academia lead to some investigation into some application issues very important to the commercialization success of the technology, including the use of the dropwise condensation in vapor chamber devices (Chapter 5). Chapter 5 also includes some life tests of the SAM coatings used throughout the research effort. Several conclusions and successful outcomes came of the dropwise condensation effort:

- By condensing on gradient surfaces, droplets can be propelled against gravity allowing the surfaces to exhibit high heat transfer capabilities.
- The SAM coatings are capable of extended life if the coatings are limited to temperature ranges suitable for electronics cooling.
- A dropwise condensation heat transfer model suitable for standard dropwise condensation surfaces and multiple fluids was developed. The new model is more

accurate, less numerically intensive, and captures more physics than the previous state of the art models.

In Part II, several research efforts are presented that build on the theme of interdisciplinary research involving surface coatings and multiple length scales in thermal management. In Chapter 6, the use of nano-scale ceramic coatings deposited in micro-channel coolers is explored for the purpose of preventing premature erosion and corrosion at high velocities. The research showed promising results that these coatings help improve reliability under stringent operating conditions. In Chapter 7, die level phase change materials are explored to help dampen thermal fluctuations at the junction of pulsed semi-conductor devices. A modeling effort, consisting of molecular dynamics simulations and finite element analysis to predict thermal performance under representative conditions, concluded that a 26% improvement could be obtained using this approach. In Chapter 8, jet impingement is investigated to cool CPUs operating without a heat sink for use in a silicon debug process. A highlight of the research effort includes the development of a thermal model to estimate the local heat transfer coefficient with jet impingement. The model was verified using a state of the art Intel supplied thermal test vehicle.

PART I

DROPWISE CONDENSATION

Chapter 2

Condensation on Gradient Surfaces Experiments

2.1 Background and Introduction

Dropwise condensation alone has shown the ability to increase condensation heat transfer coefficients by an order of magnitude over filmwise condensation that is typical of vertically oriented condensers in thermosyphons and other two-phase systems. By condensing on a wettability gradient surface, heat transfer coefficients are further increased over dropwise condensation by the fast removal of condensing droplets on the surface. Unlike the filmwise and traditional dropwise condensation, the gradient surface does not require gravity or forced convection to remove liquid from the condensing surface. Previous work has demonstrated gradient surfaces that effectively removed condensing liquid at horizontal orientations on silicon surfaces [5]. In this thesis, additional data were acquired on surfaces where the gradient was prepared directly on a copper surface using thiol based surface chemistry [11]. Data were also acquired at different inclinations, including against gravity.

A gradient surface is defined as a surface with locally varying surface energy or wettability [12]. The gradient surface causes a droplet to experience decreasing contact angles as the droplet travels along the path of increasing surface energy, as shown in Figure 2.1. The difference in contact angle is due to locally varying properties of the condensing surface, controlled by varying surface concentrations of molecules with low surface energy. The difference in contact angle on opposite sides of a droplet condensing on a gradient surface provides a driving force in the direction of decreasing contact angle.

The motion is sustained until the droplet reaches the end of the gradient (e.g. near an evaporator).

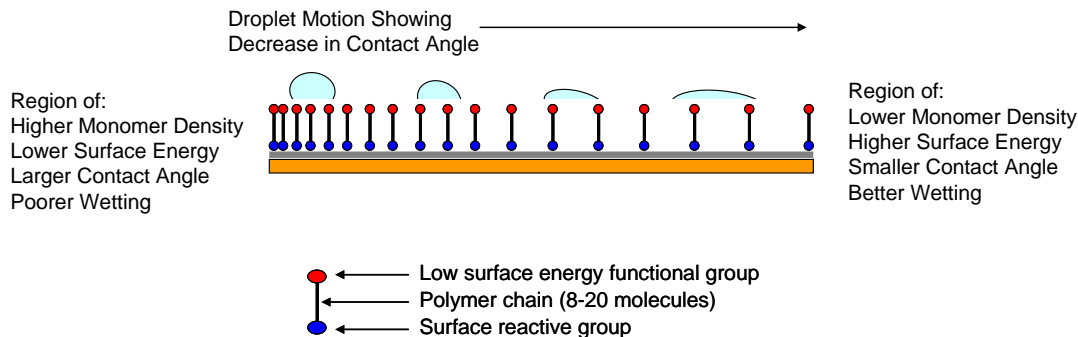


Figure 2.1 The physics of droplet motion on a chemically induced surface gradient is illustrated. A constant supply of liquid droplets is supplied uniformly by condensation on the gradient surface. The droplets move towards the more hydrophilic region of the gradient surface due to the difference in contact angle experienced by opposing sides of the droplets.

The surface gradient is created by varying the concentration of a monomer with hydrophobic surface properties along the surface. In one method of fabricating surface gradients, the concentration on the surface is controlled by a diffusion controlled reaction of an organosilane molecule on the surface. An illustration of the surface modification process is shown in Figure 2.2. A liquid droplet of the organosilane molecule is suspended above the silanized copper surface. The molecules evaporate from the droplet and diffuse through air, approaching the copper/silicon surface. Once the organosilane molecules reach the surface, the reactive end of the molecule forms a chemical bond with the silicon surface. The low surface energy end of the molecule points directly away from the surface. Since there is a gradient in the bulk concentration (air/SAM mixture) above the surface, a gradient in the surface concentration of the molecules is developed.

This gradient in bulk concentration is due to the diffusion of the SAM molecules from the concentrated liquid SAM droplet through the dilute air phase.

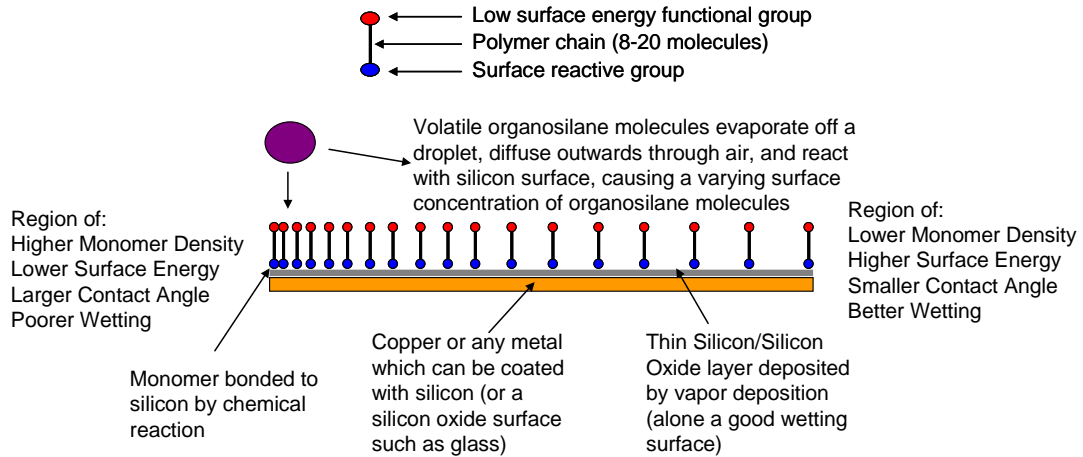


Figure 2.2 The fabrication of a chemically induced surface gradient is illustrated. Organosilanes are short polymer molecules of which one end reacts with a silicon surface and the other end can possess a desirable surface characteristic, in this case a low surface energy molecule is desired. These molecules are bonded in a diffusion controlled reaction to create a variation in concentration and therefore surface energy on a surface. Liquid droplets formed by condensation on the surface gradient will move towards the better wetting region.

2.2 Fabrication of Test Articles and Surface Preparation

Several test articles were fabricated in order to establish a baseline for the thermal test data. The first test article was prepared to exhibit a hydrophilic (wetting) filmwise condensation surface that served as the baseline to characterize the condensation measurement test apparatus. Filmwise condensation was used as the baseline since it is very well characterized. In fact, an analytical solution for the heat transfer coefficient associated with filmwise condensation exists which proved to be useful when challenging the initial experimental results [13]. A polished copper surface is not necessarily

hydrophilic after cleaning, as copper experiences a multitude of oxidation states which all have different surface energies. Some of the oxidation states even cause the condensation mode to be “transitional,” a wavy flow that is not entirely dropwise or filmwise. To compare the filmwise test data to existing filmwise models, the surface needed to be entirely filmwise. A carefully prepared oxide was grown on the copper surface by dipping a clean copper surface in dilute hydrogen peroxide (~3%) until the surface appeared amber. Before insertion into the test station the surface hydrophilicity was visually verified by placing a droplet of water on the surface to observe the wettability.

The second condensing surface prepared was the traditional non-wetting surface (without a wettability gradient). In this context, the non-wetting surface refers to a surface that is completely covered with a hydrophobic self-assembled monolayer, giving the surface the maximum hydrophobicity that can be attained with self-assembled monolayers on polished surfaces. The copper surface was first polished smooth then cleaned in acetone. The test article was then dipped in nitric acid to remove any oxides formed on the copper surface due to temporary exposure to air. Under argon, the sample was then rinsed, blown dry, and placed in dilute hydrogen peroxide to form a consistent chemical oxide on the surface. The sample was then rinse and blown dry before being placed in a solution containing the self-assembled monolayer forming chemical. Self-assembled monolayers can be formed directly on copper surfaces using a group of chemicals known collectively as thiols or mercaptans. The enabling feature of thiols is a sulfur functional group on one tail of the molecule that is known to bond with coinage metals, such as gold, silver and copper. The most common way to form a self-assembled monolayer on copper is by making a dilute solution of the thiol in an alcohol such as

ethanol or isopropyl alcohol (IPA). IPA was chosen for this study due to its availability in our lab, as it doesn't seem that the choice of alcohol has a strong effect on the self-assembled monolayer formation. 1-Octadecyl mercaptan was chosen as the thiol, as it has the largest carbon chain available from commercial suppliers. Longer chain length molecules tend to assemble more orderly on the surface than smaller chain length molecules and are preferred for making the surfaces desired for this application. After immersion of the test article for an hour in the solution, the surface was rinsed with methanol and blown dry.

A photograph of the water droplet placed on the hydrophobic surface is shown in Figure 2.3. The contact angle is around 110° , which is consistent with other observations found in the literature for self-assembled monolayer surfaces. Droplets placed on the surface also moved easily upon application of a force (e.g. gravity or drag). This served as an indication that the difference between advancing and receding contact angles (also known as contact angle hysteresis) was small, since a small force was required to move the droplets. If there was a larger difference in the contact angles, the droplets would remain "pinned" to the surface and not move readily. The low hysteresis surface is a strong indication that the surface was prepared well, indicating that the surface molecules are well organized on the surface.

The preparation of the gradient surfaces proved to be the most difficult. Provided here is the best/final strategy that was developed to prepare the gradient surfaces on copper. The copper surface was polished, cleaned, dipped in nitric and hydrogen peroxide, following the same procedures as the non-wetting surface until the rinse following the hydrogen peroxide. The surface was then immersed in a solution of

IPA/11-mercapto-1-undecanol. The 11-mercapto-1-undecanol has the same thiol end group as the 1-octadecyl mercaptan, but has a hydroxyl end group on the other end, just like a typical organic alcohol. The result is that surfaces prepared with 11-mercapto-1-undecanol are more hydrophilic. A hydrophilic base is required with the gradient surface since gradually change in the wetting properties along the surface from wetting to non-wetting is desired. The test article was placed in a dilute IPA/11-mercapto-1-undecanol solution for an hour then rinsed with methanol.

The hydroxyl group also can bond with other types of self-assembly molecules known collectively as silanes. Silanes have a chlorosilane group on one end which is capable of bonding to oxygenated surfaces. Successful gradients in the past have been prepared using silanes on silicon surfaces that have been oxidized and on glass slides (which are silicon dioxide). The presence of the hydroxyl molecules on the surface (due to the 11-mercapto-1-undecanol) are sufficient to act as a bonding site for the silanes, and traditional gradient making techniques using silanes can then be applied. The 11-mercapto-1-undecanol coated copper surface was first heated in an oven at 150°C to drive off any moisture the surface, as silanes will become hydrolyzed before they contact the surface if moisture is present, preventing a secure bond to the surface. The standard diffusion controlled reaction technique using octadecyltrichlorosilane was performed to prepare a gradient on the surface.

The physics behind the procedure used was previously described in the Chapter 1 review. A diagram showing the preparation of the surface gradient was shown in Figure 2.2 but will be described in more detail here. The hydrogenated end points away from the surface, and causes a decrease in surface energy of the surface. The chain length of the

polymer is comparable to other hydrocarbons such as octane, and therefore has a significant vapor pressure on the order of similar sized hydrocarbon molecules. The vapor pressure makes the evaporation of the octadecyltrichlorosilane off a droplet into air near the surface of the substrate feasible. Surface areas near the droplet become maximally concentrated with a single monolayer of the organosilane molecule. As the molecules diffuse away from the concentrated droplet a concentration gradient is created in the air above the surface.



Figure 2.3 Photograph of water droplet on a polished copper surface that has been prepared with 1-octadecyl mercaptan, causing the surface to be hydrophobic.

Consequently, a gradient in the concentration of the molecules on the surface is also created as the molecules chemically react with the 11-mercapto1-undecanol coated surface. The applied layer is still a monolayer thick, the molecules are just farther apart in less populated areas. The process worked well. Surfaces were fabricated with gradients approaching 1 inch in length, where a single droplet placed on the hydrophobic side of

the gradient (in an open air atmosphere) would move to the hydrophilic side in a few seconds.

The next step in the fabrication procedure involved mounting the test articles in a vacuum sealed test section for thermal performance testing. A photograph of the fabricated test section is shown in Figure 2.4. The test section consists of a boiling section (not shown) and condensing section. The boiling section is a stainless steel container with an embedded cartridge heater to supply heat. The boiling section is connected to the condensing section by stainless steel tubing through the two ports. Depending on the orientation of the testing (vertical or horizontal) the ports can serve as either the liquid return or vapor entrance lines. Cooling in the condenser is done by a liquid cooled cold plate that is attached to a thermostatically controlled chiller. The condensing test section is sealed by O-rings on both sides of a stainless insert piece. The top seal is made to a see through polycarbonate piece of plastic for visualization. The unit is bolted together to hold all the pieces in place and keep a vacuum tight seal.

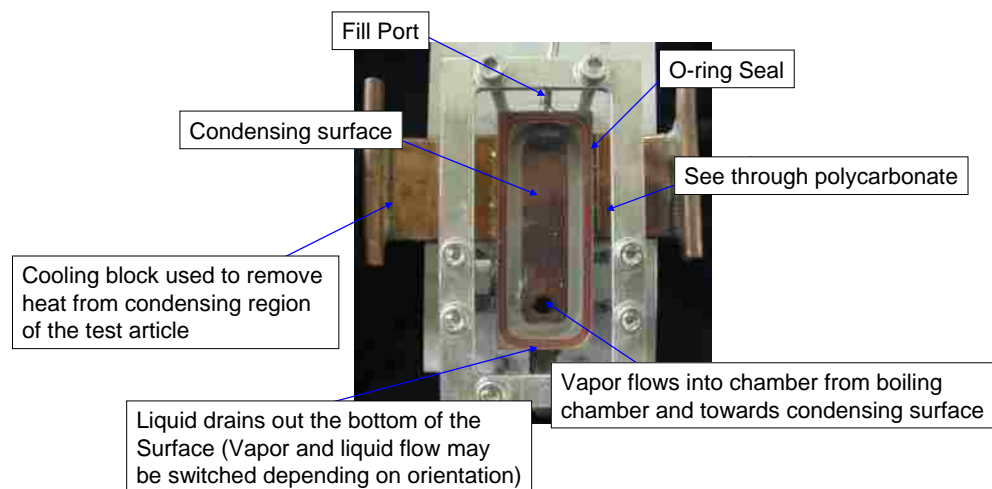


Figure 2.4 A Photograph of the assembled test section is shown.

2.3 Thermal Performance Testing

The heat flux and heat transfer coefficients along the condenser were measured using a series of thermocouples as shown in the side view photograph of the test article in Figure 2.5. The sets of thermocouples allow for calculation of the heat flux by conduction calorimetry. Conduction calorimetry involves using the distance between the thermocouples, thermal conductivity of the copper material and difference in temperature between the thermocouples to calculate the heat flux through the plate. By knowing the distance between the thermocouple and the surface, as well as the calculated heat flux and thermal conductivity of the copper material, the temperature of the wall at the surface was extrapolated. The temperature of the saturated vapor was measured with a thermocouple located in the vapor space of the test section. Knowing the wall temperatures, heat fluxes, and vapor temperature allowed for accurate calculation/measurement of the local wall heat transfer coefficient. It should be noted that a gap was machined in the copper plate between the connection port and condenser regions to prevent a thermal link between the two regions which would complicate heat transfer coefficient measurements due to conduction effects. The data reported here is a numerical average of the heat transfer coefficients measured in the three locations.

All condensation data were obtained using water as the working fluid. All tests were taken at a saturation temperature of 100°C without non-condensable gas (i.e. not in open atmosphere). Data were acquired at four input powers (25W, 50W, 75W and 100W) over the 2.54cm by 1.27cm heat input section (condenser heat fluxes ranged between 7.75 W/cm² and 31 W/cm²). Data were acquired for three surfaces (filmwise,

dropwise, and gradients) at four orientations. A plot of the four orientations tested is shown in Figure 2.6.



Figure 2.5 Shows a side view of the test section. Thermocouples inserted in the 9 holes are used to measure the heat flux and surface temperature of the condensing surface. A gap was also machined to prevent heat from leaking in through the vapor/liquid ports.

The vertical orientation (Figure 2.6A) was tested first. A plot of the experimental results is shown in Figure 2.7. The most important piece of information in Figure 2.7 is the agreement of the wetting data with the Nusselt filmwise condensation model. The near perfect agreement validates the test section and method of heat transfer coefficient measurement for this study. The model verification also adds credibility to the often difficult to accurately acquire dropwise condensation data (discussed later). Dropwise condensation on the non-wetting surface produced heat transfer coefficients that were 5-8 times higher than filmwise condensation, a significant improvement. By condensing on the gradient surface, a 35% further improvement in the heat transfer coefficient was observed as compared to the dropwise condensation surface. The expected improvement in the vertical orientation was not expected to be excessive, since gravitational force is able to pull condensing droplets on a vertical surface. The gradient adds some additional force to move the droplet in addition to gravity, resulting in increased performance.

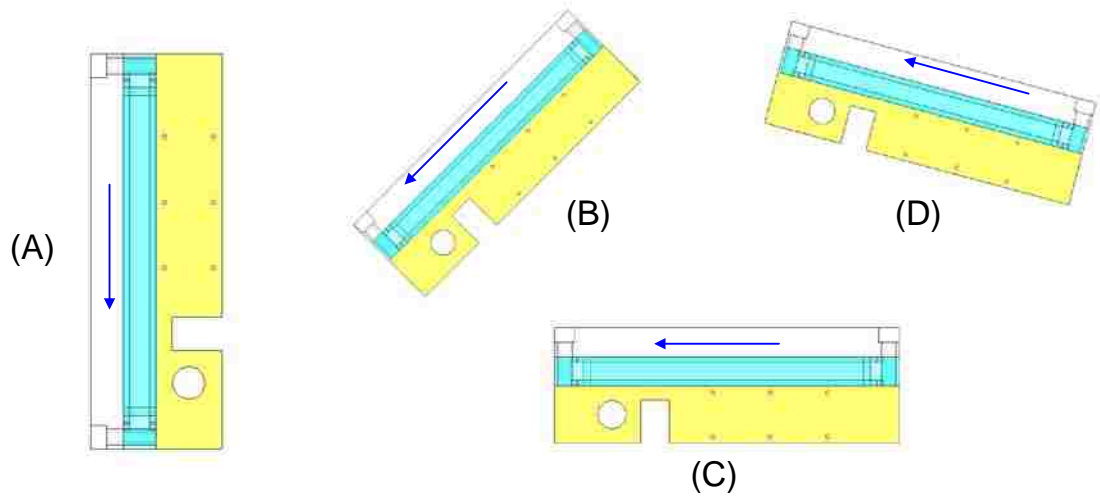


Figure 2.6 This figure shows the various orientations to be tested including the vertical (A), 45° angle (B), horizontal (C), against gravity (D).

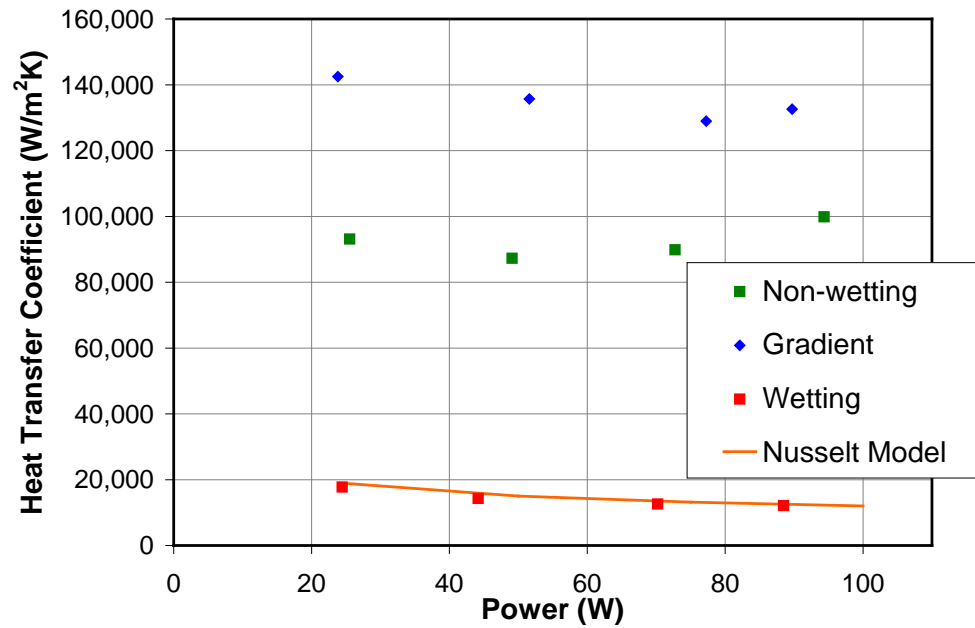


Figure 2.7 A plot of experimental measured heat transfer coefficient results for a non-wetting, gradient, and wetting surface in the vertical orientation (Figure 2.6A) are shown. The filmwise data compared well to the Nusselt model, validating the acquired data from the test section.

In the next test, the test section was tilted at a 45° angle (as shown in Figure 2.6B) and tested. The experimental data for the 45° orientation is shown in Figure 2.8. Again the filmwise heat transfer coefficient data matched well with the Nusselt model when modified for the partial loss of gravity. All modes of condensation showed reduced performance as compared to the vertical testing. The performance of the non-wetting surface fell about 65%. The gradient surface fell about 50%. However, the performance of the gradient surface was 200% better than the non-wetting surface at 45° as compared 35% in the vertical orientation. It seems that as gravity is reduced, the gradient surface is still able to maintain high droplet velocities required to keep the heat transfer coefficient higher than filmwise condensation. Since the non-wetting surface relies solely on gravity for droplet motion, the reduction in performance is more rapid as gravity is removed.

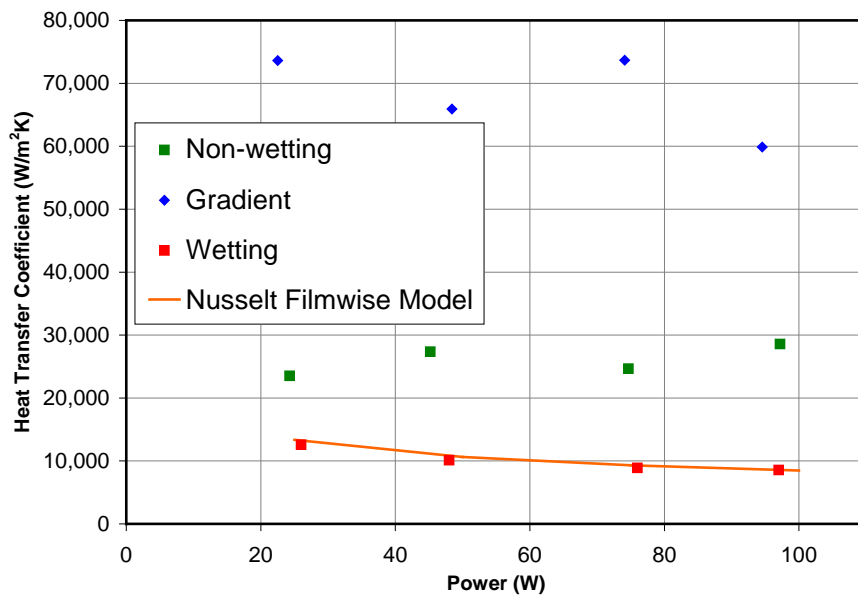


Figure 2.8 A plot of experimental measured heat transfer coefficient results for a non-wetting, gradient, and wetting surface in the 45° orientation (Figure 2.6B) are shown. Performance degraded much more rapidly with the non-wetting surface as compared to the gradient.

The next test was performed in the horizontal orientation (Figure 2.6C). Data were only acquired with the gradient surface, although gathering data with both the wetting (baseline) and non-wetting (without gradient) test articles was attempted. Without gravity to remove the condensing fluid, liquid just flooded the condensing region of both the wetting and non-wetting test articles. The heat transfer coefficients measured were $\ll 500\text{W/m}^2\text{-K}$ at very low heat fluxes (less than 5 watts of power) since not enough thermal driving force was present to move more heat through the poorly performing flooded heat transfer surfaces. The gradient surface was still able to move liquid droplets without the aid of gravity. The result was a heat transfer coefficient in excess of $35,000\text{W/m}^2\text{-K}$. As a reference, this is approximately 3 times greater than the heat transfer coefficients measured on a wetting surface with the full aid of gravity.

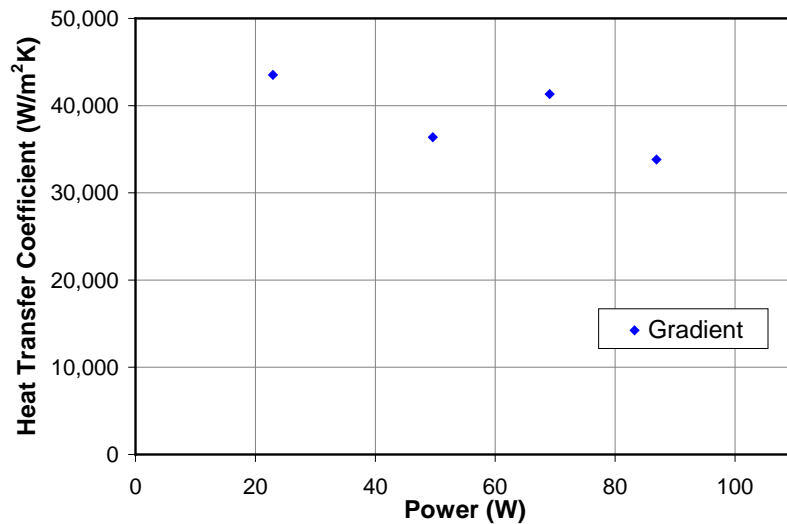


Figure 2.9 A plot of experimental measured heat transfer coefficient results for a gradient in the horizontal orientation (Figure 2.6C) are shown. The non-wetting and wetting surfaces flooded as liquid was not able to return to the boiling section.

The final test was performed with the condenser operating against gravity (Figure 2.6D). In this orientation the droplet has to be moved uphill in order to reach the end of the condensing section. A wick was inserted at the end of the condensing section to move liquid against gravity from the end of the gradient to the liquid return port. This could be avoided if the gradient ended at the liquid return port. However, the adiabatic gap section machined in the test article prevented the gradient from being close enough to the liquid return port.

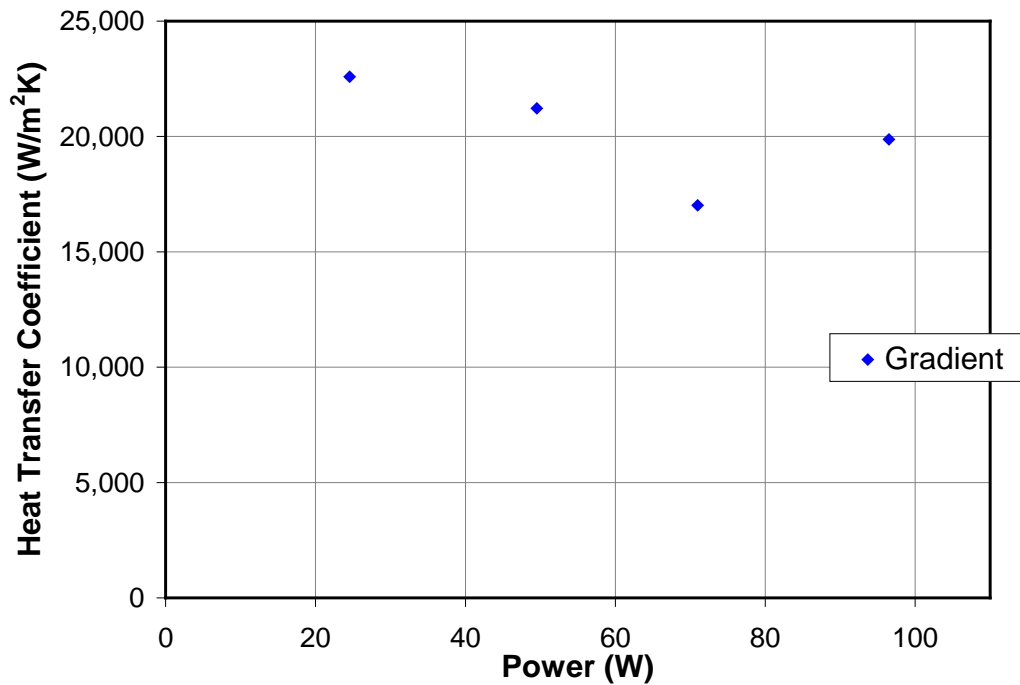


Figure 2.10 A plot of experimental measured heat transfer coefficient results for a gradient tilted 5° against gravity (Figure 2.6D) are shown. The non-wetting and wetting surfaces flooded as liquid was not able to return to the boiling section.

Inserting a piece of copper screen mesh worked well in transporting fluid from the gradient over the gap to the liquid return port. The measured heat transfer coefficients were very high. However, there was some degradation in performance as compared to the horizontal testing. In order for the droplet to move uphill, they needed to grow until they spanned larger portions of the gradient to get additional driving force. The larger droplets required to move uphill resulted in more of the surface being coated with fluid, lessening heat transfer coefficients.

An overall summary of the performance testing is provided here:

- In the vertical orientation the wetting/filmwise test data matched well with prediction, validating the test apparatus and procedure.
- The gradient surface performed 35% better than the non-wetting surface under vertical orientations.
- As gravity was reduced to a 45° angle, the gradient was better able to maintain its higher performance as compared to the non-wetting surface.
- Horizontally and against gravity, the gradient performed much better than the non-wetting surface as the non-wetting and wetting surfaces flood without gravity to remove condensing liquid.

2.4 Conclusions and Future Work

Data were acquired for condensation directly on copper surfaces exhibiting wettability gradients. Prototype gradient surfaces on copper were fabricated using novel methods to achieve the surface properties required to rapidly move condensing droplets. Further, data were acquired at multiple inclinations, including against gravity. At gravity aided orientations, the gradient surface showed a 35% improvement in the measured heat

transfer coefficient over traditional dropwise condensation surfaces (non-gradient). At the horizontal orientation, where gravity is not able to remove condensing liquid droplets on traditional condensation surfaces, the gradient surface performed orders of magnitude better in terms of heat transfer performance. The gradient surface was also able to move liquid droplets uphill against gravity while maintaining the similar high heat transfer coefficient performance. A summary of the work is provided below.

- A fabrication procedure was developed and demonstrated to manufacture wettability gradients directly on a copper surface.
- A test apparatus was built and qualified to make accurate condensation heat transfer measurements.
- Gradient surfaces performed significantly better than the traditional non-wetting (without gradients) surfaces for all orientations.
- Gradient surfaces demonstrated the ability of moving liquid droplets away from the surface on horizontal surfaces and against gravity, something other condensation modes aren't capable of doing.

In the future, more work needs to be performed to understand the effect of the gradient length on performance, including the heat transfer coefficient and ability to move droplets against gravity. Coating longevity will also always be an issue in condensation applications. New and innovative coatings that can be used to create low hysteresis surface energy gradients should be of high interest.

Chapter 3

Hydrophobic Wick Structures Experiments

3.1 Background and Introduction

In order for the military to use high power electronics in future military vehicles and aircraft, some thermal management challenges must be solved [10]. The challenges include not only managing the high heat fluxes and total power dissipated by these devices, but also succeeding within limited volume and limited energy budget constraints. Evaporative cooling technologies provide the best way to manage heat under these constraints as compared to single phase technologies for a number of reasons. Two-phase systems have naturally higher boiling and condensation heat transfer coefficients due to favorable conditions created by phase changing at the wall. Lower flow rates are required because of the higher effective heat capacity of two-phase solutions in the latent heat of vaporization as compared to sensible heating.

To manage the high heat fluxes, two-phase cooling has manifested itself in a number of technologies where the evaporator has been the main focus of attention. These technologies include but are not limited to micro-channel evaporators, heat pipes, loop heat pipes and hybrid two-phase loops. In all of these devices, condensation is required to sink the heat to an outside cooling source. In many cases the condenser can be designed with sufficient area so that the lower heat transfer coefficient associated with condensation as compared to evaporation is not an issue. For example, in air-cooled heat sinks the air side heat transfer coefficient is orders of magnitude lower than the condensation heat transfer coefficient, making the airside improvement a far more urgent priority. However, in cases where the volume requirement for the condenser is limited

and the heat transfer coefficient on the sink side is low (likely by some method of single phase liquid forced convective cooling) there is a need for condensation heat transfer coefficients larger than what is currently available.

Dropwise condensation promoted by non-wetting self-assembled monolayers (SAM) on porous metal wicks was investigated with the purpose of solving compact condenser issues in these types of military and commercial applications. Dropwise condensation on a bare surface has shown the ability to increase condensation heat transfer coefficients by an order of magnitude over film condensation [1]. By condensing on a wick, the heat transfer coefficient can be further increased over on a bare wall surface because of the increased surface area of the porous metal wick and potential lower contact angle hysteresis. The pressure drop of a dropwise condensation heat exchanger is also inherently lower since dropwise condensation results in higher condensation heat transfer coefficients without relying on increased fluid velocity as compared to other enhancement means such as forced convection through micro-channels and grooved tubing, etc. To promote dropwise condensation on a wick, the wick is coated with a self-assembled monolayer with low surface energy, to make the surface non-wetting. The demonstrated dropwise condensation technology is applicable in actively pumped two-phase flow devices such as hybrid two-phase loops, passive two-phase flow devices such as loop heat pipes, and gravity aided heat pipes or thermosyphons [14; 15].

The primary experimental objective of this effort was to observe the heat transfer coefficient with dropwise condensation on wick structures in passive and pumped flow

loops, since this hasn't been performed before. The second experimental objective is to determine the effect of pore size on the observed behavior.

3.2 Nomenclature

P Pressure

r Radius

σ Surface tension

3.3 Mechanism for Condensing on Wick Structures

Droplets forming on a polished non-wetting surface grow and coalesce until the droplets become large enough that gravity or shear forces can remove the droplets from the surface. When the droplets are removed from the surface, saturated vapor again comes in close contact with the surface, repeating the condensation process. In this process droplets are generally on the order of a few millimeters in diameter. Figure 3.1 demonstrates the mechanism by which a non-wetting sintered metal wick will enhance traditional dropwise condensation. Initially (1) droplets form in the wick between the porous powder layers formed by either copper screen wraps or sintered copper powders. The droplets themselves experience a contact angle above 90° as the surface is non-wetting. The droplets stay within the wick as they coalesce (2) and grow (3) until a droplet forms that is of equal diameter to that of the wick pore. At this point the Laplace pressure inside the droplet is determined by the pore radius of the wick as described by Eq. 3.1 [9]. Further growth in the droplet (4) results in a droplet that “sticks out of the top of the wick” with two effective pore radii. One radius is for the portion of the droplet in the wick equal to the pore radius of the wick. The other radius is for the portion of the droplet sticking out of the wick. This outer radius is greater than that of the wick equal to

the vapor core as described by Eq. 3.2. This radius of the vapor core approaches infinity as compared to the wick pore radius, resulting in zero Laplace pressure as described by Eq. 3.3. Therefore, the pressure of the droplet in the wick will always be greater than the pressure of the droplet in the vapor core (Eq. 3.4). The pressure balance will lead the droplet to be propelled out of the wick to the vapor core (5) by the capillary action of the non-wetting (hydrophobic) wick. At this point the condensate will form large droplets on the surface similar to that of bare wall condensation. The larger droplets can be removed from the surface by gravitational forces, as in a heat pipe, or by the shear forces of flowing vapor as in a pumped two-phase loop or loop heat pipe.

Dropwise condensation on the hydrophobic wick following the described mechanism is expected to have lower thermal resistance than polished wall dropwise condensation for a number of reasons. The heat transfer coefficient in dropwise condensation largely depends on how small the droplets on the surface can be kept. Smaller droplets cover less of the surface with liquid, diminishing the blanketing effect of the liquid on the surface. In polished surface dropwise condensation, the droplet size is determined by preset conditions such as gravity, inclination, and flow rate. By condensing on the wick, the droplet size at the wall is controlled by the pore size of the wick. While droplets on the wall in bare wall dropwise condensation are on the order of a few millimeters, the pore size of a wick can be as small as a few microns. Another advantage of using a wick is increased surface area. By having more surface area available for condensation, the overall thermal resistance of the condensing surface (effective heat transfer coefficient) is expected to be lower than on a bare wall surface.

The transport of droplets away from the surface by the wick is also expected to have beneficial effects when the full aid of gravity is not available. On a polished surface droplet sizes increase as the condensing surface approaches a horizontal orientation, as larger droplet sizes are needed to overcome the forces which hold the droplet to the wall. In comparison, the droplet size of the wicked surface near the wall is still determined by the small pore size of the wick. Even though the droplets on the surface of the wick may be of similar size to that of the bare wall surface, the droplets nearest to the wall determines the thermal resistance of the wall and are of utmost importance.

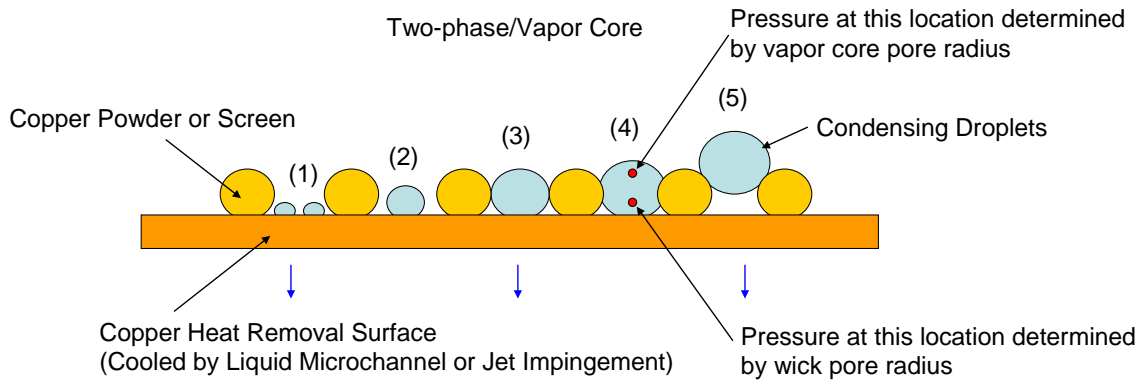


Figure 3.1 Illustration of dropwise condensation promotion using non-wetting metal wick. Droplets remain in the wick as they grow (1) and coalesce (2). (3) Eventually the droplet grows match the radius of the wick. (4) Further growth forces the bubble into a non-spherical shape with two effective radii. (5) The Laplace pressure gradient causes by the two differing radii pushes the droplet out of the wick into the vapor core.

$$\text{Eq. 3.1} \quad P_{droplet,wick} = \frac{2\sigma}{r_{wick}}$$

$$\text{Eq. 3.2} \quad P_{droplet,vaporcore} = \frac{2\sigma}{r_{vaporcore}}$$

$$\text{Eq. 3.3} \quad r_{vaporcore} \rightarrow \infty, P_{droplet,vaporcore} \rightarrow 0$$

$$\text{Eq. 3.4} \quad P_{droplet,wick} > P_{droplet,vaporcore}$$

Another advantage of using dropwise condensation is low pressure drops. In systems such as micro-channels, high heat transfer coefficients are the result of small hydraulic diameters. The small hydraulic diameters also have inherently higher pressure drops as compared to flow through a flat plate heat exchanger gap. Since the heat transfer coefficient in dropwise condensation is not reliant on small hydraulic diameters, the surface could be prepared in gaps similar in size to flat plate heat exchangers while inheriting the flat plate heat exchanger's characteristically low pressure drops.

3.4 Wick and Surface Preparation

Although not generally practiced on metal wicks, altering the surface properties of a copper wick to be non-wetting using the SAM technique was demonstrated to be straight forward and integrate well with existing heat pipe sintering procedures. A schematic showing the expected final result of a SAM coated wick is shown in Figure 3.2. The copper surface needs to be kept very clean (uncontaminated and unoxidized) after the sintering process has been performed so that the chemical bond to the surface is strong. The self-assembly process occurs spontaneously on the surface when a solution of the molecules in either a liquid or vapor form comes into contact with the surface. This method of preparation is preferred because the task of removing excess chemical from the wick is avoided.

For a solution to repel a surface (non-wetting) the fluid's surface tension must be larger than the surface tension of the surface as described by Young's equation, shown in Eq. 3.5 for reference. The contact angle must be greater than 90° for the surface to be considered non-wetting. Fluids with higher surface tension will experience higher

contact angles (more non-wetting) than solutions with lower surface tension. This limits the use of this technology to primarily water or other high surface tension organic fluids.

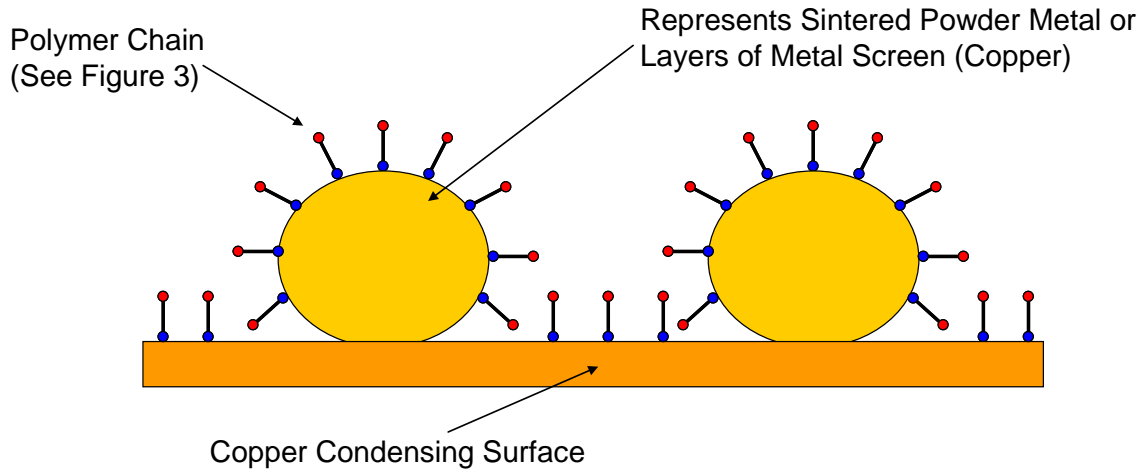


Figure 3.2 Illustration of self-assembled monolayer surface preparation technique on a porous wick structure. The molecules with envelope the wick and wall, creating a non-wetting surface on all locations of the wick and wall.

$$\text{Eq. 3.5} \quad \sigma_{SG} = \sigma_{SL} + \sigma_{LG} \cos \theta$$

Two polished copper test articles appropriate for filmwise and dropwise condensation were fabricated. The filmwise surface was prepared by creating a chemical oxide on the surface with hydrogen peroxide. The dropwise condensation surface was prepared by creating a self-assembled monolayer of octadecyl mercaptan on the polished surface.

Two sintered wick test articles one with a layer of fine copper powder and the other with a layer of coarse copper powder were fabricated and coated with the same monolayer to promote dropwise condensation. The test articles with a layer of sintered copper powder are shown in Figure 3.3. A thin layer of powder was sintered to the center

of each test article where condensation will take place. The outer edge of each sample was left bare to help facilitate a leak tight seal to the test article. A hole is also placed in the center of each test article to allow for saturated vapor to enter the test section. Two screen wick test articles, one with single layer copper mesh and the other with double layers copper mesh, were fabricated and coated with the same monolayer to promote dropwise condensation.

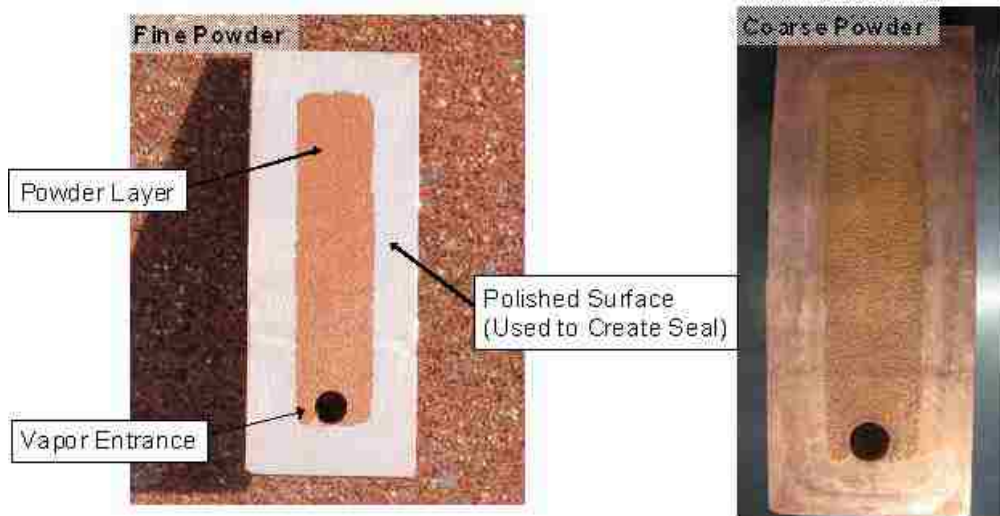


Figure 3.3 Photographs of a layer powder sintered onto test blocks.

The preparation of the non-wetting surfaces with the self-assembled monolayer was successful. The resulting contact angle with water is very high, approaching 150° . Photographs of a water droplet on the freshly prepared surfaces of the test articles are shown in Figure 3.4. The fluorinert droplet and methanol droplet photographs on the polished copper surface with the non-wetting treatments are shown in Figure 3.5 and Figure 3.6. The resulting contact angles of these two fluids' droplets are not as large as that of the water droplet. For the fluorinert, the contact angle was not high enough as to exhibit dropwise condensation. However, methanol proved to have a high enough

contact angle as to promote dropwise condensation at low heat fluxes on polished surfaces. However, methanol exhibited only filmwise condensation on wicked surfaces.



Figure 3.4 Photograph of water droplet on one layer of powder after treatment of the surface with a self-assembled monolayer of hydrophobic octadecyl mercaptan.



Figure 3.5 A droplet of a fluorinert (3m Novec Fluid HFE-72DE) is placed on a polished copper surface that has been prepared with a fluorinate self assembled monolayer. The contact angle is less than 10° .



Figure 3.6 A droplet of methanol is placed on a polished copper surface that has been prepared with a fluorinate self-assembled monolayer. The contact angle is roughly 40° .

3.5 Test Apparatus

The same condenser block described in Chapter 2.2 was used to perform testing. The heat flux and heat transfer coefficients along the condenser were measured using a series of thermocouples as shown previously in Figure 2.5. The sets of thermocouples allow for calculation of the heat flux by conduction calorimetry. Conduction calorimetry involves using the distance between the thermocouples, thermal conductivity of the copper material and difference in temperature between the thermocouples to calculate the heat flux through the plate. By knowing the distance between the thermocouple and the surface, as well as the calculated heat flux and thermal conductivity of the copper material, the temperature of the wall at the surface can be extrapolated. Knowing the wall temperature also allows for accurate calculation/measurement of the local wall heat transfer coefficient. The back side of the condenser region was cooled using a cold plate pressed to the bottom of the surface. The cold plate was connected to a thermostatically controlled chiller, and controlled to the desired saturated vapor temperature of the test article. A gap was machined in the copper plate between the evaporator and condenser regions to prevent a thermal link between the two regions which would complicate heat transfer coefficient measurements.

The copper sample plate was oversized to allow for the O-ring seal between the copper sample plate and see-through plate around the outside of the heated/cooled surfaces. These seals are important as a vacuum tight seal is desired for testing. A vacuum/fill port through the O-ring seal plate (not shown) is also required. The test article was partially filled to maintain saturated conditions in the system (liquid and vapor). To charge the unit with a prescribed amount of fluid, a vacuum was pulled on the

leak tight assembly and then back-filled with water. This method assured only saturated liquid and vapor, without any non-condensables, were present in the system. A valve was connected to the fill port to vent and fill the system. The O-ring plate also has a through hole for a thermocouple to measure the saturation temperature of the system. The O-ring seal plate height was designed large enough so that the pressure drop and velocity of vapor traveling from the evaporator towards the condenser are low enough to prevent shearing of the condensing liquid droplets.

The see through plate is an important part of the design as visual observations were key in this first attempt at understanding the physics of dropwise condensation on a wick. The plate was made of polycarbonate. Both surfaces of the plastic were untouched by machines (as supplied by the manufacturer) to allow for maximum optical clarity, other than the through holes for bolting the assembly together.

Along with the test articles, two types of test sections were fabricated. One test section is a passive flow loop system and the other is a pumped loop system. A solid model of the passive flow test section is shown in Figure 3.7. Fluid boils in the reservoir located at the bottom of the test section. Vapor travels up towards the test section and through the hole located in the center of the copper test article. The vapor condenses on the upper portion of the copper test article. The copper test article is cooled by a liquid cold plate attached to the back of the test article. Heat flux and surface temperature measurements were made by 9 thermocouples located between the liquid cooled cold plate and the condensing surface. Condensing liquid returns to the boiling chamber by flowing down a hole located in the sealing vessel. A fill port is located in the top of the test section to add fluid and remove non-condensable gas.

A solid model of the pumped loop test section is shown in Figure 3.8. Fluid boils in the boiling chamber located at the bottom of the test section. Vapor travels up towards the test section and through the hole located on top of the condenser chamber with the copper test article inside. The vapor condenses on the upper portion of the copper test article. The copper test article is cooled by a liquid cold plate attached to the back of the test article. Heat flux and surface temperature measurements were made by 9 thermocouples located between the liquid cooled cold plate and the condensing surface. Condensing liquid flows to the reservoir below the condensing chamber and is pumped upwards by the pump located below the reservoir to the boiling chamber. A fill port was located in the top of the test section to add fluid and remove non-condensable gas. A drain was located at the lowest position in the test section to remove liquid for the system. A flow meter was installed after the pump and before the boiling chamber. The system was properly insulated to minimize heat losses to the ambient during performance testing. The voltage and current of the cartridge heater were measured using a Fluke meter. Temperatures and flow rate through the cold plate were measured and used to calculate energy dissipated through the block. Heat flux through the plate was measured using conduction calorimetry through the plate. These three measurement methods were used to quantify the energy balance of the system.

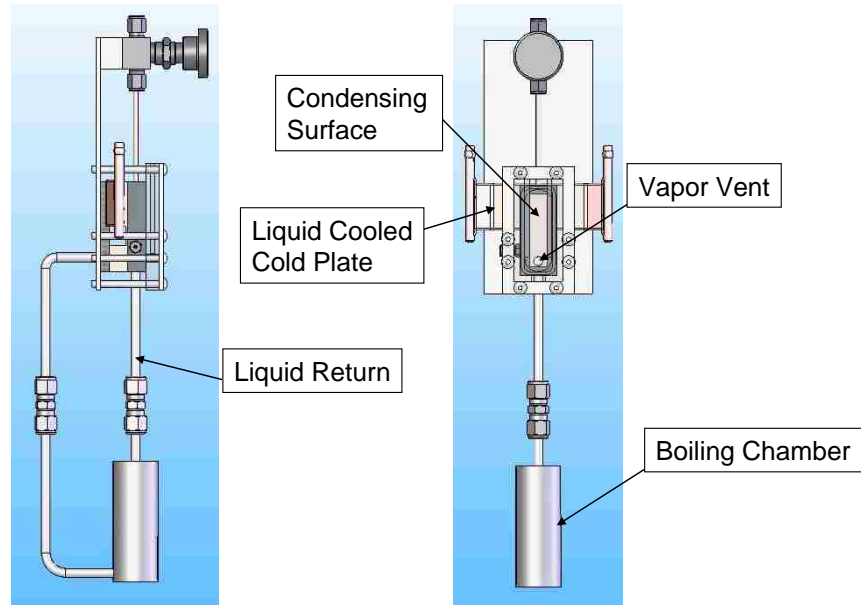


Figure 3.7 A solids model picture of the passive flow loop test section is shown.

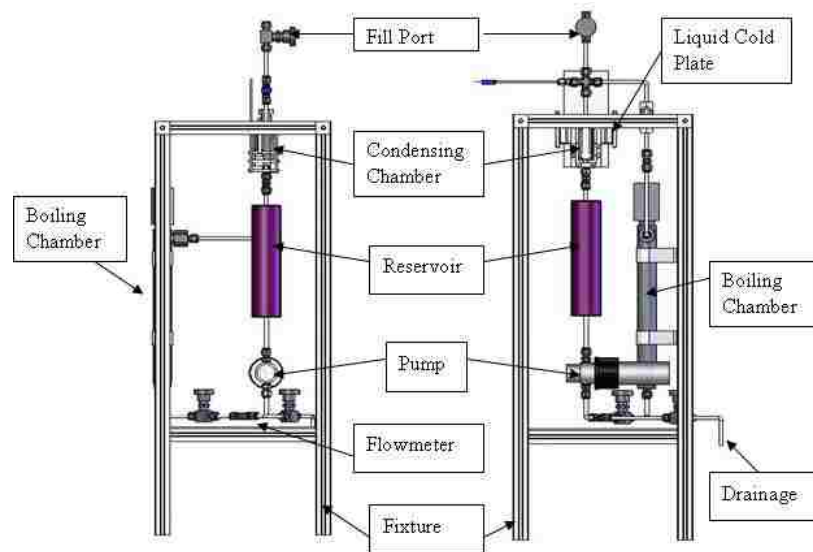


Figure 3.8 A solids model picture of the pumped flow loop test section is shown.

3.6 Thermal Performance Testing

This section contains a summary of all test data. For testing with water, data were acquired for wicked and polished test samples in the passive and pumped flow loop.

Data were not acquired for the fluorinert fluids since dropwise condensation was not exhibited. Data for methanol were only acquired on the passive flow loop with polished surfaces, since this was the only testing method that exhibited dropwise condensation.

3.6.1 Passive Loop System with Water

Experimental results with the passive loop system have been acquired for all test articles. Data has been obtained using water as the working fluid. All tests were taken at a saturation temperature of 100°C under vacuum. Data was acquired at four input powers (25W, 50W, 75W and 100W) over the 2.54cm by 1.27cm heat input section (heat fluxes between 7.75 W/cm² and 31 W/cm²). A plot of the experimental results is shown in Figure 3.9. Initial test data was acquired with the filmwise polished test article prepared chemically prepared oxide layer. The filmwise data was compared to the standard analytical Nusselt condensation heat transfer coefficient model for gravity aided filmwise condensation [13]. The acquired data agreed well with the correlation. The agreement of the filmwise condensation experimental data with the model qualifies the test section to acquire data for the less predictable dropwise condensation results.

Dropwise condensation data were acquired for a polished surface test article, a fine powder surface test article, a coarse powder surface test article, a single layer screen test article, and a double layer screen test article. All test articles were prepared with a self-assembled monolayer of octadecyl mercaptan to promote dropwise condensation. Overall the heat transfer coefficients measured on the dropwise surfaces were higher than that of filmwise condensation. The maximum heat transfer coefficient was measured on the coarse powder surface. It was 5~10 times larger than that of the filmwise condensation. The coarse pore size attainable with sintered powder was more beneficial

than the fine pore size attainable with sintered powder. The fine pore surface nearly matched the performance of the polished surface. The heat transfer coefficient improvement on the screen surfaces was minimal.

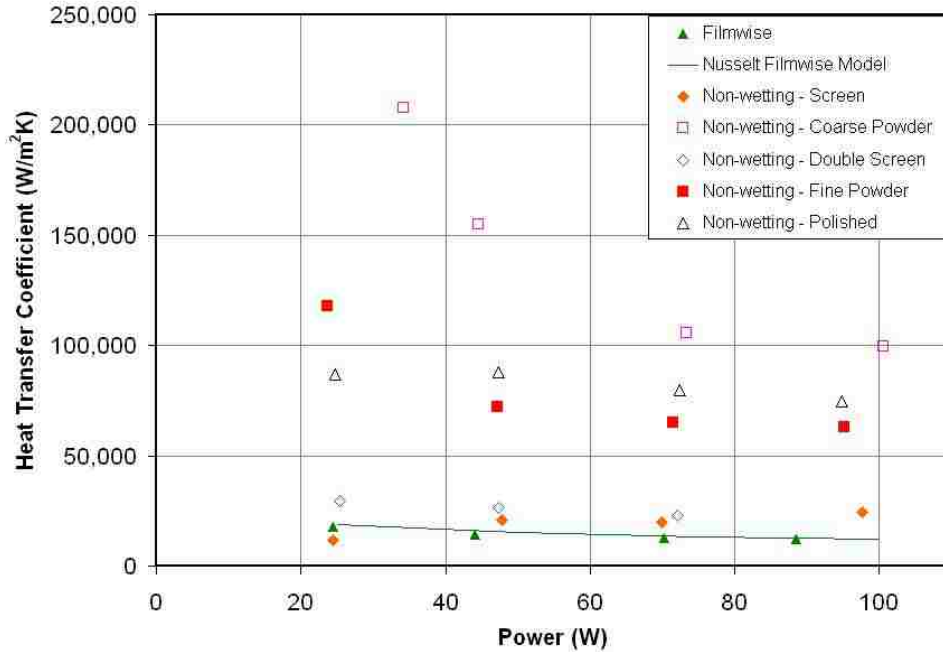


Figure 3.9 Experimental data for six test articles is shown: filmwise, dropwise on polished surface, dropwise on sintered fine powder surface, dropwise on sintered coarse powder surface, dropwise on single layer screen surface, and dropwise on double layer screen surface. Filmwise data is also compared to Nusselt condensation model.

The filmwise condensation data trends lower at higher flux as the additional liquid film reduces heat transfer. For dropwise condensation, the heat transfer coefficients fall rapidly as heat flux is increased. This phenomenon is more significant on surfaces with larger heat transfer coefficients. It is probably brought about by the reduction in the surface tension of water at higher temperatures. It is unclear without further experiments whether the heat transfer coefficient will continue to fall at higher heat fluxes.

3.6.2 Pumped Loop System with Water

Experimental results have been acquired from the forced flow test section for the dropwise test articles and the baseline filmwise test article. Data were only obtained using water as the working fluid. All tests were taken under vacuum. One purpose of the tests was to examine the performance of the dropwise condensation test articles under higher heat fluxes. The desired heat flux, according to the micro-channel heat exchanger design goal was to remove 5000W over a 25cm² area, or 200W/cm². The other goal was to study the relationship between the condensation heat transfer coefficient and the flow rate. By maintaining the saturation temperature and max power input, heat transfer coefficients were measured under varying fluid flow rate. The max power input was limited by the coolant unit and the attachment of the cold plate.

A plot of the comprehensive results is shown in Figure 3.10. The best result came from the coarse powder wick surface. The heat transfer coefficient was 12 times larger than from the filmwise baseline test article.

The baseline test article was polished and chemically prepared with an oxide layer. The filmwise condensation heat transfer coefficient showed a decreasing trend with an increasing in flow rate. The increased liquid quality as a result of the higher flow rates is one possible explanation of the net decrease in heat transfer.

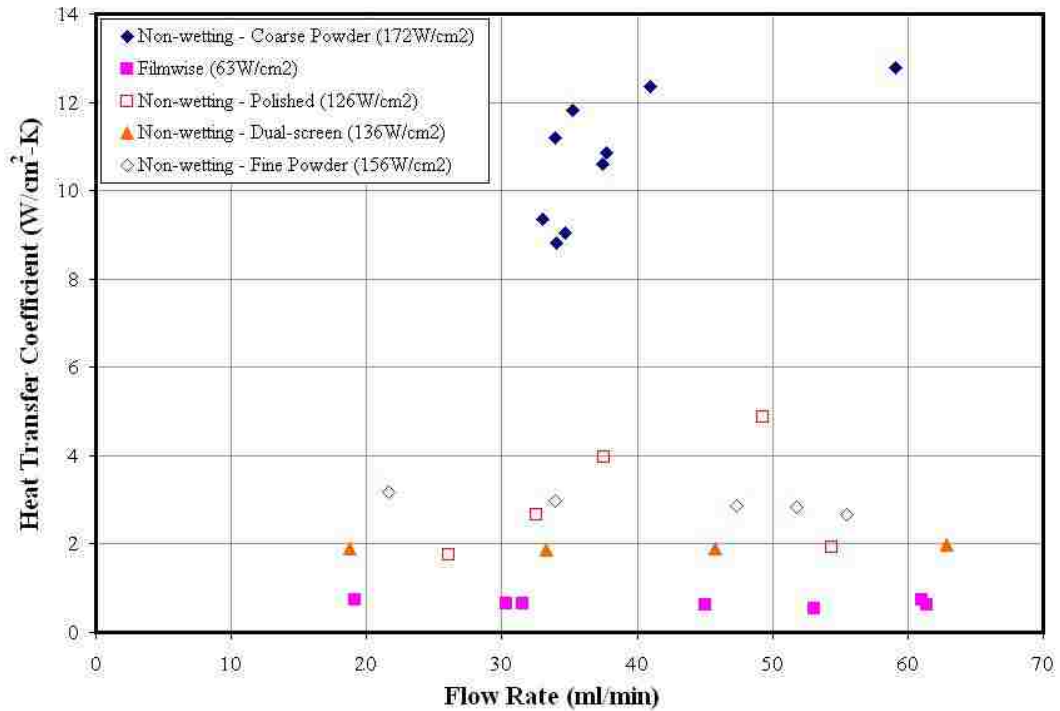


Figure 3.10 The heat transfer performance of the dropwise test articles versus the baseline filmwise test article with different flow rate is plotted.

Dropwise condensation data were acquired from the fine powder surface, coarse powder surface, polished surface and double screen surface test articles. The test articles were prepared with a self-assembled monolayer of octadecyl mercaptan to promote dropwise condensation. The coarse powder wick surface outperformed all other surfaces. Overall the sintered powder surfaces performed the best followed by polished base wall surface and then by the screen wick surfaces. All the above results were consistent with the results from the passive loop tests.

At elevated flow rate, three different trends were observed on the test articles. For the non-wetting polished surface, the heat transfer coefficient increased up to a

maximum value with increased fluid velocity and then started to decrease. This is believed to be caused by the increased coalescence between droplets blanketing the surface with a film of condensate. For the high performance sintered coarse powder surfaces, heat transfer coefficients showed some increasing trends with flow rate. Further experiments on this surface over higher power input might reveal the same trend showed on the non-wetting polished surface. For the rest of test articles, the heat transfer coefficients showed less variations with flow rate and lower values. This may be because dropwise condensation was not fully established on these surfaces.

3.6.3 Passive Loop System with Methanol

Polished surface dropwise test article was tested with methanol in the passive loop system. The test article was prepared with the same self-assembled monolayer of octadecyl mercaptan to promote dropwise condensation. The passive loop system was evacuated then charged with methanol. The saturation temperature of the system was kept at 70°C. Dropwise condensation was observed at the elevated power inputs 10 Watts, 20 Watts, 30 Watts and 40 Watts. Above 40 Watts condensation obviously turned transient and finally filmwise. The test results for non-wetting polished surface working with methanol and with water are displayed in Figure 3.11.

The heat transfer coefficient from the methanol system was extremely high at low power inputs where the dropwise condensation was better established. It was about 1.5 times larger than the maximum heat transfer coefficient from the water system. With the power elevated, the heat transfer coefficient dropped as the condensation turned from transient to filmwise. However, the benefit with applying non-wettable surface is still phenomenal. Further experiments need to be conducted with different working fluids and

on other surfaces.

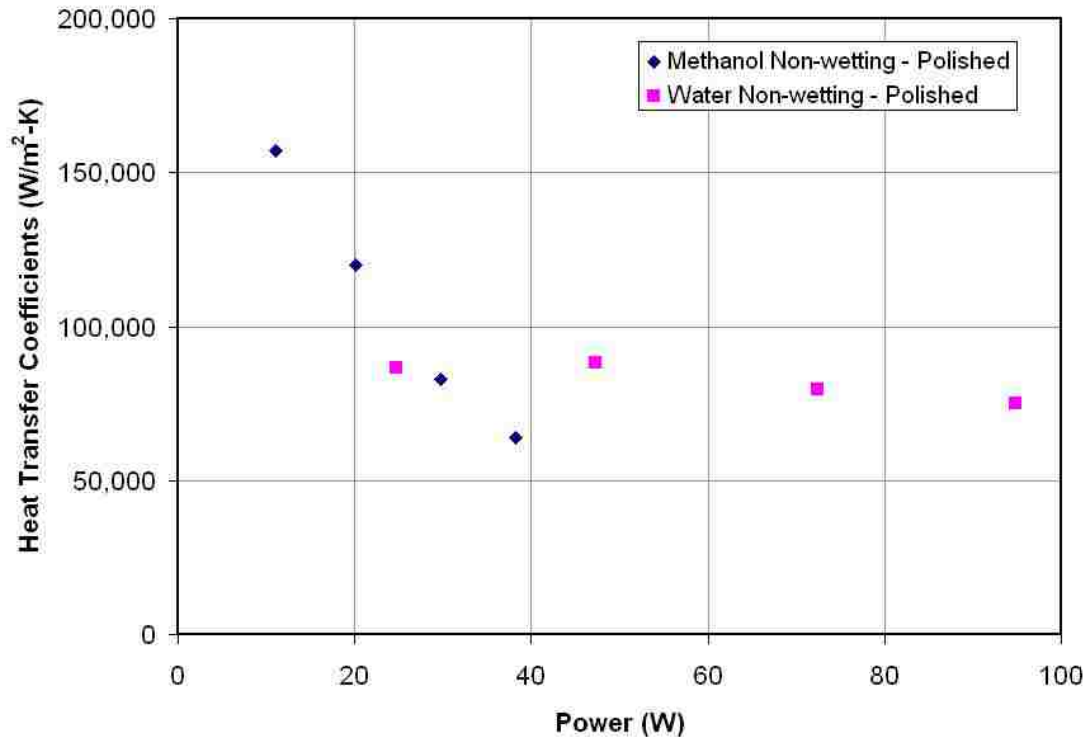


Figure 3.11 Experimental data for non-wetting polished test articles tested with water and with methanol. The saturation temperature was maintained at 100°C for water system and 70°C for methanol system.

3.7 Conclusions and Future Work

In conclusion, dropwise condensation with water on sintered wick structures shows great promise to enhance condensation. Sintered coarse powder and sintered fine powder test articles were successfully coated with SAMs. All enhanced test articles exhibited dropwise condensation with water, but not with other organic fluids. Heat transfer coefficients 5 to 20 times greater than filmwise condensation were attained with the dropwise condensation surfaces with water in the thermosyphoning configuration. The coarse power wick showed the greatest performance. In the pumped system, the heat

transfer coefficient from the coarse powder test article was above $100,000\text{W/m}^2\text{-K}$ with water as working fluid. The other non-wetting surfaces showed improvement in the pumped system, although the sub-cooled liquid length in the condenser caused the acquisition of accurate condensation measurements to be difficult. Methanol and fluorinert both showed some non-wettability on the polished copper surface. Methanol had a contact angle approaching 40° and the fluorinert was closer to 10° . The contact angle for methanol and fluorinert on the polished surface was not high enough to promote superhydrophobic effects on the wicked surfaces. In fact, wetting is promoted for both of these fluids. The contact angle for methanol was high enough to promote dropwise condensation on the polished surface. Heat transfer coefficients for methanol above $150,000\text{W/m}^2\text{-K}$ were measured, although a heat flux limitation existed. Dropwise condensation with the fluorinert was not observed. Further reduction in the surface energy of the polished surface is required.

Chapter 4

Heat Transfer Coefficient Modeling

4.1 Background and Introduction

Two generalized dropwise condensation heat transfer coefficient correlations (a heat flux dependent and a non-heat flux dependent) covering water and organic fluids are presented. The correlations accurately cover all fluids using two curve-fit parameters that are common to all fluids. The derived heat transfer coefficient correlations take the form of a power law expression. The generalized form of both correlations is derived by making several modifications to the Le Fevre and Rose model. Key additions to the Le Fevre and Rose model include the effect of contact angle on droplet height along with a complimentary method of estimating contact angle on well promoted surfaces. The final expression for the dropwise condensation Nusselt number re-emphasizes the view that dropwise condensation is a conduction heat transfer process limited primarily by the maximum departing droplet size, droplet height, and interfacial heat transfer coefficient. Using a data set which includes steam, propylene glycol, ethylene glycol and glycerol data, an error tolerance of +/- 15% is reported for 92% of the data and +/- 27% for all of the data using a non-heat flux dependent expression with common empirical coefficients. A heat flux dependent correlation is also presented which re-introduces a term that is neglected in the derivation of the non-heat flux dependent correlation. However, due to ambiguities between data acquired for water and especially some of the lower surface tension organic fluids, the heat flux dependent correlation is only recommended for water. Both models also match reasonably well with data acquired on inclined surfaces when a straight forward correction is made to the gravitational force acting on departing

droplets. A comment is also included on the effect of the promoter thermal resistance on dropwise condensation in light of recent theoretical and experimental results regarding the thermal resistance of promoter/water interfaces.

4.2 Nomenclature

A	Fractional surface area covered by all droplets of a given radius
B	Coefficient in Equation 21, equal to $-21.7m/N$
C_1	Coefficient related to conduction thermal resistance
C_2	Coefficient related to interfacial resistance
C_3	Coefficient related to departing droplet size
f	Fraction of surface covered by all droplets larger than a given radius
g	Gravitational constant
h	Heat transfer coefficient
h_{fg}	Heat of vaporization*
k	Liquid thermal conductivity*
L	Characteristic thermal length for dropwise condensation
Nu	Nusselt number
q	Heat flux through condensing surface
q_b	Heat flux through base of single droplet
r	Droplet radius
\hat{r}	Departing droplet radius**
\check{r}	Minimum droplet radius**
r_d	Expression for departing droplet radius***
r_i	Effective length scale equating conduction and interfacial resistance***

r_t	Minimum droplet radius***
R_g	Specific ideal gas constant
n	Empirical power law coefficient (related to droplet distribution)
m	Empirical coefficient power law coefficient for heat flux dependent expression
T_{sat}	Saturation temperature
T_s	Surface Temperature
ΔT	Difference between surface and saturation temperature

Greek Symbols

σ	Surface tension*
θ	Contact angle
ϕ	Surface inclination
ρ	Liquid density*
ρ_v	Vapor density*
π	Pi
γ	Constant pressure heat capacity ratio*

*All physical properties are evaluated at the saturation temperature of the fluid

**Specific to Le Fevre and Rose Model

***Specific to the Bonner Model

4.3 Introduction

Dropwise condensation has been of interest to the heat transfer community since its earliest published work in 1930 [16]. This ongoing interest is motivated by the observation that dropwise condensation promoted surfaces typically exhibit heat transfer coefficients at least five times higher (often exceeding ten times higher) than filmwise

condensation at similar operating conditions [1; 17]. Despite eight decades of research, a number of fundamental and practical issues remain unresolved in dropwise condensation research [18]. On the fundamental side, detailed theories on the dropwise condensation heat transfer mechanism exist and explain observed physics well. However, the most well recognized models for dropwise correlation heat transfer coefficients require four curve fit parameters. Further, these curve fit parameters vary from fluid to fluid in order to maintain sufficient accuracy. A single correlation for predicting dropwise condensation heat transfer coefficients for various fluids and surface inclinations is not available utilizing curve fit parameters common to all fluids. On the practical side of dropwise condensation research, long life coatings capable of promoting dropwise condensation for commercially viable systems are not available. However, recent results along with the emergence of electronics cooling applications with less demanding operating conditions (as compared to power generation and chemical production applications), show some hope that dropwise condensation can be implemented in commercial applications [4; 19; 20; 21].

In spite of the ongoing issues, research into dropwise condensation on advanced surfaces such as superhydrophobic surfaces capable of jumping droplets and surfaces with wettability gradients have been performed to address some of the second order issues, such as the reliance on gravity to remove condensing droplets [22; 23]. The ability to model these more advanced dropwise condensation heat transfer processes is difficult to achieve without better models for dropwise condensation on flat un-surface engineered surfaces [24].

The objective of this research effort was to present a generalized dropwise condensation heat transfer coefficient model that accurately models experimental data previously acquired for several fluids and temperatures [25]. Due to ambiguities between the heat flux dependency of data acquired for water and data acquired for organic fluids, a non-heat flux dependent and heat flux dependent model are presented. The non-heat flux dependent model actually works quite well for all fluids, as the measurement accuracy for dropwise condensations seems to be on the same order as the change in heat transfer associated with heat flux at typical operating conditions. The heat flux dependent model includes an additional term that accounts for additional droplet sub-cooling requirements at small radii, which improves the accuracy of the model when used with water.

In general, both models are derived by making several modifications to the Le Fevre and Rose model. In the derivation process, some of the original terms used in the Le Fevre and Rose model are neglected. However, the heat flux dependent correlation includes all of the effects that are captured in the Le Fevre and Rose model. Both models also include some physics not captured by the Le Fevre and Rose model, including the effect of contact angle on the droplet height. The generalized form also provides some clear insights into the heat transfer process. The correlations take the form of the familiar Nusselt expression, with the various power law terms in the denominator of the correlation representing the effective thermal length of the heat transfer process. The non-heat flux dependent model is able to accurately correlate most of the data to with +/- 15% using only 2 coefficients which are common to each fluid. This achievement compares favorably with the Le Fevre and Rose model, which uses 4 empirical

coefficients. Further, these four coefficients vary from fluid to fluid in order to achieve reasonable accuracy, compared with the presented correlations having common empirical coefficients.

The heat flux dependent correlation includes a term to account for the increase in heat transfer coefficient (primarily with water) at higher heat fluxes. However, the heat flux dependent model actually results in decreased accuracy with the organic fluid data. The decrease in accuracy is likely due to the propensity of the lower surface tension fluids to experience critical heat flux limitations on parts of the surface as heat flux is increased. Both of the described models are also compared to some data acquired on inclined surfaces. Good agreement is observed with both models when a straight forward modification to the gravitational force term is performed.

This chapter describes the derivation of two generalized dropwise condensation heat transfer coefficient correlations, including a non-heat flux and heat flux dependent model. An extensive overview of the Le Fevre and Rose theory is provided since the theory serves as a starting point for deriving the functional form of the correlation. In the accompanying section, modifications to the Le Fevre and Rose model are described in detail. The three primary modifications required to arrive at the non-heat flux dependent expression include (1) neglecting the term that accounts for the additional sub-cooling required to condense on small droplets (due to surface curvature), (2) replacement of the lower limit term with the radius that equates the interfacial resistance (due to mass transfer resistance) and droplet conduction resistance, and (3) corresponding elimination of the interfacial resistance term in the integrand. The neglecting of terms is purely a mathematical manipulation to arrive at a workable power law expression, and not an

indication that these terms are not important. In fact, all of the physics represented by these temporarily neglected terms are accounted for in the heat flux dependent expression. Heat flux dependency is accomplished by re-introducing a term that describes the added sub-cooling required to condense on the surface of small droplets by treating the term as a thermal resistance to heat transfer. The model also accounts for the change in droplet height due to the change in contact angle, which is not present in the Le Fevre and Rose model.

4.4 Le Fevre and Rose Theory

The Le Fevre and Rose theory develops a prediction for the average dropwise condensation heat transfer coefficient by integrating the heat flux contribution of each individual droplet size over the distribution of droplet sizes present on the surface [26; 27]. One tenet of the theory is that the droplet distribution can be modeled as fixed even though the droplet size at any location is highly transient and the distribution across the entire surface oscillates around the time averaged distribution [28]. For the size distribution of droplets, a power law type distribution is used, where f is a cumulative distribution function that signifies the fraction of droplets greater than the radius, r (Eq. 4.1). The function predicts that no droplets are greater than the departing droplet radius. Empirical evidence has shown the proposed functional form for the cumulative distribution to be valid with the empirical coefficient n equal to 1/3. In order to evaluate the total area contributed by drops of a given radius between n and $r + dr$, it is desirable to re-write the distribution as stated in Eq. 4.2.

$$\text{Eq. 4.1} \quad f = 1 - \left(\frac{r}{\hat{r}}\right)^n$$

$$\text{Eq. 4.2} \quad A(r)dr = n \left(\frac{r}{\hat{r}}\right)^{n-1} \frac{dr}{\hat{r}}$$

Eq. 4.3 describes the heat flux through a single droplet by using a thermal resistance network approach. The numerator describes the thermal driving force across an arbitrary droplet size, accounting for the additional sub-cooling required to condense on a curved vapor liquid interface. The additional sub-cooling term can be derived by equating the pressure differences predicted by the Clapeyron Equation and the Kelvin Equation. The denominator accounts for two thermal resistances. The first term is a simple conduction resistance coupled with a quasi-empirical shape factor to account for the droplets hemispherical shape, deviation in contact angle from 90°, and contact angle hysteresis. The second term accounts for the thermal resistance across the liquid vapor interface attributed to imperfect accommodation of vapor as the vapor impacts and condenses on the liquid surface of the droplet.

$$\text{Eq. 4.3} \quad q_b = \frac{\Delta T - \frac{2\sigma T_{sat}}{r\rho h_{fg}}}{\frac{c_1 r}{k} + \frac{c_2 T_{sat}(\gamma+1)}{\rho_v h_{fg}^2(\gamma-1)} \left(\frac{RgT_{sat}}{2\pi}\right)^{1/2}}$$

Eq. 4.2 and Eq. 4.3 are combined and integrated over the entire droplet distribution in Eq. 4.4 to calculate the average heat flux through a surface. The upper limit for integration is the droplet departing size given in Eq. 4.5 which includes an empirical coefficient to match data. In actuality, the $(\sigma/\rho g)^{1/2}$ term represents the maximum length at which a surface tension can hold a liquid droplet spherical under its own weight. However, the term is correct if the contact angle hysteresis is included in the numerator. Given the difficulties in predicting, measuring, and estimating contact

angle hysteresis, the use of $(\sigma/\rho g)^{1/2}$ with an empirical factor is justified. The magnitude of the term and the empirical factor have been confirmed from visual observation of droplets falling during condensation. The minimum droplet radius that is sustainable without evaporating due to the high vapor pressure created by the curved droplet surface serves as the lower limit of integration (Eq. 4.6). This term is directly related to the sub-cooling term in the numerator of Eq. 4.4.

$$\text{Eq. 4.4} \quad q = \frac{n}{\hat{r}^n} \int_{\check{r}}^{\hat{r}} \left\{ \frac{\Delta T - \frac{2\sigma T_{sat}}{r \rho h_{fg}}}{\left(\frac{c_1 r}{k} + \frac{c_2 T_{sat} (\gamma+1)}{\rho v h_{fg}^2 (\gamma-1)} \right) \left(\frac{R g T_{sat}}{2\pi} \right)^{1/2}} \right\} r^{n-1} dr$$

$$\text{Eq. 4.5} \quad \hat{r} = C_3 \left(\frac{\sigma}{\rho g} \right)^{1/2}$$

$$\text{Eq. 4.6} \quad \check{r} = \frac{2\sigma T_{sat}}{\rho h_{fg} \Delta T}$$

The Le Fevre and Rose model accurately explains many of the observed phenomena associated with dropwise condensation heat transfer. However, the use of four adjustable parameters which require additional adjustment when extrapolating the theory to fluids other than water has lent the theory to some criticisms. In the theories' defense, some of the adjustable parameters have been independently verified through non-condensation related experiments and analytical solutions, somewhat reducing the theories' reliance on empiricism. The use of an integral expression to calculate heat flux is also inconvenient. Evaluating the integral expression may not be straight forward for practicing engineers, as the interval spans several orders of magnitude. However, analytical solutions to the Le Fevre and Rose model exist, and modern computational tools can certainly evaluate the required integrals.

4.5 Bonner Model

The derivation of the Bonner model begins with the aforementioned Le Fevre and Rose model. No changes are made to the distribution equations (Eq. 4.1 and Eq. 4.2) in the Le Fevre and Rose model. The first improvement is made to Eq. 4.3 by accounting for the change in the height of the droplet as a function of droplet height. This only affects the conduction term in the denominator of Eq. 4.7. At this point in the derivation, the shape factor C_1 is still included in the expression, although the inclusion will prove to be insignificant to the final correlation.

$$\text{Eq. 4.7} \quad q_b = \frac{\Delta T \frac{2\sigma T_{sat}}{r\rho h_{fg}}}{\frac{C_1 r}{k} \frac{1-\cos\theta}{\sin\theta} + \frac{C_2 T_{sat}}{\rho_v h_{fg}^2} \left(\frac{\gamma+1}{\gamma-1}\right) \left(\frac{R_g T_{sat}}{2\pi}\right)^{1/2}}$$

Eq. 4.8 shows a revised expression for Eq. 4.4 including the revised conduction term. From here, several changes are made in order to modify the expression so that the expression can be readily integrated in closed form. (It should be noted that Eq. 4.4 can be integrated analytically but the form is very complicated). The modifications were inspired by graphical inspection of the plot of relative heat flux contribution versus droplet radius. A plot of the relative heat flux as predicted by the Le Fevre and Rose model versus radius for steam at 100°C and 3°C sub-cooling is shown in Figure 4.1 for discussion purposes. The data in Figure 4.1 was generated using the Le Fevre and Rose Model and plotting the heat flux contribution when integrating with a step size that was proportional to the radius. Because the actual heat flux depends on the magnitude of the step size, the plot represents the relative heat flux contribution for all droplets of a given

radius. Although simply plotting heat flux versus radius seems more straight forward, the large variations in radius (over four orders of magnitude) distorts the plot.

At small radii (in Figure 4.1), the combination of the thermal driving force loss due to droplet surface curvature and the interfacial heat transfer coefficient thermal resistance acts to limit heat transfer. At larger radii, heat transfer is limited by conduction through the relatively tall drops. The total relative heat flux curve shows a characteristic maximum value that can be predicted by the intersection of the interface resistance and conduction resistance curve. The total heat flux contribution, or area under the relative heat flux contribution curve, is broken up into two portions: a "left" portion spanning from \check{r} to the radius where the maximum relative heat flux is observed and a "right" portion (grayed area of Figure 4.1) spanning from the radius where the maximum value of the relative heat flux curve is observed to \hat{r} . By observing several of these curves at different conditions, these portions were noticed to be of approximate equal size. Therefore, only one side of the integral in Eq. 4.7 needs to be evaluated since the value of either integral will be proportional to the total heat flux. The right side of the integral is chosen over the left side because both the sub-cooling due to curvature term and interfacial resistance term can be neglected at large radii which simplifies the derivation process. Furthermore, the right portion seems to be the slightly larger of the two portions. The original lower limit \check{r} in Eq. 4.8 is replaced with r_i . Since r_i is expected to occur when the conduction and interfacial thermal resistance are approximately equal, an expression for r_i can be developed by equating the conduction and interfacial resistance terms as shown in Eq. 4.9 and Eq. 4.10. After making these changes Eq. 4.8 is transformed into Eq. 4.11.

$$\text{Eq. 4.8} \quad q = \frac{n}{\hat{r}^n} \int_{\hat{r}}^{\hat{r}} \left\{ \frac{\Delta T - \frac{2\sigma T_{sat}}{r \rho h_{fg}}}{\left(\frac{C_1 r}{k} \frac{1-\cos\theta}{\sin\theta} + \frac{C_2 T_{sat} (\gamma+1)}{\rho_v h_{fg}^2 (\gamma-1)} \left(\frac{R_g T_{sat}}{2\pi} \right)^{1/2} \right)} \right\} r^{n-1} dr$$

$$\text{Eq. 4.9} \quad \frac{C_1 r}{k} \frac{1-\cos\theta}{\sin\theta} \cong \frac{C_2 T_{sat} (\gamma+1)}{\rho_v h_{fg}^2 (\gamma-1)} \left(\frac{R_g T_{sat}}{2\pi} \right)^{1/2}$$

$$\text{Eq. 4.10} \quad r_i = \frac{k T_{sat}}{\rho_v h_{fg}^2} \left(\frac{\sin\theta}{1-\cos\theta} \right) \left(\frac{\gamma+1}{\gamma-1} \right) \left(\frac{R_g T_{sat}}{2\pi} \right)^{1/2}$$

$$\text{Eq. 4.11} \quad q = \frac{n}{\hat{r}^n} \int_{\hat{r}}^{\hat{r}} \left\{ \frac{\Delta T}{\left(\frac{C_1 r}{k} \frac{1-\cos\theta}{\sin\theta} \right)} \right\} r^{n-1} dr$$

Without the curvature term in the numerator, the equation can be rearranged to solve for the heat transfer coefficient directly according to Eq. 4.12. As shown in Eq. 4.13, this results in an integral that can be readily solved analytically. After integrating and realizing that the second term associated with the upper limit is negligible, all of the empirical proportionality coefficients can be lumped into a single empirical proportionally constant as shown in Eq. 4.15. Also note that \hat{r} has been replaced with r_d , as the empirical coefficient associated with this term can be lumped in with the all of the other empirical coefficients (Eq. 4.14). Further inspection of Eq. 4.16 shows the equation to be in the form of the familiar Nusselt Number (Eq. 4.16), Nu , where $r_d^n r_i^{1-n} \frac{1-\cos\theta}{\sin\theta}$ is the effective thermal length for condensation and the final proportionality constant is in fact the dropwise condensation Nusselt Number (Eq. 4.17).

$$\text{Eq. 4.12} \quad h = \frac{q}{\Delta T}$$

$$\text{Eq. 4.13} \quad h = \frac{n C_3^{-n}}{C_1} \frac{\sin\theta}{1-\cos\theta} \frac{k}{r_d^n} \int_{r_i}^{r_d} r^{n-2} dr$$

$$\text{Eq. 4.14} \quad r_d = \left(\frac{\sigma}{\rho g} \right)^{1/2}$$

$$\text{Eq. 4.15} \quad h = \frac{C_2^{n-1} C_3^{-n}}{C_1} \frac{n}{1-n} \frac{k}{r_d^n r_i^{1-n}} \left(\frac{\sin\theta}{1-\cos\theta} \right)$$

$$\text{Eq. 4.16} \quad Nu = \frac{hL}{k}$$

$$\text{Eq. 4.17} \quad Nu = \frac{c_2^{n-1} c_3^{-n}}{c_1} \frac{n}{1-n}$$

Eq. 4.18 presents the generalized expression for the non-heat flux dependent dropwise condensation heat transfer coefficient. Although there are two power law coefficients for r_d and r_i that need to be determined, they both depend solely on one changeable coefficient, n . It is no coincidence that the power law coefficients sum to unity, such that the effective thermal length term $r_d^n r_i^{1-n} \frac{1-\cos\theta}{\sin\theta}$ always has dimension of unit length regardless the value of n . The only two unknowns are the value for n and the Nu number which need to be determined from experimental data. To avoid confusion, further emphasis is placed on the fact that r_i represents the droplet height at which the interfacial resistance and conduction resistance are equal and not the minimum droplet size present on the surface.

$$\text{Eq. 4.18} \quad h = Nu \frac{k}{r_d^n r_i^{1-n}} \left(\frac{\sin\theta}{1-\cos\theta} \right)$$

Eq. 4.18 does not include a mechanism for capturing the heat flux dependency of the dropwise condensation heat transfer coefficient. To complicate matters, data acquired for water and organic fluids are not in complete agreement, as water tends to show an increase in heat transfer with heat flux while some of the organic fluids show zero change (constant heat transfer coefficient) or a continual decrease in heat transfer coefficient with increasing heat flux. Despite the discrepancies, a model which captures the heat flux effect for water (even if it doesn't work for organic fluids) is highly desired for practical purposes. To account for the heat flux dependency, the Kelvin/Clapeyron term

previously used to represent the minimum droplet radius is reintroduced into the heat transfer coefficient expression by treating the term as a thermal resistance (rather than as a loss of driving force). This term is renamed r_t , although it is equivalent to the previous minimum droplet radius expression for \check{r} . To maintain the unit length dimension of the denominator in Eq. 4.20, the power law coefficients require rebalancing. A ratio of 2:1 for the power law coefficients of r_d and r_i is maintained to stay consistent with the exponent ratio found when empirical data is fit to Eq. 4.18 (as will be shown in section 4.6 Comparison to Data).

$$\text{Eq. 4.19} \quad r_t = \check{r} = \frac{2\sigma T_{sat}}{\rho h_f g \Delta T}$$

$$\text{Eq. 4.20} \quad h = Nu \frac{k}{r_d^m r_i^{m/2} r_t^{1-3m/2}} \left(\frac{\sin \theta}{1 - \cos \theta} \right)$$

The expressions above require knowledge of the contact angle for quantitative evaluation. This data is often difficult to measure and difficult to find, especially for fluids other than water. In order to evaluate the contact angle as a function of only the fluid's surface tension, a convenient equation has been developed for use with the Bonner model (Eq. 4.18, Eq. 4.20, Eq. 4.22, and Eq. 4.23). The equation was derived using Zisman's theory, which has been applied to estimate contact angles of organic and aqueous fluids on smooth surfaces [29]. According to Zisman's theory, the cosine of the contact angle on a surface has a linear relationship with the surface tension of the fluid. The surface can be characterized with a single value defined as the surface energy of the surface. The surface energy (same units as surface tension) is defined as the value of the maximum surface tension which wets the surface with zero contact angle (complete spreading). The surface energy of the surface is generally found by plotting the cosine of

measured contact angles for several fluids against the fluids' surface tension, and determining the point at which a linear curve fit intersects the line $\cos \theta = 1$.

Using this theory, an equation for estimating the contact angle contact on well promoted dropwise condensation surfaces was developed using Zisman's linear relationship and two assumed data points. The first data point was determined from consistent observations by generally all dropwise condensation researchers that the contact angle for water on well promoted smooth surfaces is usually around 100° at room temperature. The second point used to determine the slope and intercept in Eq. 4.21 was determined by estimating that the surface energy of the well promoted surfaces are 18 mN/m, consistent with the range of most hydrophobic self-assembled monolayer coated surfaces. Although the exact surface energy values changes based on the promoter type and surface preparation techniques, the deviation is probably with 10-15% for most well prepared surfaces. The chosen value actually isn't of utmost importance since the empirical nature of the correlation will dampen out any small errors in the surface energy. With this in mind, Eq. 4.21 is only recommended for the purpose of estimating the contact angle of various fluids on well promoted smooth surfaces while evaluating the Bonner model.

$$\text{Eq. 4.21} \quad \cos \theta = B\sigma + 1.39$$

4.6 Comparison to Data

Dropwise condensation data were mined from several sources. From each source, heat transfer coefficient data were digitally extracted from plots of heat flux versus ΔT acquired at constant saturation temperatures. Between one and two dozen points were

extracted from each curve such that the entire length of each curve was represented, not including data that showed significant signs of filmwise transitioning (which only affected the organic fluids). Overall, two sources of data were utilized resulting in 218 data points, including data acquired with four different fluids, including:

- Stylianou [30]: Water at 374 K, 366 K, 359 K, 348 K, 333 K, 321 K
- Utaka [31]: Ethylene Glycol at 428 K, 368 K, Propylene Glycol at 408 K, 388 K, 363 K and Glycerol at 423K

For plotting purposes, these data points acquired at each temperature were averaged so that only one data point existed for each saturation temperature. Figure 4.2 shows the experimental data versus Eq. 4.18 using a value of n equal to $2/3$ to evaluate the power law coefficients above r_i and r_a . A plot redundant to Figure 4.2 is shown in Figure 4.3 using all of the extracted data points. Figure 4.3 highlights the scatter present in raw (un-averaged) data, particularly at low ΔT 's where even small measurement errors result in large variations in the measured heat transfer coefficient. The value of n used in both plots was found by manual iteration such that the regression line residual was minimized. The slope of the regression line, equal to the Nu number in Eq. 4.18, is 33. The value of n is not in agreement with the experimental droplet distribution data associated with the Le Fevre and Rose theory and Glicksman [28] that shows the value of n to be approximately $1/3$. This disagreement is probably due to the simplifications that were made in order to derive Eq. 4.18 and certainly not a reason to distrust the previously acquired droplet distribution data. Overall, the data falls nicely on the proposed curve, showing that the general form of the correlation captures the physics of the dropwise condensation process well. As compared to the Le Fevre and Rose theory, the underlying

physics are not all that different except for the inclusion of contact angle related effects. A large portion of the accuracy improvement may be due to the more manageable form of Eq. 4.18 and completely empirical nature in which all of the empirical coefficients were determined.

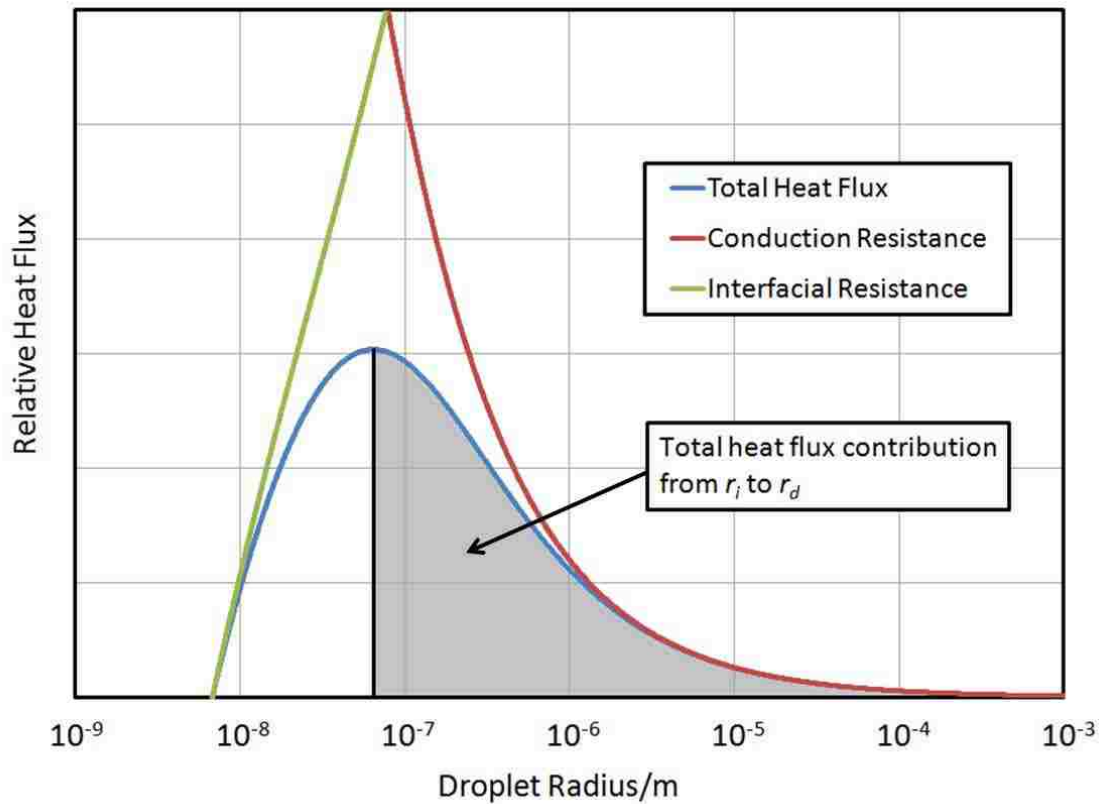


Figure 4.1 The relative heat flux contribution for all droplets of a given radius as a function of droplet radius as predicted by the Le Fevre and Rose model is plotted. The relative heat flux contribution of only the conduction and only the interfacial resistance is also plotted. The intersection of the two lines graphically depicts r_i . The Bonner model is derived by estimating that the maximum relative heat flux occurs at the droplet radius where the conduction and interface resistances are equal. The Bonner model also assumes that the relative heat flux contributed by droplets larger than r_i and smaller than r_i , are approximately equal. Therefore, the total dropwise condensation heat flux should be proportional to the value of either half of the integral.

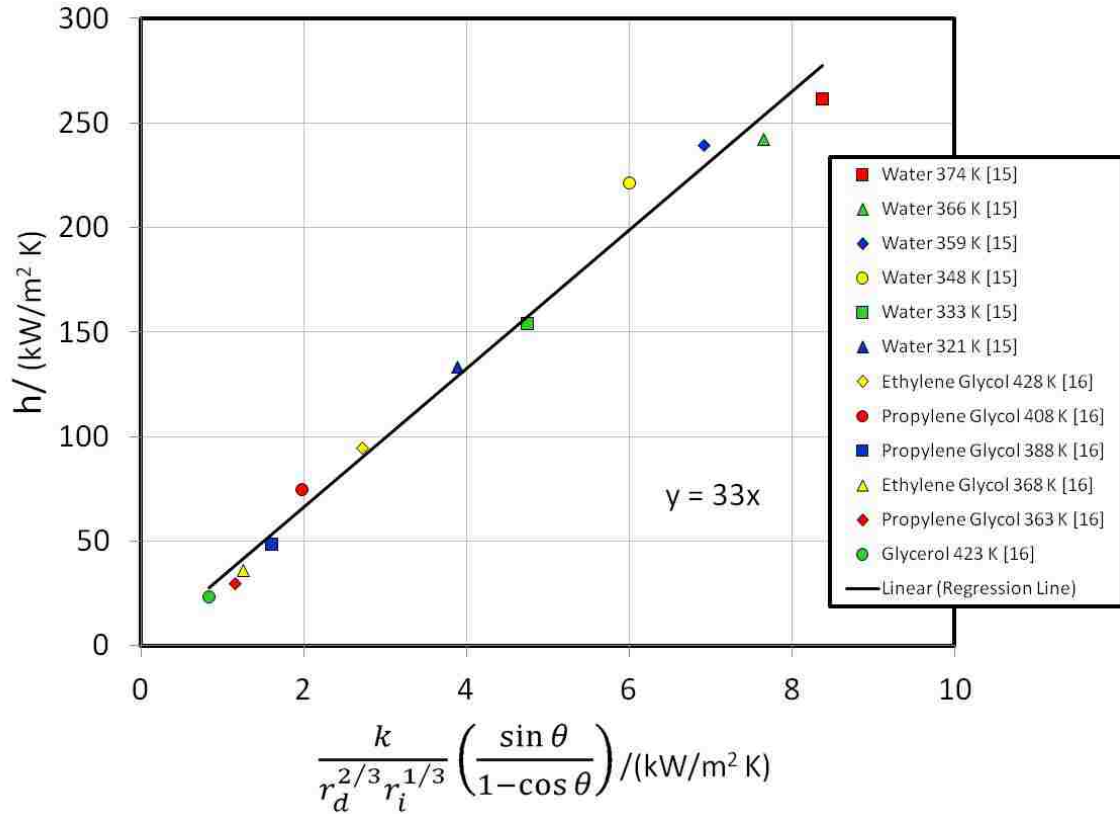


Figure 4.2 Experimental heat transfer coefficients averaged with respect to heat flux (for data acquired at constant temperature) are plotted against a term in non heat flux dependent Bonner model with n equal to $2/3$. The slope of the regression line is equal to the dropwise condensation Nusselt number for the non heat flux dependent Bonner Model.

The final equation for the non-heat flux dependent heat transfer coefficient is provided below in Eq. 4.22. Eq. 4.21 should be used to estimate the contact angle along with Eq. 4.10 for r_i and Eq. 4.14 for r_d . All physical properties should be evaluated at the saturation temperature. The saturation temperature was chosen rather than the wall temperature to avoid the requirement of an iterative process in order to evaluate the heat transfer coefficient. This approximation is generally valid since the wall to fluid temperature difference is usually small in dropwise condensation.

$$\text{Eq. 4.22} \quad h = 33 \frac{k}{r_d^{2/3} r_i^{1/3}} \left(\frac{\sin \theta}{1 - \cos \theta} \right)$$

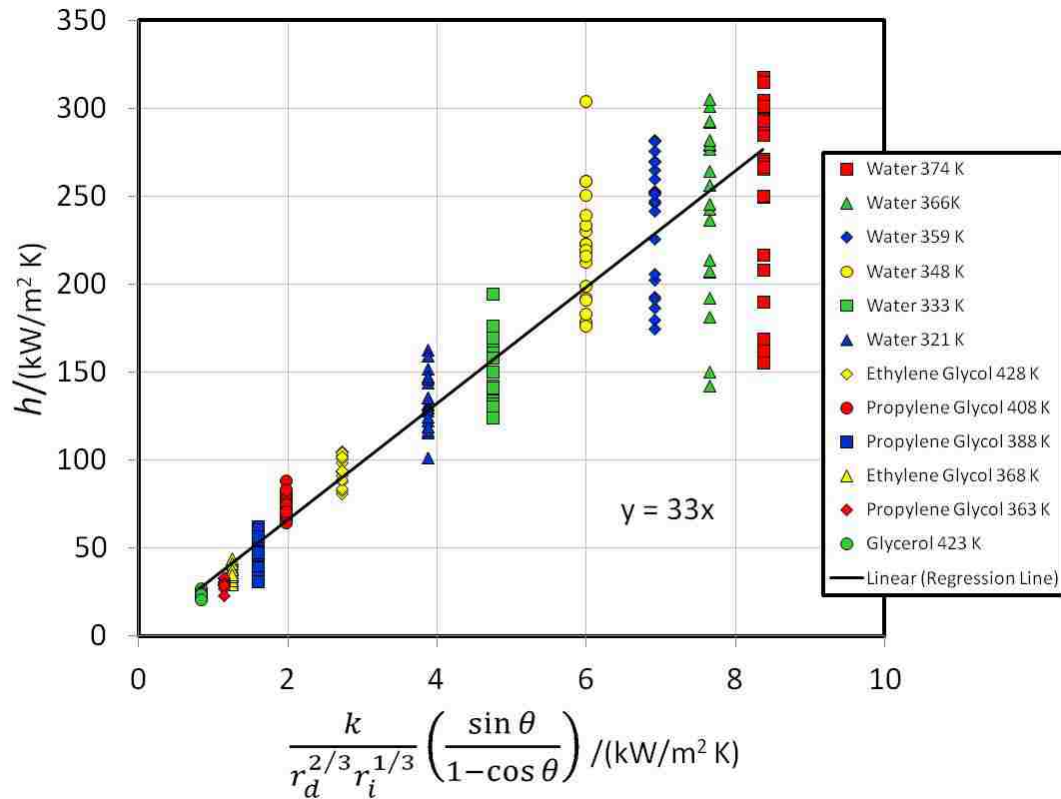


Figure 4.3 Experimental heat transfer coefficient data are plotted against a term in the non-heat flux dependent Bonner Model (similar to Figure 4.2, with all of the data, rather than averaged data plotted).

Some of the scatter in the data may also be attributed to the lack of a heat flux dependent term in Eq. 4.18. Less scatter is observed along with higher accuracy for water by refitting all of the data to the heat flux dependent Eq. 4.20 as shown in Figure 4.4. However, less accuracy is observed for most of the organic fluid data. Eq. 4.23 shows the final form of Eq. 4.20 when the empirical coefficients are evaluated (with m equal to 1/2).

Eq. 4.23

$$h = 2.7 \frac{k}{r_d^{1/2} r_i^{1/4} r_t^{1/4}} \left(\frac{\sin \theta}{1 - \cos \theta} \right)$$

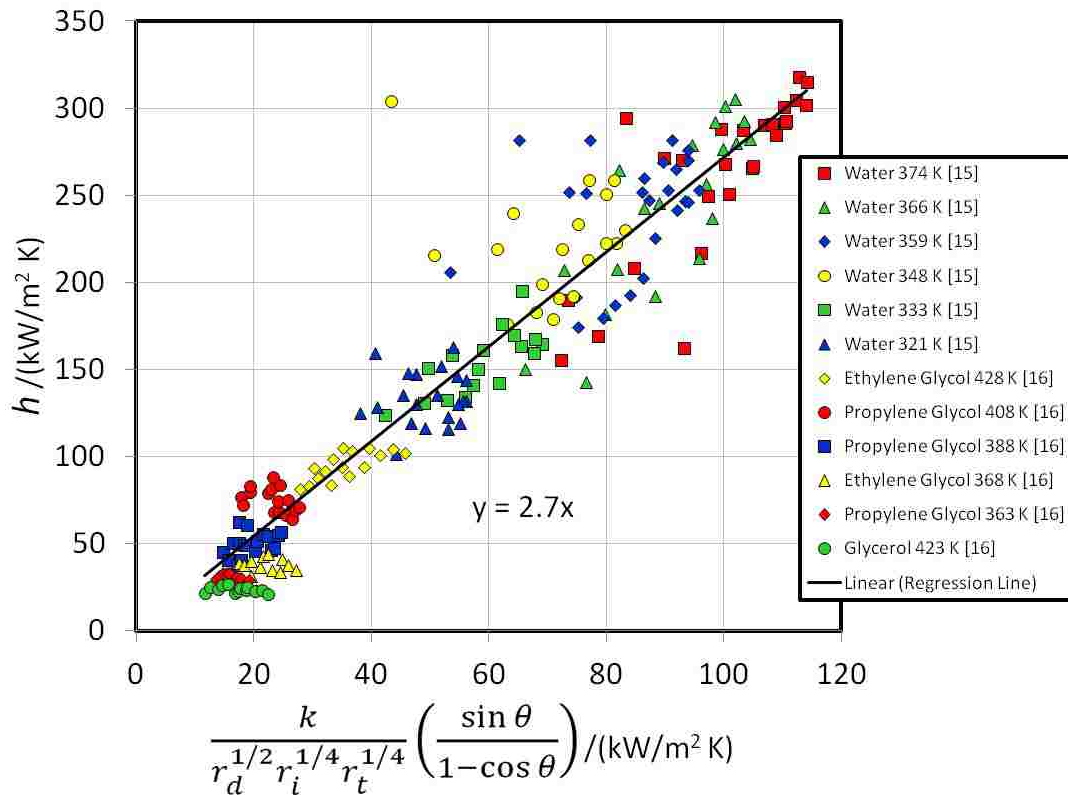


Figure 4.4 Experimental heat transfer coefficients are plotted against the term in the heat flux dependent Bonner model with m equal to $1/2$ [30][31]. The slope of the line is equal to the dropwise condensation Nusselt number for the heat flux dependent Bonner model.

To get a better feel for the accuracy of both models, all of the acquired data along with both models (Eq. 4.22 and Eq. 4.23) are plotted in Figure A.1 through A.12. Generally, higher accuracy and better heat flux trends are observed with water. With the organic fluids, some of the data remains in agreement with the heat flux dependent model (Eq. 4.23) although some of the data departs. This is unavoidable, as some of the organic fluid data actually shows an opposite (decreasing heat transfer coefficient) trend with

higher heat flux. The organic data is better represented by the non-heat flux dependent expression. The organic fluid data probably decreases with heat flux because partial flooding of the surface begins as heat flux is increased, which causes inefficient filmwise condensation to partially blanket the surface. To get better accuracy with the organic fluids, a term that depends on the onset of the condensation critical heat flux could be included.

4.7 Surface Inclination

A natural challenge to the Bonner model is to predict heat transfer coefficients acquired at different orientations. Koch has acquired data at different orientations for steam at 100°C [32]. Although the data taken in the vertical condition is not in agreement with the Bonner model or Le Fevre and Rose model (possibly due to non-condensable gas), the data can still be used to test the ability of the new correlation to capture the inclination effect. If the Bonner correlation is correct such that only the gravitational force acting on the departing droplet changes, then the heat transfer coefficient should scale linearly with $(g \sin \phi)^{1/3}$ or $(g \sin \phi)^{1/4}(g \sin \phi)^{1/3}$.

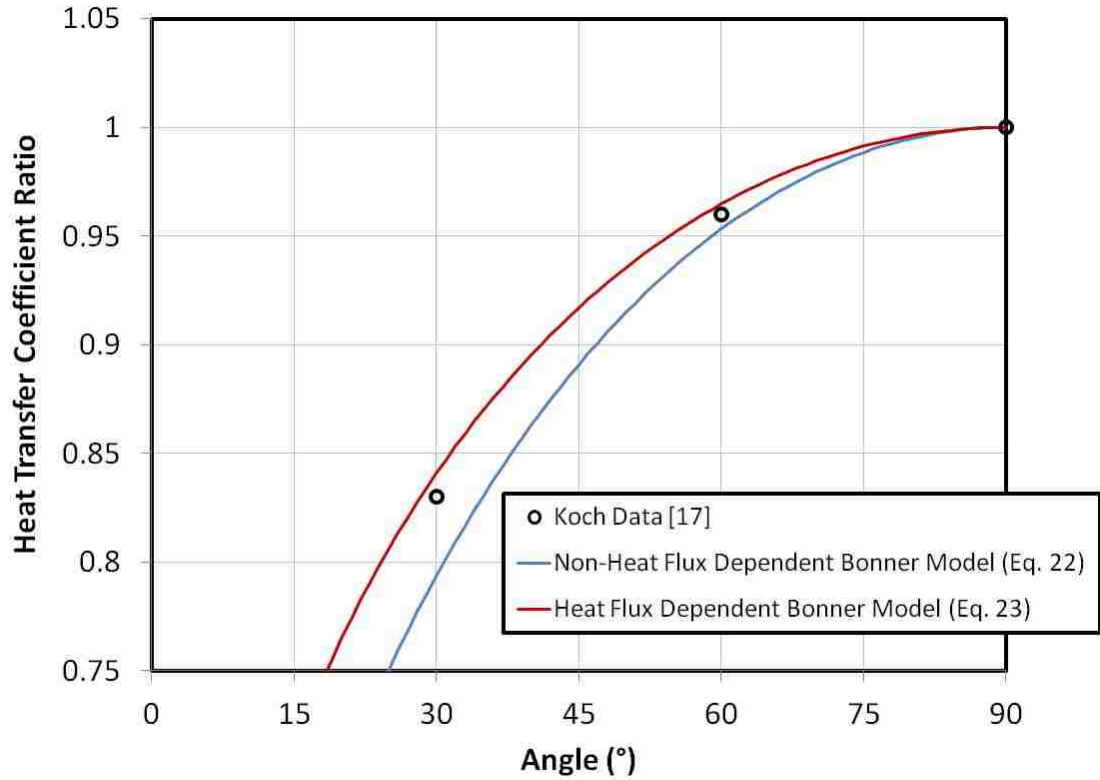


Figure 4.5 Comparison of the derived $(g \sin \phi)^{1/3}$ term in the non-heat flux dependent Bonner model (Eq. 4.22) and the $(g \sin \phi)^{1/4}$ term used in the heat flux dependent Bonner model (Eq. 4.23) to relative (to completely vertical) heat transfer coefficient data acquired at various inclinations by Koch [32].

As shown in Figure 4.5, the gravitational scaling in the non-heat flux dependent and heat flux dependent Bonner correlations (Eq. 4.22 and Eq. 4.23) matches that of the Koch data. In fact, Koch matched data for non-suspended droplets with an identical term where the exponent was equal to 0.270, in good agreement with the value of 1/3 and 1/4 used in Eq. 4.22 and Eq. 4.23. Therefore, it is recommended that either Bonner correlation be used for inclined surfaces by substituting the g in r_d with $g \sin \phi$.

4.8 Considering the Promoter Resistance

The effect of the promoter resistance is not present in the Bonner model although a number of researchers have previously investigated the effect of the promoter thermal resistance on the dropwise condensation heat transfer coefficient [33; 34]. In the previous work, the thermal resistance of the promoter was modeled as a conduction thermal resistance, using the thermal conductivity of the promoter and its thickness to calculate a thermal resistance. However, this is only accurate if the coating thickness is greater than the Kapitza length of the interface. Although this may be the case for some of the thicker PTFE coatings that are sometimes used, it is not the case for monolayer promoters. At the length scale of promoters ($\sim 2\text{nm}$) the interacting phonon and fluid particle interactions between the metal, promoter and liquid play a role in the thermal interface resistance. Researchers have separately performed molecular level modeling and experimental testing of these interfaces showing the interface conductance for a hydrophobic self-assembled monolayer on a metal surface in contact with water to be on the order of $50\text{-}100\text{ MW/m}^2\text{ K}$ [35; 36]. As discussed previously, r_i (Eq. 4.19) is near the point of maximum heat transfer in the heat flux versus radius plot of Fig. 1. Comparing the conduction resistance at r_i for steam at 100°C of $\sim 6\text{ MW/m}^2\text{ K}$ (using r_i/k) shows the promoter resistance to be an order of magnitude smaller than the conduction resistance. Since r_i was derived by equating the conduction resistance with the interfacial thermal resistance on the droplet/vapor interface, we can also say that the promoter resistance is an order of magnitude smaller than the total droplet thermal resistance.

4.9 Wettability or Surface Energy Gradients

Several researchers have investigated the use of surfaces with graded wettability (through a surface energy gradient) to enhance dropwise condensation while decreasing the detrimental effects of adverse elevation [11; 22; 37; 38; 39]. Surface energy gradients (or wettability gradients) have the ability to move droplets placed on the hydrophobic side of the gradient to the hydrophilic side without the aid of additional gravitational, shear or capillary forces that are generally required. In fact, droplets placed on the surfaces can even move “uphill” against gravity [12].

Figure 2.1 shows a physical description of how droplet motion is generated on a surface possessing a surface energy gradient. Since the surface is steadily decreasing from hydrophobic to hydrophilic, a droplet placed on the surface experiences two differing contact angles with the higher contact angle located on the more hydrophobic side of the droplet. The difference in contact angle across the droplet creates a Young's force sufficient to push the droplet in the direction of increased wettability (or higher surface energy). In order for a droplet to move on the wettability gradient the advancing contact angle on the leading edge (more hydrophilic side) of the droplet must be less than the receding contact angle on the trailing edge. If this condition is not maintained, the droplet will remain pinned on the surface. In other words, the gradient surface must have a low hysteresis (difference between advancing and receding contact angle) at all positions along the gradient for droplet motion to occur.

Initial research proved that droplets condensing on a well fabricated gradient surface can attain very high speeds. The fast movement of condensing droplets on a sub-cooled surface exposed to saturated steam was demonstrated by Lehigh University

researchers using a chemically produced surface energy gradient [22]. The movement of these droplets was demonstrated on a 5 cm diameter copper disk with a radial surface energy gradient oriented horizontally. Droplets condensing on the surface moved from the center of the disk to the outer edges by the surface energy gradient. Due to the coalescence of droplets and constant addition of fluid to the surface by condensation, the droplets accelerate to very high speeds. The prevailing theory on the high droplet speeds is related to an effective reduction in the hysteresis as the energy budget of the coalescence process creates a continuous white noise vibration on the droplet surfaces. This white noise vibration causes the droplets to vibrate near their equilibrium droplet shape, rather than remain near the maximum advancing or minimum decreasing contact angle experienced when a single droplet moves along the gradient surface. Droplet speeds of over 30 cm/s have been measured on the horizontal surface. However, the high velocities don't necessarily cause the higher heat transfer coefficients experienced when condensing on wettability gradient. The higher heat transfer coefficients are more likely caused by the reduction in the maximum droplet size. As touched on above, r_{max} should include a term in the numerator accounting for hysteresis of the surface. However, the hysteresis of a surface varies most strongly with surface preparation quality, making the consistent estimation of the hysteresis difficult. Most condensation researchers don't measure or report surface hysteresis. Methods do exist for predicting the changes in hysteresis on a surface for various fluids, with the molecular weight of the fluid being the dominant factor. In general, higher molecular weight fluids have lower hysteresis.

The additional Young's force acting on the droplet (due to the presence of the wettability gradient) causes a reduction in the maximum droplet size, although larger

droplets may be observed in locations where the gradient is not steep. The smaller departing droplet size (r_{max}) causes an increase in the condensation heat transfer coefficient relative to falling droplets. Due to the gravity independence, the heat transfer coefficient values are higher in comparison to traditional dropwise condensation surfaces oriented horizontally, even outperforming filmwise condensation surfaces with the full aid of gravity. No models exist to estimate the dropwise condensation heat transfer coefficient on wettability gradients although data has been reported by several researchers.

A summary of data acquired for steam at 100°C and several inclinations is provided in Figure 4.6. The data is not in complete agreement. This is likely due to some differences between the data sets, such as length of the gradient (a few centimeters), type of surface (silicon, copper), and gradient type (linear, radial) as well as traditional dropwise condensation issues such as non-condensable gas. However, when the data is averaged with respect to heat flux, and plotted along with additional data taken at different inclinations, some general trends exist (Figure 4.7).

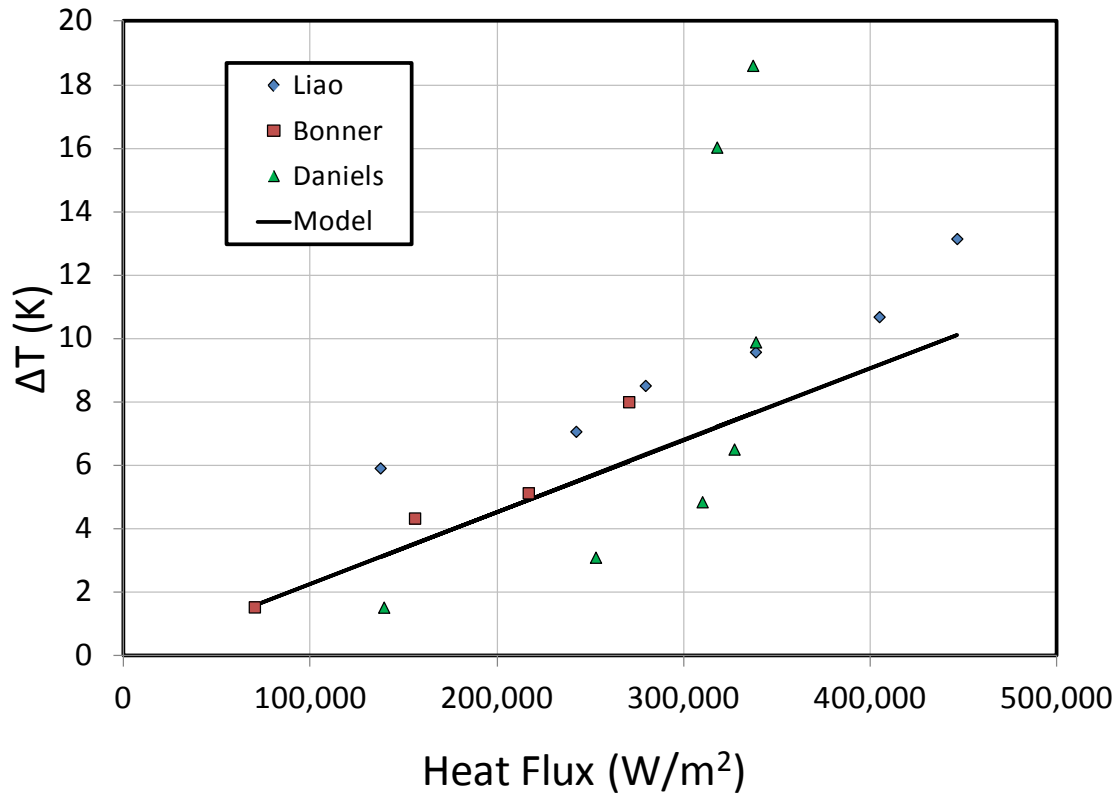


Figure 4.6 Gradient Data Horizontal versus Heat Flux

To model the data plotted in Figure 4.7, two modifications to the Bonner correlation are required, including the effect of the Young's force acting on the maximum departing droplet size and the effect of smaller droplet heights as a consequence of decreased contact angles on the hydrophilic side of the gradient. To account for the additional Young's force acting on the droplets an additional term is added to the denominator of r_{max} , such that the gravitational force and Young's force are additive and independent (Eq. 4.24). The Young's force term represents the force per unit volume acting on the maximum departing droplet. Although it is expected that the term should depend on many variables, such as the hysteresis, gradient length, etc., enough reliable

data are not present to accurately model such effects. However, assuming a constant value for the force per unit volume term seems to work reasonably well. When selecting a value for the force per unit volume term, another consideration was included. Ideally the correlation should predict zero heat transfer as the adverse inclination of the surface approaches 10° as is observed experimentally. Dropwise condensation has only been shown at adverse inclinations exceeding 5° as the Young's force is not able to overcome gravity, resulting in flooding of the surface at larger adverse inclinations. A Young's force per unit volume of $1,630 \text{ N/m}^3$ predicts the required zero heat transfer at 10° adverse surface inclination.

$$\text{Eq. 4.24} \quad r_{max} = \left(\frac{\sigma}{\rho g \sin \phi + F_{WG}} \right)^{1/2}$$

In the special wettability gradient case, the contact angle estimation provided in Eq. 4.21 is generally not valid, since the contact angle varies on the surface. The height of the droplets on the surface decrease as the droplets progress towards the hydrophilic side of the gradient, resulting in a decreased conduction resistance (increased heat transfer). A method for calculating the appropriate average contact angle as an input to the Bonner correlation is possible. In this research, an attempt was made at calculating the average droplet height by integrating over all of the droplet heights present on the surface and dividing by the contact angle span. However, this approach results in data being strongly weighted towards the hydrophilic side of the surface, predicting heat transfer coefficients that are too high when using 100° and 0° as the maximum and minimum contact angles. This is to be somewhat expected, since a transition to filmwise condensation is expected to occur well before 0° . With this in mind, and realization that

most of the data acquired on surface energy gradients is below predictions by the Le Ferve and Rose and Bonner models (for various reasons), it was decided to re-correlate the dropwise condensation Nusselt number and calculate the contact angle using Eq. 4.21. The data plotted in Figure 4.7 was fit using a dropwise condensation Nusselt number of 7. In future efforts the contact angle issue will need to be revisited after more data has been acquired.

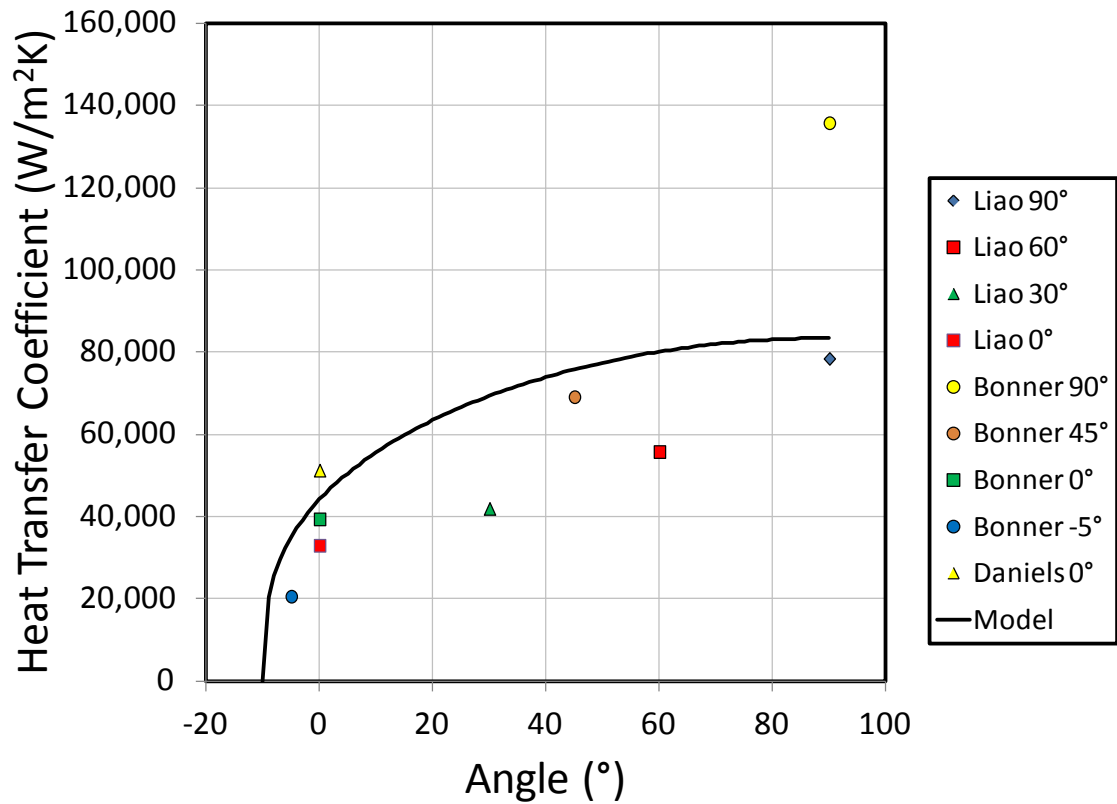


Figure 4.7 Gradient Data Versus Inclination

4.10 Conclusions and Future Work

A new dropwise condensation heat transfer coefficient model was developed that matches empirical data and the observed thermal physics for several fluids and data

acquired on inclined surfaces. The new model was derived using the framework of the Le Fevre and Rose model in addition to the droplet height variation with contact angle. By observing the heat flux versus droplet size predictions made by the Le Fevre and Rose model, prudent simplifications were made to arrive at a manageable expression for the dropwise condensation Nusselt number. Overall, the success of the correlation indicates that the fundamental assumptions of the Le Fevre and Rose model were correct, but contact angle effects are also important. Better agreement with water is found by including a term to account for the loss of thermal driving force due to curvature on small droplets. However, some accuracy is lost with the heat flux dependent term when predicting heat transfer to organic fluids, likely owed to partial filmwise transition of the lower surface tension fluids. Without modification, both the non-heat flux and heat flux dependent models matched the trends of data acquired on inclined surfaces. Finally, a comparison of recent experimental and simulation results show that the effect of monolayer type promoter resistances are small compared to the droplet conduction and interface mass transfer resistances.

Chapter 5

Practical Applications of Dropwise Condensation

As the semi-conductor industry continues to push for increased performance, the amount of power utilized by semi-conductor devices grows. Despite gains in efficiency, a significant amount of the electrical input is converted into waste heat. The waste heat needs to be dissipated to ambient in order to maintain a reliable operation temperature for the device. System integrators face additional challenges that affect thermal management as consumers continue to demand smaller, more portable, and more specialized devices. For these devices to maintain a nominal operating temperature, the thermal management techniques involved must continue to become more efficient and compact.

An important process in the current thermal management architecture involves spreading the heat generated from these small electronics devices over a larger area so the heat can be dissipated to the ambient through traditional air cooled heat sinks. The use of two-phase heat transfer devices such as heat pipes and vapor chambers to help spread heat has become common [40; 41]. As the overall device package shrinks, the area available for heat sinking also decreases, causing larger thermal gradients and heat fluxes through the condensing sections of the two-phase heat transfer devices. A need arises for technologies resulting in a decrease in condenser thermal resistance without additional power consumption or moving parts. The operation of these electronic devices must also be orientation insensitive. Similarly, in micro-gravity applications two-phase cooling solutions must function without the use of gravity.

This section contains some practical research and demonstration efforts to include some of the basic dropwise condensation research described in previous chapters in

practical systems. Section 5.1 describes an effort to promote dropwise condensation in vapor chambers used in many electronics cooling applications. Section 5.2 describes issues regarding the life of the coatings, which is of utmost importance in commercial and military applications.

5.1 Vapor Chambers

An effort was conducted to develop a vapor chamber possessing a dropwise condensation surface [21]. In the development effort, multiple vapor chambers were fabricated and “opened” to assure that the coating was intact after fabrication. Figure 5.1 shows droplets placed on the condenser surface after fabrication.



Figure 5.1 Droplets were placed at multiple locations on the vapor chamber lid to test for hydrophobicity.

The performance improvement attributable to the dropwise condensation coating was then experimentally tested. A vapor chamber prototype was specially modified to acquire accurate heat transfer coefficients in the condenser. This extra effort is required since the ΔT from the wall to fluid space is often very low ($<2^{\circ}\text{C}$) with dropwise condensation.

The condensation lid of the vapor chamber was made thicker than a normal vapor chamber lid to allow for accurate measurement of the heat transfer coefficient on the vapor chamber inner surface. The thicker lid allowed for the drilling of two holes in the condenser surface that were used to extrapolate the surface temperature of the condensation surface and perform conduction calorimetry. Conduction calorimetry was performed by using Fourier's Law to calculate the heat flux at each location (more details on conduction calorimetry were described in Chapters 2 and 3). A diagram showing the location of various thermocouples in the vapor chamber is shown in Figure 5.2. Two (2) holes were drilled at five (5) locations in the lid to extrapolate the surface temperature and determine the local heat fluxes through the lid. The dimensions of the vapor chamber heat input areas were 5.08cm x 5.08cm. The heat input (evaporator) and heat removal (condenser) sections were equally sized in this experiment to exaggerate heat fluxes in the heat removal regions.

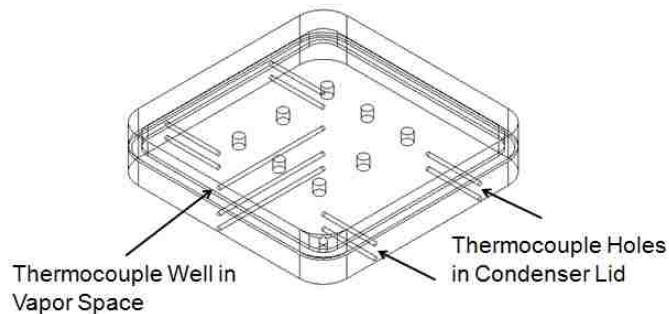


Figure 5.2 A solid model showing the location of thermocouple required to measure the surface temperature and heat flux (through conduction calorimetry) are shown. Also shown is a thermocouple in the fluid space to measure the saturated fluid temperature.

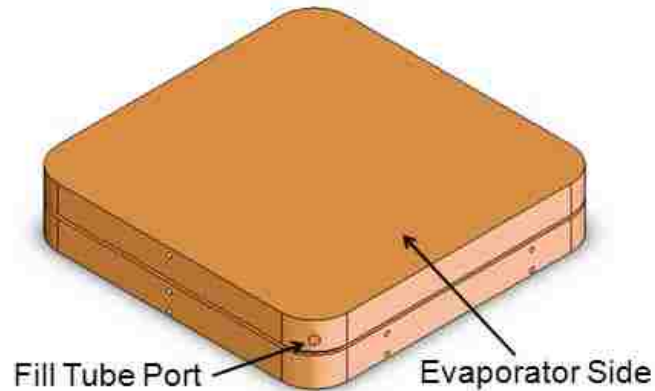


Figure 5.3 A solid model of the tested 5.08cm by 5.08cm vapor chamber is shown.

The vapor chamber was tested in a gravity aided orientation with the condenser surface perpendicular to the ground. A baseline vapor chamber with a filmwise condensation surface was also fabricated and tested. The vapor chambers were tested with the saturated vapor temperature set to 70°C. The average condenser heat fluxes tested ranged from 2W/cm² to 25W/cm². Measured heat transfer coefficients for the filmwise and dropwise condensation surfaces are shown in Figure 5.4. The data shown are the numerical average of the five (5) local heat transfer coefficients measured. The filmwise condensation data are also compared to the Nusselt filmwise condensation model [4] in Figure 5.4.

The dropwise surface resulted in condensation heat transfer coefficients that were ~4 times higher than model predicted filmwise condensation and ~2 times higher than the tested filmwise surface. The disagreement between the filmwise condensation model and the filmwise condensation test data is likely due to surface conditions. Organic contamination on the filmwise surface is likely to result in a transitional

dropwise/filmwise surface that is consistent with the test data. However, it is expected that the transitional (part dropwise/ part filmwise) surface that was likely present would eventually transition to completely filmwise and result in the predicted filmwise condensation performance. In another study conducted on copper surfaces where visualization of the surface was possible, the filmwise data matched very well with the model [11]. In that work, the test setup allowed for stringent cleaning of the surface and more control over the copper oxide growth conditions.

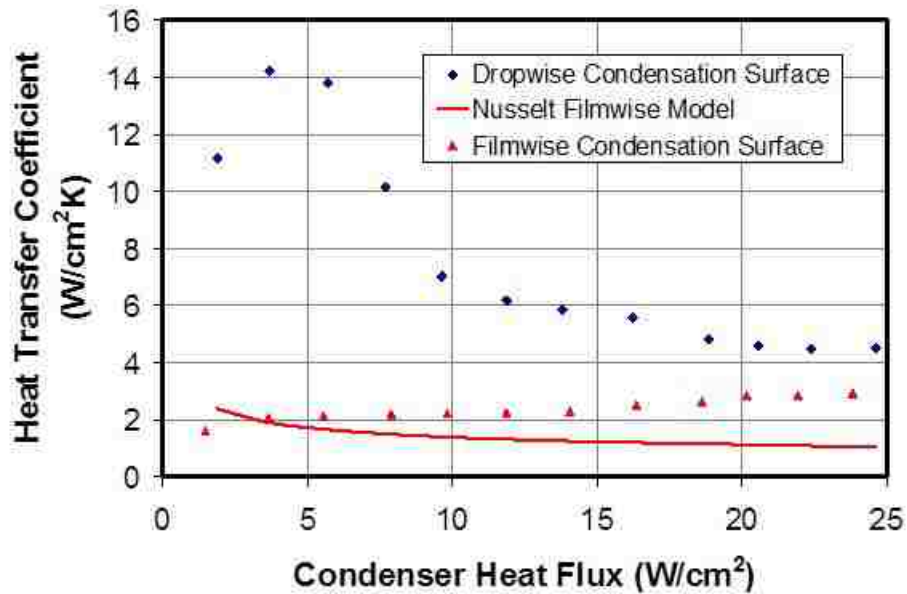


Figure 5.4 Gravity aided condensation heat transfer coefficient data for a vapor chamber with a dropwise condensation surface is shown. Filmwise data are also compared to predictions from the Nusselt model for filmwise condensation.

The dropwise condensation performance was also not as beneficial as expected. In the same study referenced above, an 8-10 times improvement in heat transfer coefficient was measured with dropwise condensation over filmwise condensation. It is

suspected that the degradation of the surface around the perimeter may have contributed to the measured performance degradation. This effect should be minimized when a larger vapor chamber is fabricated, and the perimeter related defects aren't as dominant.

5.2 Life Testing and Reliability

A life test was performed to determine the durability of thiol based SAM on coinage metal (copper and gold plated copper) surfaces [19]. The life test was performed under vacuum at a saturation temperature of 60°C. The saturation temperature was chosen to mimic the vapor temperature of heat pipe systems designed for electronics cooling. The temperature is also associated with operation at the higher end of environmental conditions expected for commercial applications. This life test is not considered to be directly applicable to industrial operations, such as distillation, where a continuous supply of fresh fluid (with fresh contaminants) occurs and operation at higher temperatures is typical.

The copper and gold plated copper surfaces life tested in this study were prepared with a heptafluoro-1-decanethiol SAM. The surfaces were first polished until an mirror surface finish was attained. The surfaces were then ultrasonically cleaned with methanol. The native copper oxides on the surface were removed with nitric acid. The surface was then exposed to an oxidizing solution to create hydroxyl groups on the copper surfaces. The SAM was then created by placing the surface in a dilute solution of IPA and heptafluoro-1-decanethiol overnight. The surface was also rinsed with IPA and blown dry with nitrogen after every step of the preparation. Immediately after preparation the contact angle was visually inspected at various locations on the surface to be ~110°.

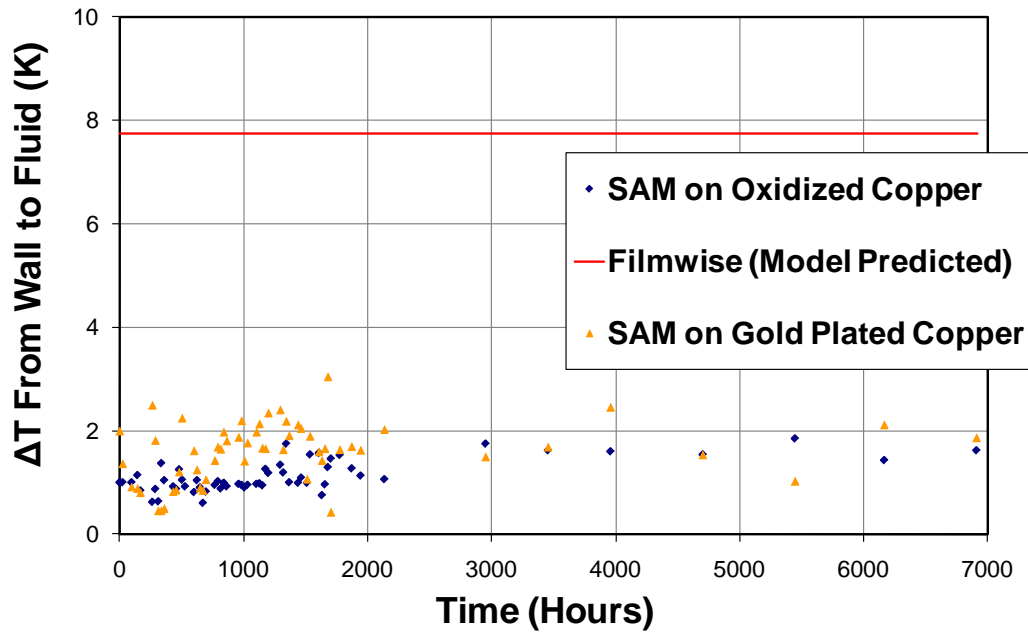


Figure 5.5 Life test data for copper and gold surfaces prepared with SAM's are shown.

The life test data reported here are a numerical average of the extrapolated surface temperatures. Surface temperature was chosen as the reported variable because significant scatter results since the measured ΔT is very small at the low heat fluxes encountered with life test. The life test results are plotted in Figure 5.5. Both of the surfaces have been viable for over 9 months and the test is continuing. The longer duration between data after 2000 hours coincides with the funded project end date. Visual inspection of the surface shows both surfaces are still exhibiting full dropwise condensation. It should be noted that the gold surface appears to be producing better droplets than the copper surface (less pinning, smaller sizes), but this is not evident in the

heat transfer measurements. The gold plated surfaces are expected to outperform the copper surface, as gold forms stronger bonds to the sulfur reactive group of the SAM.

5.3 Conclusions and Future Work

In summary, self-assembled monolayer coated condensation surface were tested in vapor chamber heat transfer devices suitable for commercial electronics cooling. A well instrumented vapor chamber was fabricated and tested to take accurate condensation heat transfer coefficient measurements. Filmwise and dropwise condensation vapor chambers were experimentally tested. The dropwise condensation mechanism demonstrated superior performance over conventional vapor chambers with a 4 fold improvement in heat transfer coefficient performance over predicted filmwise condensation performance. Dropwise condensation performance is expected to be even higher if the quality of the self-assembled monolayer coating can be maintained on the perimeter of the vapor chamber during sealing. Self-assembled monolayer coatings were also investigated for reliability. Over 2,000 hours of successful life testing with water was demonstrated at suitable (70°C) electronics cooling temperatures.

PART II

MICRO- AND NANO-SCALE HEAT TRANSFER TOPICS

Chapter 6

Micro-channel Corrosion Prevention

6.1 Overview

Many high heat flux electronics applications have surpassed the limits of air cooling and are moving towards liquid cooling as a method to remove waste heat directly from electronics packages. In applications such as power electronics, high liquid velocities along with highly corrosive coolants (DI water in particular) limit the reliability and performance capability of many liquid cooling solutions. Engineering solutions include the use of stainless steel in place of better performing copper or aluminum materials and the use of costly nickel and gold platings where the performance of copper is required. The problem is particularly difficult with copper micro-channel coolers (MCCs), as conventional plating techniques are not capable of creating conformal coatings in the micro-channels. In this effort, preliminary results on the passivation capability of nano-scale alumina coatings deposited by atomic layer deposition (ALD) were attained [42]. ALD coatings are deposited in the vapor phase, one atomic layer at a time, resulting in unmatched conformality and coating thickness uniformity on the micro-channel geometries. Experimental results for thermal cycling, erosion and corrosion passivation performance with salt water are presented for a baseline (copper), gold plated copper, and ALD coated copper micro-channel coolers. In all cases the ALD coated samples demonstrated superior passivation properties.

6.2 Background Reliability Issues in Micro-channel Coolers

Currently, the most effective method used to remove large amounts of heat is pumped single-phase coolant flowing through copper micro-channel coolers (MCCs).

MCCs are fabricated using a combination of micro-machining, lithography, etching, and diffusion bonding [43]. Most commercially available MCCs are made with many thin sheets of photo-etched copper that are diffusion bonded together. Copper is used because of its excellent thermal and electrical conductivity (in applications where the MCC serves as both a cooler and as an electrical bus bar). The MCC design increases surface area and improves convection (due to the small channel diameters) which minimizes the overall thermal resistance of the cooling solution. To minimize conduction resistance, cooling fluids often pass very close to the heat source. De-ionized (DI-H₂O) water is often used as the cooling fluid because of its excellent thermo-physical properties. Although this design is thermally advantageous, the use of copper allows the electrical path to come into direct contact with the water cooling fluid (this is true of cases where the copper is used as an electrical bus bar or is simply not completely electrically isolated from electrical live electronics devices). When an electric potential is applied to the copper, a very rapid reaction occurs between the copper and water that results in well-documented failure mechanisms including corrosion and erosion [44]. Even without the extreme case of applied electrical potential, electric potential differences stemming from having dissimilar materials (galvanic corrosion) or simply high purity DI water can also create highly corrosive conditions [45].

One solution to this problem is to electrically isolate the device from the cooling fluid by using ceramic materials. Ceramics are very inert and their high dielectric constant prevents electro-chemical corrosion with DI-H₂O. Ceramics are also hard, which improves erosion resistance. To maintain structural stability, the ceramic pieces must be rather thick. To maintain respectable heat transfer, only ceramics with high thermal

conductivity may be used. Such ceramics include beryllium oxide, aluminum nitride, and thick films of chemically deposited diamond [46]. Although the thermal conductivity of these materials is decent, they are at best less than half that of copper. Another disadvantage of ceramic MCCs is cost. The use of exotic-thermally conductive materials is a driving factor, as well as the specialty fabrication processes required to manufacture precision structures from ceramics.

A typical, and more cost effective approach used to prevent corrosion in copper MCCs uses very thin barrier coatings consisting of nickel and gold. Corrosion prevention is primarily controlled using the gold thin film. To hinder copper diffusion into the gold and improve wear resistance, an intermediate layer of nickel is used [47]. Although the nickel does impede copper diffusion, it does not completely prevent it [48]. Studies show that even at low temperatures, copper may diffuse across the nickel barrier [49]. Additionally, micro-channels with high aspect ratios tend to cause non-uniform electric fields during the metal plating process, and as a result, pinholes form in the gold/nickel film exposing bare copper [50].

Currently, failure of the MCC resulting from corrosion is a leading cause of power electronic systems failures. A passivation coating that significantly improves MCC reliability would in turn increase the reliability of high power electronic systems.

6.3 Corrosion and Erosion Mechanisms

When an electric potential is applied to a copper MCC, a very rapid electrochemical reaction may occur between the copper MCC and coolant fluid. For this reason, de-ionized water (DI-H₂O) is used as a cooling fluid. Not only does DI-H₂O have excellent thermo-physical properties, it also has a high electrical resistivity. DI-H₂O with

a resistivity ranging from 0.1-0.5 MΩ/cm provides optimum corrosion prevention. A lower resistivity allows current flow resulting in increased electrochemical corrosion. As the resistivity increases, the pH decreases, and corrosion caused by hydrogen ions becomes dominant. DI-H₂O with the optimum resistivity reduces the flow of electrons, and consequently the electrochemical reaction is only driven by leakage current [44]. This corrosion process is further hindered by the use of nickel/gold (Ni/Au) thin films. However, pinholes in the plating significantly reduce MCC reliability by providing corrosion initiation sites.

Erosion on copper MCCs is also a significant problem [46]. High velocity water flow may disrupt adherence between the Ni/Au thin films and the copper MCC. In addition, the removal of surface films by erosion may accelerate corrosion. This phenomenon is known as erosion-corrosion. Defects in the coating surface allow turbulent eddies to form (Figure 6.1A) which results in undercutting of the protective films (Figure 6.1B-D). Debris that is spalled off and carried away in the high velocity fluid may impinge the coating, exacerbating the erosion process. Coatings that provide the best erosion protection are hard, dense, adherent, and continuous [51].

A conformal coating that is electrically insulating, hard, and easily deposited will economically reduce/eliminate the failure mechanisms facing Ni/Au plated copper MCCs. A thin electrically insulating barrier placed between the copper MCC and the DI-H₂O water cooling fluid will prevent charge migration and corrosion. A hard barrier coating will prevent erosion. The coating must also be easily deposited, highly uniform, and pinhole free.

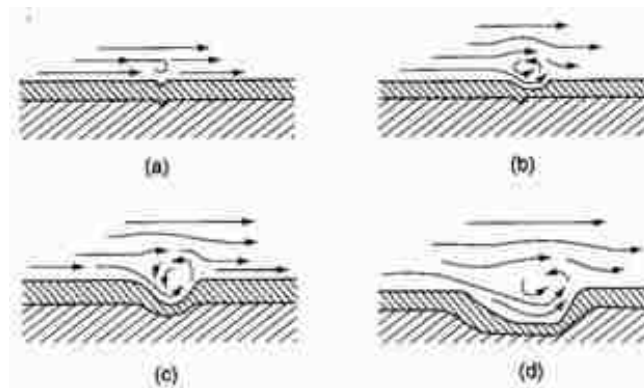


Figure 6.1 Schematic of turbulent eddy mechanism for downstream undercutting of erosion-corrosion pits [51]. Defects in the coating surface allow turbulent eddies to form (a), which results in undercutting of the protective films (B-D).

6.4 Atomic Layer Deposition

Atomic layer deposition (ALD) is a well-developed deposition process capable of depositing uniform ceramic thin films, including alumina, zirconia, hafnium oxide, titanium nitride and aluminum nitride. This deposition process is a result of a chemical reaction between two precursor chemicals and the substrate material. The precursor chemicals are in the gaseous phase, allowing uniform coatings to be deposited on surfaces with high aspect ratio features, such as copper MCCs.

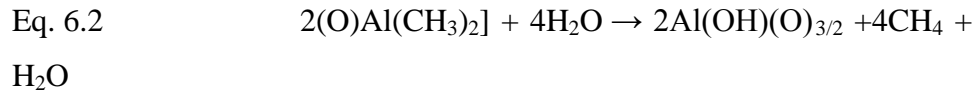
ALD is commonly used to deposit oxides and nitrides. This is done by introducing the molecular precursors into the ALD reactor separately. Typically, the first precursor chemical is a volatile molecule consisting of a metal element attached to a ligand. This molecule chemically bonds to the active sites on the substrate surface. This reaction is complete when the metal-ligand gas has reacted with all of the active sites on the surface. To remove any by-product gases, this step is followed by an inert gas purge.

After the gas purge, a second precursor chemical is introduced. This reaction is also self-limiting, and completes once it has reacted with all of the metal-ligand molecules. At the end of this reaction a single monolayer film is deposited and the surface chemistry is restored to its initial state. This allows the two-step reaction to be repeated multiple times, each time creating only a single layer. Since each cycle results in a single layer, the thickness of coatings created with ALD can be controlled very precisely by controlling the number of cycles.

An ALD coating process of particular interest for Ni/Au MCCs is alumina (Al_2O_3), shown in Figure 6.2. To begin ALD of Al_2O_3 , the surface must first be functionalized with hydroxyl (OH) groups (Figure 6.2A). The OH groups provide active sites for the metal-ligand molecule tri-methyl-aluminum ($\text{Al}(\text{CH}_3)_3$) to bond, resulting in the following reaction (Eq. 6.1, Figure 6.2B):



At the end of this reaction, the methane (CH_4) is removed via inert gas purge (Fig. 2c), and the remaining $\text{Al}(\text{CH}_3)_2$ provides the necessary surface chemistry for the next reaction. Water vapor (H_2O) is flowed into the ALD chamber creating the following reaction (Eq. 6.2, Figure 6.2D):



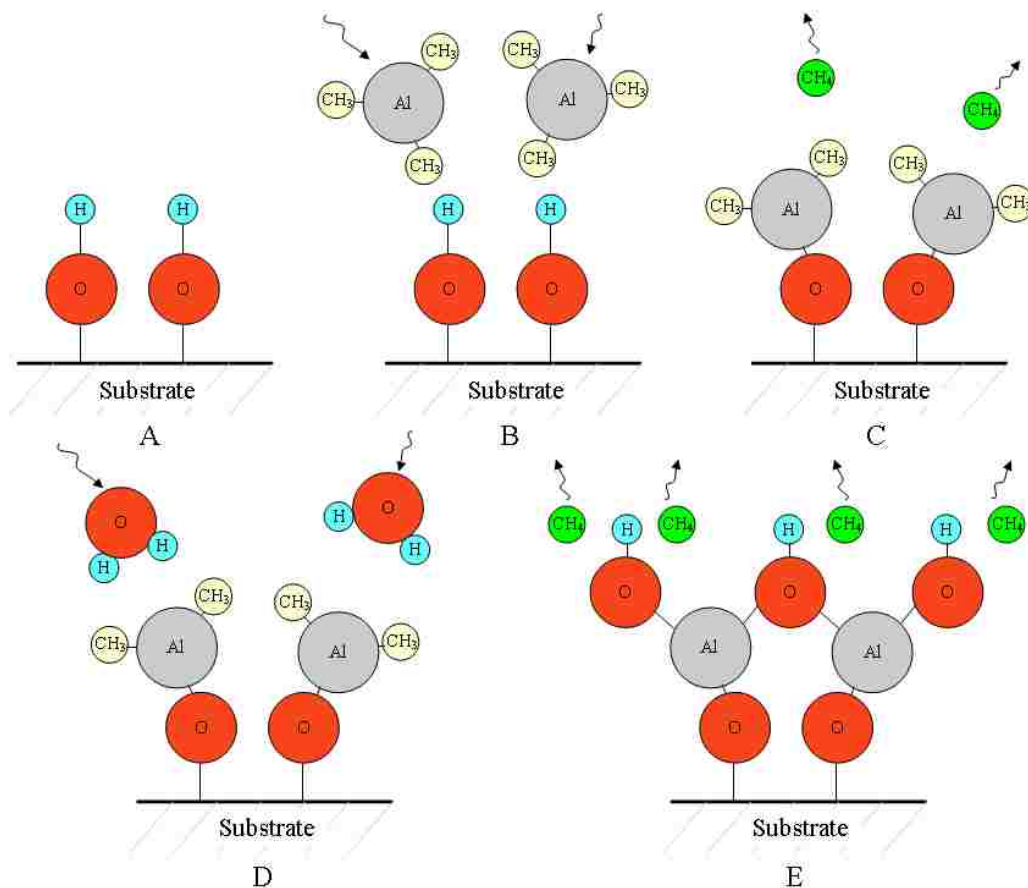


Figure 6.2 Atomic Layer Deposition Process of Al_2O_3 . For Al_2O_3 -ALD to begin, the substrate must be prepared with OH groups (A). The first reaction in Al_2O_3 -ALD uses $\text{Al}(\text{CH}_3)_3$ (B), which reacts with the hydroxyl groups and releases CH_4 (C). The second reaction in Al_2O_3 -ALD uses water vapor (D). The water reacts with the remaining methyl groups, releasing more methane, and restores the surface chemistry to the initial OH condition (E).

The H_2O in this reaction reacts with the $-\text{CH}_3$ sites that remain from the initial precursor. The reaction self-saturates once all the $-\text{CH}_3$ sites have reacted. At the end of this reaction, a single ALD cycle is complete, and the density of surface hydroxyl group is restored to the original state (Figure 6.2E) [52].

ALD is identified as a coating process capable of producing highly uniform thin films. Since the deposition process uses gaseous precursor chemicals, ALD has the ability to deposit material on substrates with high surface aspect ratio features, like copper MCCs. The self-limiting nature of ALD allows coatings of precise thickness to be deposited. ALD works especially well at depositing ceramics, like Al_2O_3 . Since ceramics are naturally electrically insulating and hard, they will provide excellent corrosion and erosion protection in Ni/Au plated copper MCCs.

6.5 Self-Assembled Monolayers

The surface chemistry of the substrate plays an important role in coating adhesion. A specific chemistry is required for bonding during ALD deposition where the surface must be hydrophilic to ensure the first step in the cyclic ALD process occurs. Any imperfections on the substrate surface will also limit deposition, and result in pinholes. Self-assembled monolayers (SAMs) were chosen as a surface treatment method that is compatible with ALD, is capable of providing hydrophilic, defect free surfaces for initial deposition.

The SAM technique involves chemically reacting molecules with a short polymer chain to a surface, as illustrated in Figure 1.1. The chemicals used in these types of surface preparations are typically polymer chains approximately 8-20 molecules long. On one side of the polymer chain is a reactive functional group, capable of forming a chemical bond with a surface. In this effort a thiol (-SH) functional group capable of creating a chemical bond with gold or copper was used. It should be pointed out that the “coating” used in this process is more than just paint, as the chemical bond between the molecule and the metal surface is of a permanent nature. The other end of the polymer

chain is a hydroxyl (-OH) surface group that will form a chemical bond with the precursors used in the ALD process. Although other functional groups are possible, the hydroxyl group will form the strongest bond with the ALD treatment. The self-assembly process is naturally self-extinguishing after one layer of molecules assembles on the surface, since only one of the functional groups on the polymer chains reacts with the gold or copper surface while the other functional group is non-reactive. Furthermore, the reactive end group does not react with the surface functional group.

In the ALD process the metal surface needs to be kept very clean so that the chemical bond to the surface is strong. Chemical cleaning methods were used, since mechanical cleaning methods will be difficult on the micro-channel surfaces. The self-assembly process occurs spontaneously on the surface when a solution of the molecules in either a liquid or vapor form comes into contact with the surface. Typical thiol chemistry involves immersing a cleaned surface in an alcohol/SAM reagent mixture to allow the self-assembly process to occur. In this case, a thiol with a relatively long carbon chain was chosen because longer chained SAM molecules tend to pack and organize better than shorter chain SAM molecules. Further, the SAM was terminated with a hydroxyl group to make the surface hydrophilic.

In addition to strong bonding, the SAM covers surface defects on the metal surface, which will insure that a pinhole free ceramic coating is deposited. The elastic properties of the SAM also make the ceramic coating more strain tolerant, reducing stresses caused by mismatch in thermal expansion coefficient between the ceramic coating and metal MCC. Increased compliance also aids erosion protection.

6.6 Coating Identification

Figure 6.3 shows an illustration of the complete coating, including the alumina, SAM, and metal plating layers on the copper MCC surface. It should be noted that the gold layer is not required as the SAM can be deposited directly on copper. However, the SAMs generally bond better to gold than copper and the Ni/Au layer certainly doesn't hamper the passivation protection of the coating.

6.7 Erosion, Corrosion, Thermal Cycling Experimental Results

Three micro-channel samples were fabricated for each of the passivation tests, including a baseline (all copper), gold plated and an alumina (by ALD) coated sample. The alumina sample was first coated with gold, and a thiol based SAM before 10-100 nanometers of alumina was deposited by ALD. The thickness of the coating results in negligible thermal resistance. Several test apparatus were fabricated for the different passivation processes. In all, 3 different passivation tests were performed, including erosion, corrosion and thermal cycling.

A multipurpose test set capable of high liquid velocities and accelerated electrochemical corrosion was developed to test for erosion and corrosion (Figure 6.4). The test article design includes a lid with a step to eliminate flow area above the fins and a means for applying electrical current normal to the surface (Figure 6.5). The resulting average fluid velocity through the channels was 1.9 m/s.

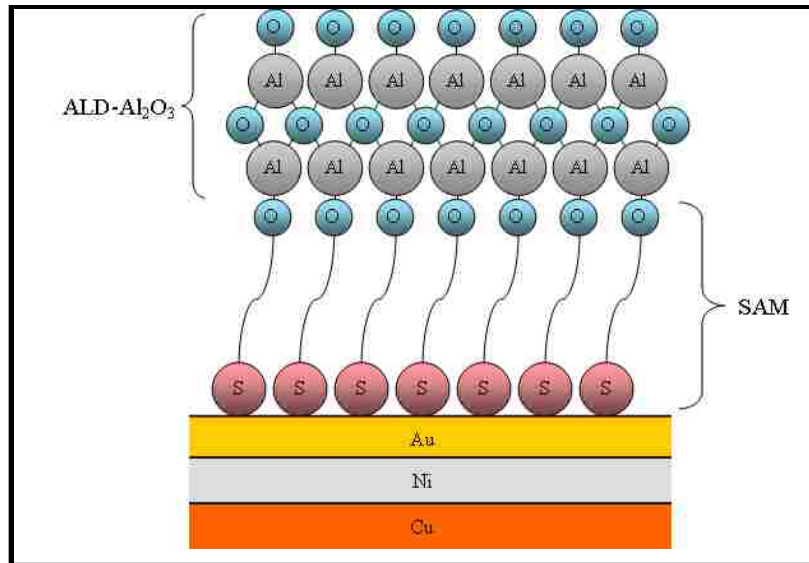


Figure 6.3 Illustration of coating: alumina coating deposited on a self-assembled monolayer on a gold plated copper surface.

Currently, Ni/Au thin films are susceptible to erosion, exposing bare copper to the DI-H₂O. Our goal was to show the ceramic coating would be impervious to these effects. Visual inspection was used after high velocity testing, but in all cases including bare copper, there were no detectable traces of erosion. In future work, higher velocities at longer duration will be used.

Several thermal cycling tests were performed to demonstrate the survivability of the alumina coating under thermal stress. The most impressive test involved heating a copper and an alumina coated micro-channel side by side on a hot plate. At temperatures exceeding 300°C, the alumina coated sample showed no oxidation resistance, which would be expected if thermal expansion were to cause delamination of the coating (Figure 6.6). The baseline copper sample showed gross oxidation (a form of corrosion)

as expected. Other tests were also run where the samples were cycled between room temperature and 100°C in water several dozen times without degradation.



Figure 6.4 Illustration corrosion and erosion test apparatus.

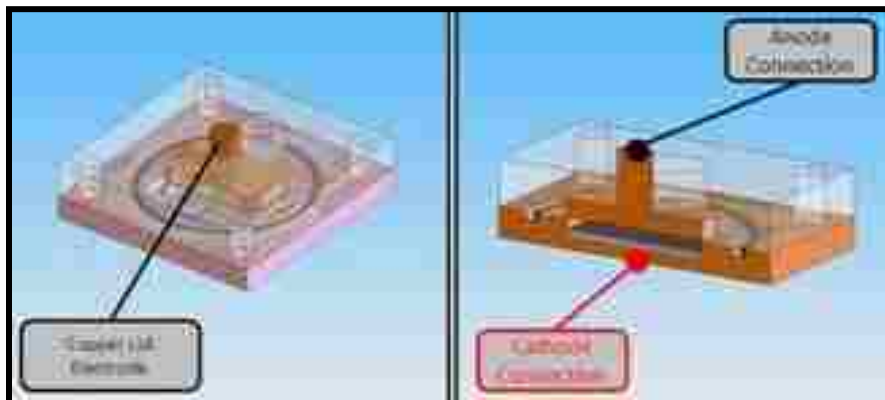


Figure 6.5 Illustration of corrosion test article.

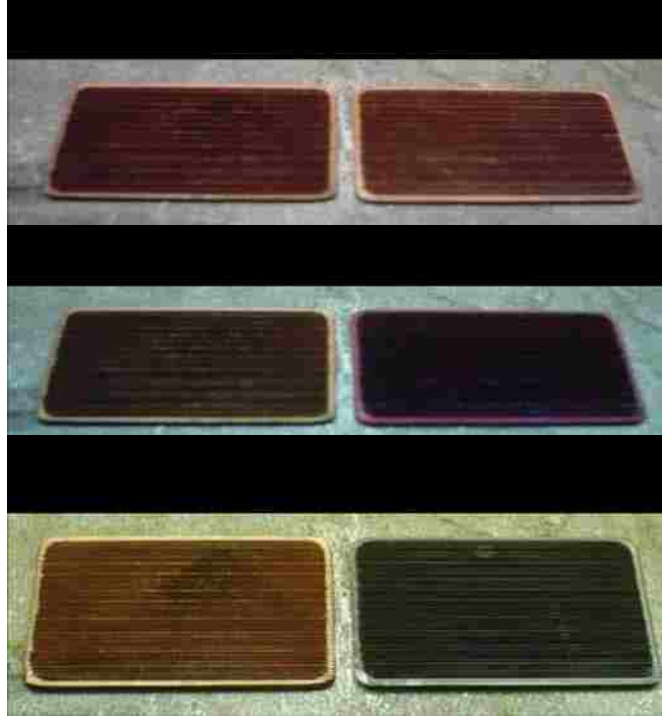


Figure 6.6 Thermal cycling results for copper and alumina coated samples.

An accelerated corrosion test was also performed where a voltage was applied across the surface through an electrically conductive salt water solution. As expected, the copper (Figure 6.7) and gold plated (Figure 6.8) samples showed significant, visible corrosion. The alumina (on gold) coated sample showed negligible corrosion (Figure 6.9). Future work involves using electrochemical analysis to quantify corrosion rates.

6.8 Conclusions and Future Work

Thin film (<100 nanometer) alumina coatings deposited by ALD are promising candidates for passivation coatings in MCCs and other liquid cold plates. In experimental thermal cycling, erosion, and corrosion tests, ceramic ALD coatings outperformed state of the art metallic coatings. Future work involves long duration life

testing, more quantitative electrochemical analysis, and exploration of other ALD deposited ceramics, such as hafnia.

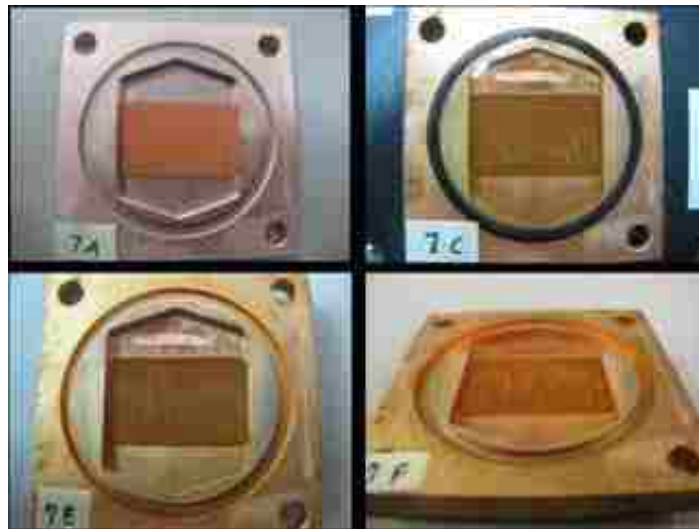


Figure 6.7 Results for corrosion testing of baseline copper samples are shown. The top left picture is before testing, the others are post testing.



Figure 6.8 Results for corrosion testing of gold plated samples are shown. The top left picture is before testing, the others are post testing.



Figure 6.9 Results for corrosion testing of alumin (by ALD) on gold plated samples are shown. The top left picture is before testing, the others are post testing.

Chapter 7

Die Level Thermal Storage

The work presented in this chapter is the result of a collaboration between a number of team members from Advanced Cooling Technologies, Inc. (Tapan Desai, Angie Fan, Xudong Tan), Massachusetts Institute of Technology (Feng Gao, Daniel Piedra, Tomas Palacios), and University of Michigan (Seungha Shin, Massoud Kaviany). The team collaborated through a National Reconnaissance Office (NRO) sponsored research project, where Mr. Bonner served as the Principal Investigator. Mr. Bonner also lead the proposal effort, and is the primary inventor on a patent application related to the work investigated in the NRO research project. The work described in this chapter is a summary of the research orientated tasks directly investigated by Mr. Bonner, with brief summaries of the work performed by other investigators where the collaboration required overlapping tasks. The work resulted in the publishing of several papers, most of which are summarized below. The work presented in this chapter is primarily derived from the paper lead by Mr. Bonner, listed first.

- Bonner, R., et al., March 2011, "Die Level Thermal Storage for Improved Cooling of Pulsed Devices," Semitherm, Santa Clara, Ca.
- Desai, T., Piedra, D., Bonner, R., et al., "Novel Junction Level Cooling in Pulsed GaN Devices," ITherm, San Diego, CA, May 30, 2012
- Piedra, D., Desai, T., Bonner, R., et al., "Integration of a Phase Change Material for Junction-Level Cooling in GaN Devices," Semi-therm, San Jose, CA, March 2012
- Tang, X., Bonner, R., et al., "A 2-D Numerical Study of Micro-scale Phase Change Material Thermal Storage for GaN Transistor Thermal Management," Semi-therm, San Jose, CA, March 2011
- Shin, S., Kaviany, M., Desai, T., Bonner, R., "Roles of Atomic Restructuring in Interfacial Phonon Transport," Physical Review B, 82, 081302 (2010)

7.1 Overview

In many communications applications semiconductor devices operate in a pulsed mode, where rapid temperature transients are continuously experienced within the die. A novel junction-level cooling technology was investigated, where a metallic phase change material (PCM) was embedded in close proximity to the active transistor channels without interfering with the device's electrical response [53; 54; 55; 56]. Multi-scale simulations were performed to determine the thermal performance improvement and electrical performance impact under pulsed operating conditions. The modeling effort was focused on Gallium Nitride (GaN) on Silicon (Si) chips with Indium (In) as the PCM. To accurately capture the micro-scale transient melting process, a hierarchical multi-scale model was developed that includes linking of atomistic-level molecular dynamics simulations and macro-scale finite element analysis simulations. Macro-scale physics, including the melting process, were captured with a transient two-dimensional finite element analysis (FEA) model. The FEA model also includes interfacial and contact resistances between the semiconductor materials and PCM. Non-equilibrium Molecular Dynamic (MD) simulations were performed to estimate the value of the interfacial resistances between the Si substrate and the In PCM, which included a new interatomic potential between In and Si that was developed from experimental scattering results available in the literature. The thermal modeling results indicate 26% more heat can be dissipated through the PCM enhanced transistor while maintain a safe operating temperature. A separate electrical modeling effort showed that the metallic PCM layer did not create appreciable parasitic capacitances as long as the PCM was farther than $1\mu\text{m}$ from the active channel. The lower, more constant temperatures achieved by this

technology can help improve the reliability and performance of future communication devices.

7.2 Introduction

In the last few years, AlGaIn/GaN high electron mobility transistors (HEMTs) have become the preferred option for solid state amplifiers in the 1-40 GHz frequency range [57]. With an output power density of more than 40 W/mm² (defined as power per unit length of gate) at 4 GHz, these devices offer 10 times higher power density than Si-based electronics, higher efficiency levels, lower cooling requirements and easier impedance matching [58]. The extremely high power densities available in nitride devices create new challenges for heat management and extraction in these devices. Most GaN transistors are grown on Silicon Carbide (SiC) substrates, which have a thermal conductivity 3 times higher than Si. However, this approach is not ideal. SiC substrates are only available on 4" diameters, and are at least 100 times more expensive than Si. Although SiC dissipates heat more effectively than Si, the heat dissipation still limits device performance. In spite of the unprecedented power densities demonstrated in these devices, commercial GaN devices typically operate at much lower power densities (4-6 W/mm²) due to the great difficulty in dissipating the generated heat [59]. The device junction temperature needs to be kept below 175°C to minimize degradation in the transport properties of the semiconductor and, more importantly, to assure good reliability [60]. Even when operating at the relatively low power densities of 4 W/mm², large heat sinks are required that significantly reduce the system scalability. New approaches to efficiently extract the heat at the device level will significantly improve the performance of nitride transistors.

7.3 Background

A micro-scale thermal storage approach was proposed that takes advantage of the transient behavior in communication devices where heat generating pulses on the order of a few milliseconds or even microseconds are typical. The duty cycle is typically between 2% and 10%. The idea is to increase the effective heat capacity of the material near the active channels of the GaN devices by embedding a PCM (material that changes phase between liquid and solid at a given temperature) in close proximity to the active channels. During the heat generating pulses of each duty cycle, the large amount of heat generated in the GaN devices is temporarily stored in the heat of fusion of the PCM as the solid material is melted. During the inactive times, heat is dissipated as the phase change material re-solidifies.

During operation, GaN device temperatures can oscillate between 150°C and 80°C during the rapid transients. The constant thermal cycling and high maximum junction temperatures cause cyclical thermal stresses that lead to reduced reliability. By using PCMs with significantly lower melting points than 150°C, the peak junction temperature can be reduced and the transient temperature profile stabilized. By reducing the peak junction temperature of the GaN devices and maintaining a more constant temperature, reliability will be greatly improved. Solders with low melting points were selected as the phase change material. Solders are preferred over paraffin wax based PCMs due to their higher thermal conductivity. In₅₂Sn₄₈ (52% Indium, 48% Tin) is the eutectic solder that was targeted in this study due to its advantageous melting point of 118°C. Initial calculations verified the feasibility of the proposed concept. For a GaN device dissipating 100 W/cm² during peak power over a 10 ms pulse, a layer of

approximately 32 μm of $\text{In}_{52}\text{Sn}_{48}$ solder would be required to absorb the heat through heat of fusion. This is very reasonable based on current GaN on Si designs. In this effort, the micro-scale PCM mechanism was modeled to determine the benefits and feasibility of using PCM to minimize peak junction temperatures and maintain temperature stability. Due to the small size of the required PCM components and fast transient nature of the process, macro-scale/finite element analysis and atomic-scale/molecular dynamics analysis were required.

Figure 7.1 shows the transistor modeled in this study. The transistor consists of an 8 μm wide periodic unit cell with two sources, two gates, and one drain. Two localized heat sources (with equal heat fluxes, although typically the heat generation is biased towards the drain) on the GaN surface represent the high heat fluxes generated near the gates. A full scale device consists of many identical unit cells. The whole device is divided into three layers: a 1 μm GaN layer, a silicon 4 μm layer, and 10 μm substrate. The grooved structure shown holding the PCM is 2 μm in thickness and 6 μm in width, although these dimensions were varied throughout the modeling effort. $\text{In}_{52}\text{Sn}_{48}$ was chosen for study as the PCM material, whose heat of fusion is 28.58 kJ/kg. Before the Macroscale Finite Element Analysis (FEA) model could be implemented, the interfacial resistances between the silicon and PCM and between the GaN and Si needed to be estimated. The thermal resistance between GaN and Si was estimated using Diffuse Mismatch Theory [61]. The thermal resistance between Si and the PCM was computed using molecular dynamics as detailed in the Atomistic Scale Modeling section.

Locating a metallic PCM near the junction region might degrade the electrical performance of the device. Analysis was completed using Flex PDE to determine the

parasitic capacitance of the metallic PCM as a function of the PCM layer proximity to the junction. Overall, the PCM is able to be located close enough to be thermally effective without degrading performance, as detailed in the Parasitic Capacitance Modeling section.

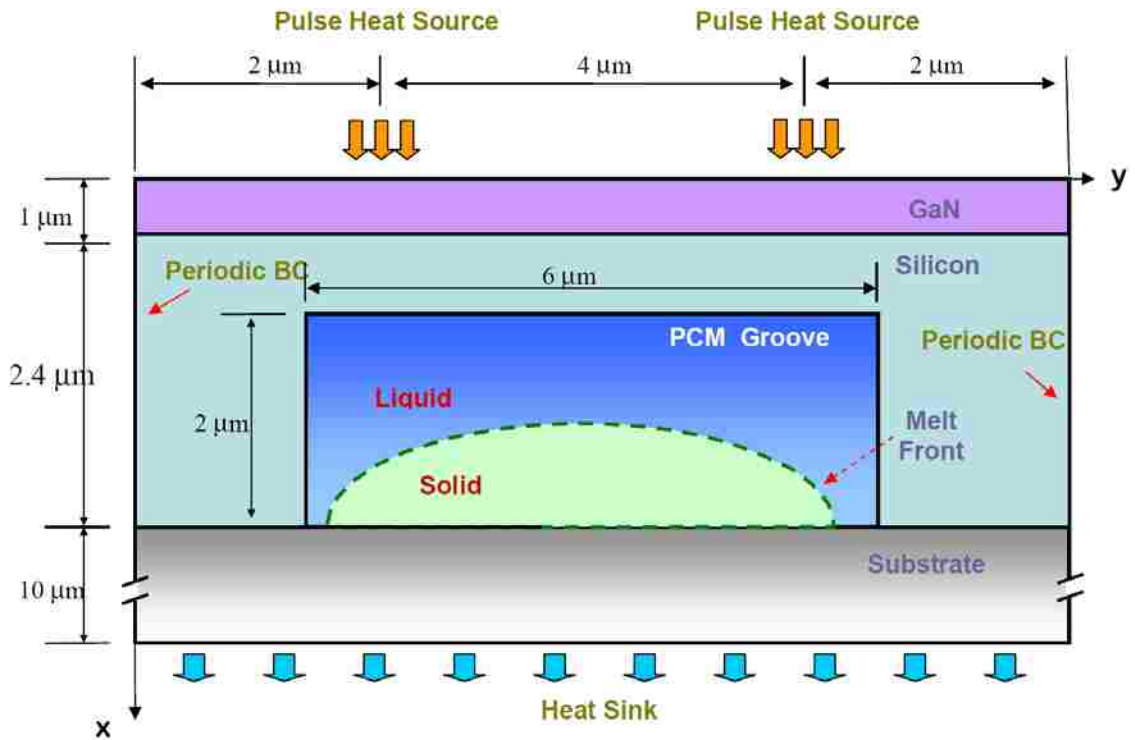


Figure 7.1 Thermal model of a GaN Transistor Unit Cell with a PCM groove structure.

7.4 Macroscale Finite-Element Analysis Modeling

The modeling domain for the Macroscopic FEA model was that of Figure 7.1. A cyclic heat generation boundary condition was applied on the hot spot of the GaN surface as shown in Figure 7.2. In our analysis, each duty cycle lasted 100 μs . Each cycle consisted of 2 μs of heating time and 98 μs of time in which no heat was generated. A constant heat flux of $5 \times 10^5 \text{ W/cm}^2$ was applied during the heat generation portion of the

duty cycle. The heat was generated across the two $0.1 \mu\text{m}$ length junction regions to simulate heating in the gate regions. Periodic boundary conditions were applied on the left and right sides of the calculation domain. At the bottom of the unit cell, a convective boundary condition was applied with a fluid temperature of 25°C to approximate the thermal resistance of a heat sink. More details on the numerical techniques used in this analysis can be found in a related work [56].

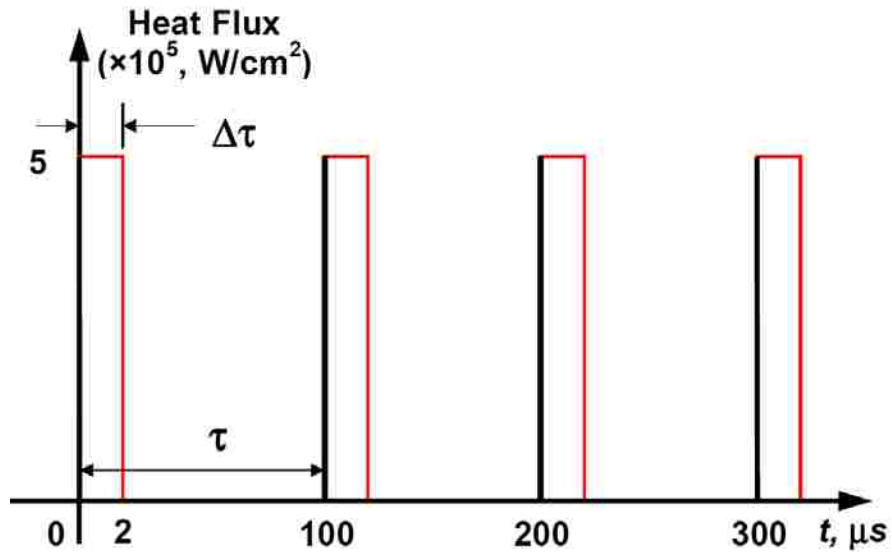


Figure 7.2 Transient heat flux boundary condition.

The transient thermal operation of the device from a cold start to pseudo-steady state is shown in Figure 7.3. A description of a thermal operation throughout a complete cycle at pseudo-steady state is described here. At the beginning of each duty cycle, GaN, Si and PCM are near thermal equilibrium at 97°C . The PCM is all in the solid phase. As heat is applied to the GaN surface, hot spots can be observed, with a temperature about 7°C higher than the rest of the GaN layer due to conduction gradients. The temperature distribution along the GaN-to-Si interface is quite uniform, indicating that heat spreading

across the GaN layer is adequate. The temperature difference across the GaN-to-Si interface is not significant due to its relatively low interfacial thermal resistance. A 3°C to 5°C temperature jump exists across the Si-to-PCM interface. The device temperature keeps climbing and at about $t = 0.8 \mu\text{s}$ (with $t = 0$ representing the start of one of the pseudo-steady pulses) or about halfway through the heat generating pulse, the corners of PCM in contact with Si reach the melting point, 118°C for $\text{In}_{52}\text{Sn}_{48}$. The melt front extends to the entire Si-to-PCM interface to form an arc shaped two-phase interface. As more heat is applied, the melt front propagates towards the heat sink region. During this process, the solid PCM remains at 118°C as conduction gradients are small within the high thermal conductivity PCM. Consequently, it can be seen the hot spot temperature is effectively controlled. At the end of the heat generating pulse, the device temperature reaches a maximum. The hot spot temperature for the PCM case is 135°C, which is 21°C lower than the baseline. Most of PCM in the groove structure is liquid.

The temperature gradient between the hot spot and melt front interface dissipates very quickly after the zero heat generation period begins. However, GaN and Si temperatures are still higher than 118°C. The PCM continues to absorb some sensible heat in GaN and Si layers causing more PCM to melt. At $t = 4.1 \mu\text{s}$ the temperature of GaN, Si and PCM becomes equalized at 118°C. At this point the melt front stops progressing, and actually begins to regress towards the junction as heat is transferred to the heat sink. During this solidification process, the temperature of the GaN, Si and PCM remains around 118°C. All of the latent heat is released at $t = 50.8 \mu\text{s}$ as the PCM has completely re-solidified. The device temperature drops as some sensible heat is removed

from the device. At the end of the duty cycle, the temperature of GaN, Si and PCM returns to its initial value of 97°C.

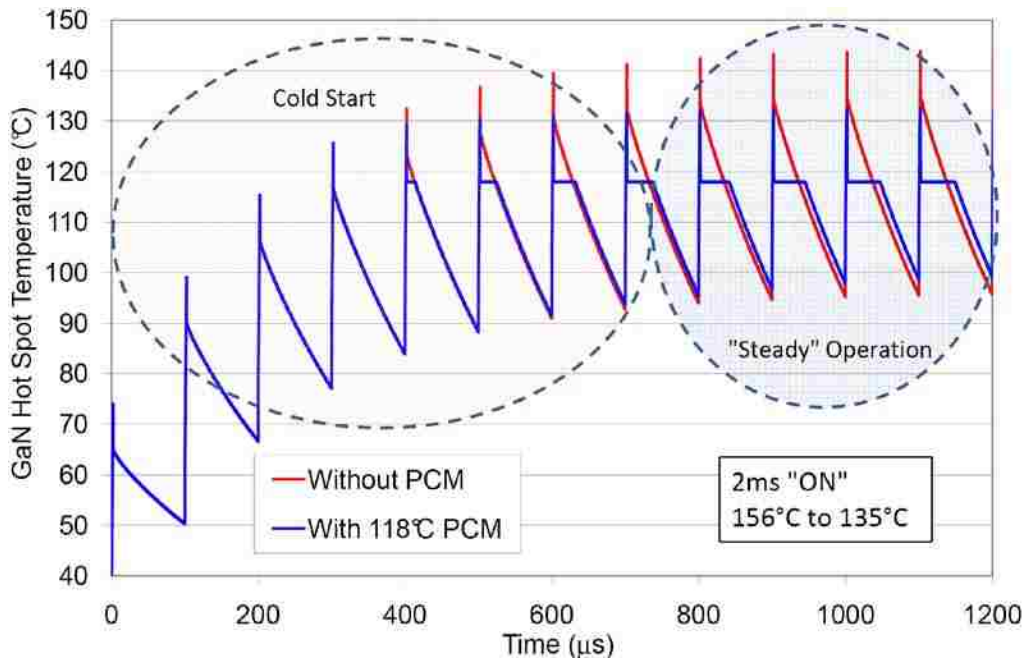


Figure 7.3 Transient thermal result for GaN device under pulsed operating conditions with and without PCM.

Figure 7.4 shows a plot that illustrates the performance improvement for one PCM groove design. Results for a baseline (No PCM) and 2 different PCM groove structures are plotted. In each case, the amount of power to the device was varied until the maximum operating temperature of 180°C was reached. The PCM case with a 5 μm by 6 μm groove and 140°C melting point PCM performed best, and was able to remove 26% more power while maintaining the same junction temperature for a groove design. However, more work needs to be done to optimize the groove structure and optimize the PCM selection, which should ultimately increase the observed improvement.

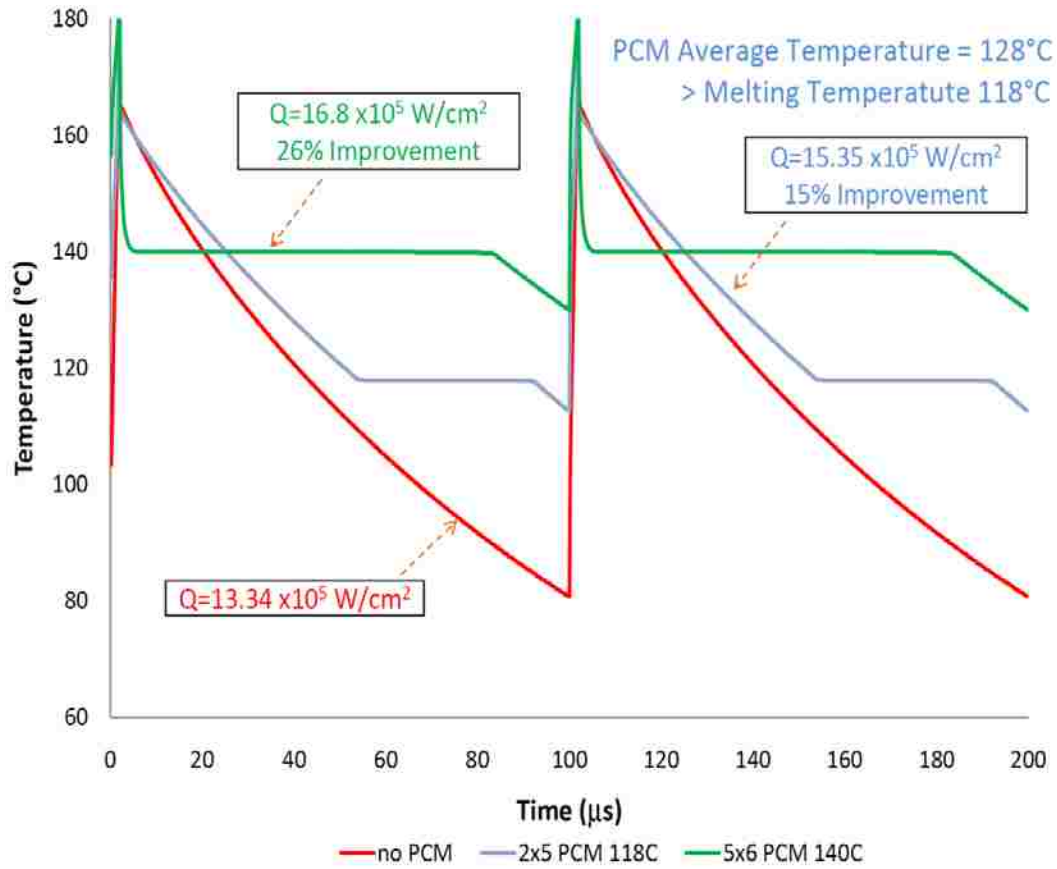


Figure 7.4 Thermal result demonstrating increased power dissipation at constant maximum junction temperature.

7.5 Atomistic-Scale Modeling

As performing Molecular Dynamics (MD) on a Silicon/In₅₂Sn₄₈ was not feasible due to the lack of available interatomic potentials, a simpler Si/In system was chosen as a model system to estimate the thermal resistance between the Si and PCM surfaces. To perform the MD simulations on the Si/In system, the interatomic potentials for Si, In and Si-In were required. Most molecular simulations are based on short-ranged, two-body interactions. One of the popular two-body interatomic potentials is the Lennard-Jones (LJ) potential. However, any reasonable pair potential as well as the Lennard-Jones

potential cannot stabilize the diamond cubic structure of Si and thus, empirical potential models for silicon have been suggested. One empirical potential for silicon is the Stillinger-Weber potential [62], which is known to predict accurate thermal properties. The Stillinger-Weber potential was used for Si. The LJ model was used for In.

The interfacial interaction between indium and silicon was modeled with the LJ interatomic potential [Eq. 7.1]. The parameter σ is the equilibrium interatomic distance and its value was chosen as the average size of the indium and silicon atoms (2.8 Å). The interaction energy between the silicon and indium atom is controlled by the parameter, ϵ . Currently, there are no models available in the literature to represent In-Si interactions. The value of the interaction energy can be derived from experimental input. Using X-ray reflectivity measurement data at the Si-In interface as a benchmark, the value of ϵ was adjusted such that the number density profile from MD simulations closely resembled the experimentally measured density profile [63].

$$\text{Eq. 7.1} \quad \varphi_{\text{LJ},ij}(r_{ij}) = 4\epsilon_{\text{LJ}} \left[\left(\frac{\sigma_{\text{LJ}}}{r_{ij}} \right)^{12} - \left(\frac{\sigma_{\text{LJ}}}{r_{ij}} \right)^6 \right]$$

The X-ray reflectivity data used was taken from experiments on solid Si (100) – liquid In interfaces available in the literature [63]. In brief, the experimental results indicated that the density profile of the liquid In exhibits a first layer at the Si (100) interface with a maximum density that is 28.7% increased with respect to the bulk liquid and a thickness of 24.5Å, as shown in Figure 7.5. It is followed by a second layer of reduced density (-3.3% with respect to the bulk) with a thickness of 17.5Å. A numerical analysis performed to predict whether a hard sphere model can manage to arrange the

spheres in such a way that the electron density is increased to 28% compared to the bulk density on a length of more than 24\AA . It was concluded that the hard sphere model gave a density increase of 23% within a thin slab of $0.6r$, where r is the size of In atom.

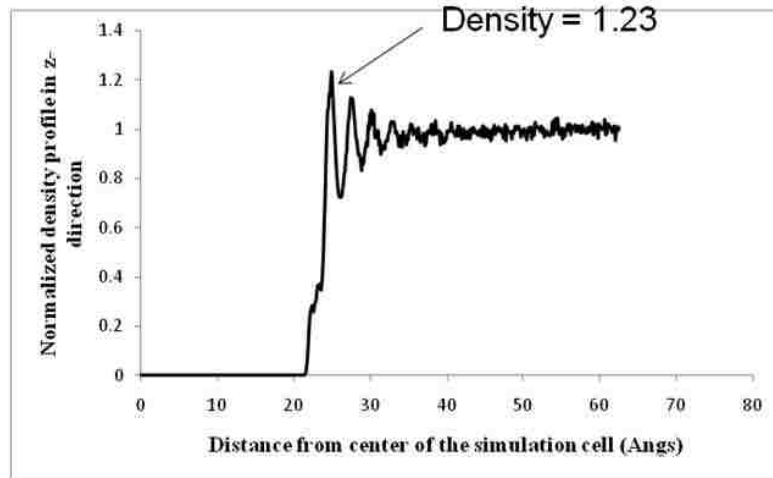


Figure 7.5 Density profile for a Si and In interface [63].

Simulations were performed with various sets of interaction energy parameters between Si and In to match the experimental results and the hard sphere model. The LJ interaction potential under investigation in this project is closer to the hard sphere model. The Si-In interaction energy of 0.02625eV gave a density profile similar to the one predicted by the hard sphere, *i.e.*, density increase of 23% in comparison to the bulk within a thin slab of 5\AA in the first In melt layer next to the interface at 400 K. The simulation temperature of 400 K is $\sim 25\text{ K}$ above the melting temperature estimated from the free energy simulations that were performed. In comparison to the experiments, the peak height of 23% increase was matched but not the peak width of 24\AA . The large width might be due to electronic (metallic) interactions that are not captured in the simple LJ potential model.

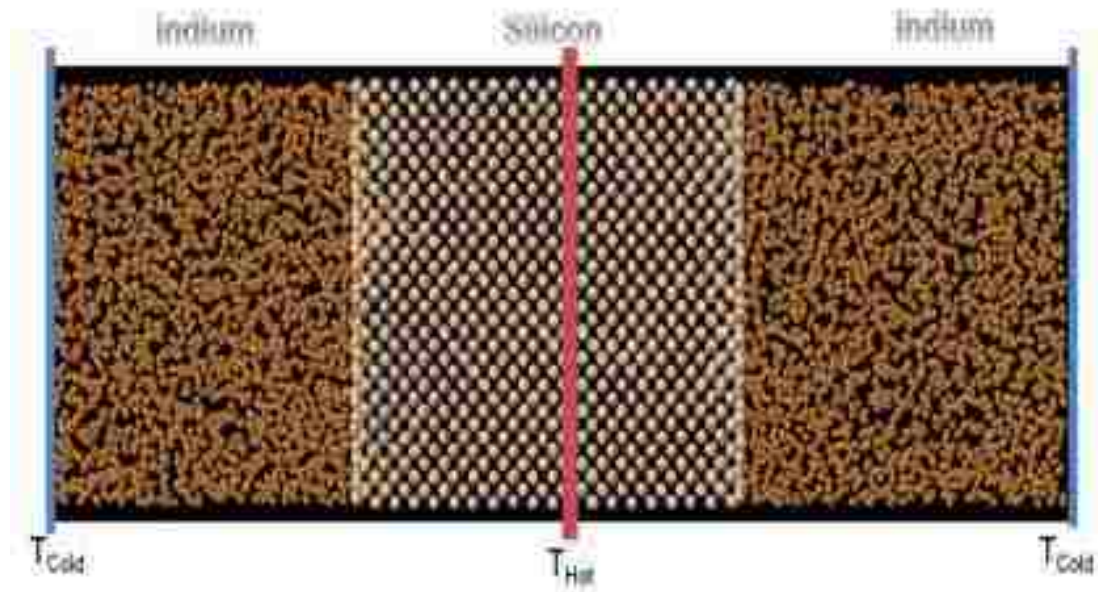


Figure 7.6 Snapshot of silicon-indium atoms at 500K. The red strip represents the hot slab where energy is supplied and the cold strip where equal amount of energy is removed.

A snapshot of the Si/In system is shown in Figure 7.6. In this system 0.0005 eV of energy was added to the hot side (shown in red) and an equal amount of energy was removed from the cold side (shown in blue) to impose the thermal gradient. Periodic boundary conditions are used on all boundaries. In Figure 7.7, the time-averaged temperature profile for the equilibrated silicon-indium bilayer structure at 500 K is plotted. The resultant ΔT of 87 K at the interface is due to the interfacial resistance. The interfacial thermal resistance value is calculated to be $2.71 \times 10^{-8} \text{ m}^2\text{-K/W}$. The calculated thermal resistance value was input to the macro-scale FEA model along the Si/PCM interface (described in the previous section).

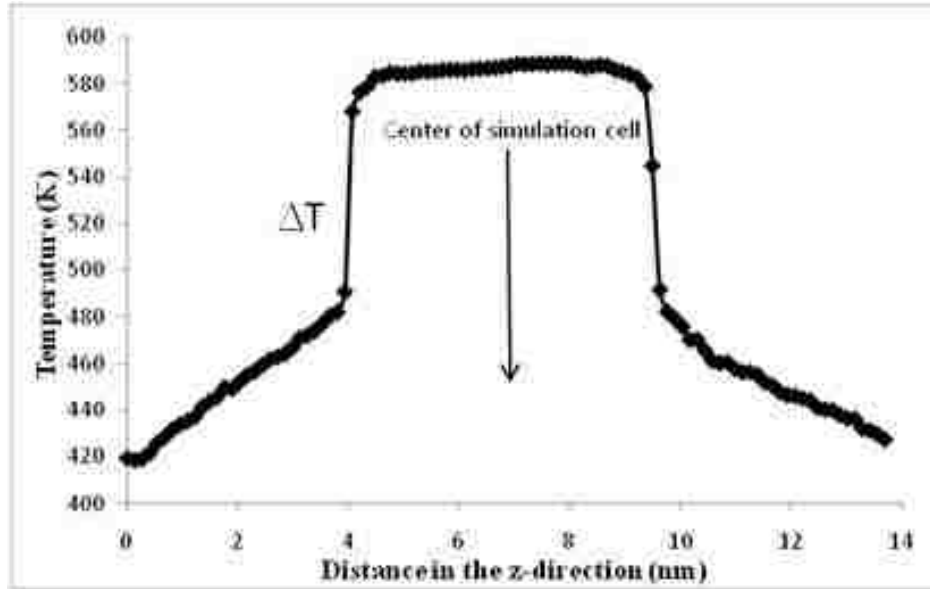


Figure 7.7 Temperature profile across the simulation cell in the z-direction.

7.5 Parasitic Capacitance Modeling

The effect of PCM material in the high frequency performance of GaN HEMTs was also studied. For this task, the software FlexPDE, a commercial partial differential equations (PDE) solver, was used to solve Poisson’s equation and determine the electric field in the device. Using this software a script program was developed to calculate the parasitic capacitances in a GaN HEMT with and without PCM cooling. Figure 7.8 shows a depiction of the modeling domain with a meshing result for the PCM case. The calculated electric fields are shown in Figure 7.9 and Figure 7.10 for the baseline and PCM cases. From the result, it is clear that the electrostatic potentials in the device are changed by the presence of the metallic PCM near the transistor.

Figure 7.11 shows the calculated parasitic capacitances on the source and drain due to the PCM material. The PCM has minimal impact on C_{GS} , regardless of proximity to the transistor. On the other hand, as the distance between the transistor channel and

PCM is reduced below $0.1 \mu\text{m}$, the parasitic capacitance between the gate and the drain rapidly increases. However, thermal modeling results show that locating the PCM within $1\mu\text{m}$ of the transistor is reasonable, so this is not expected to cause any electrical issues.

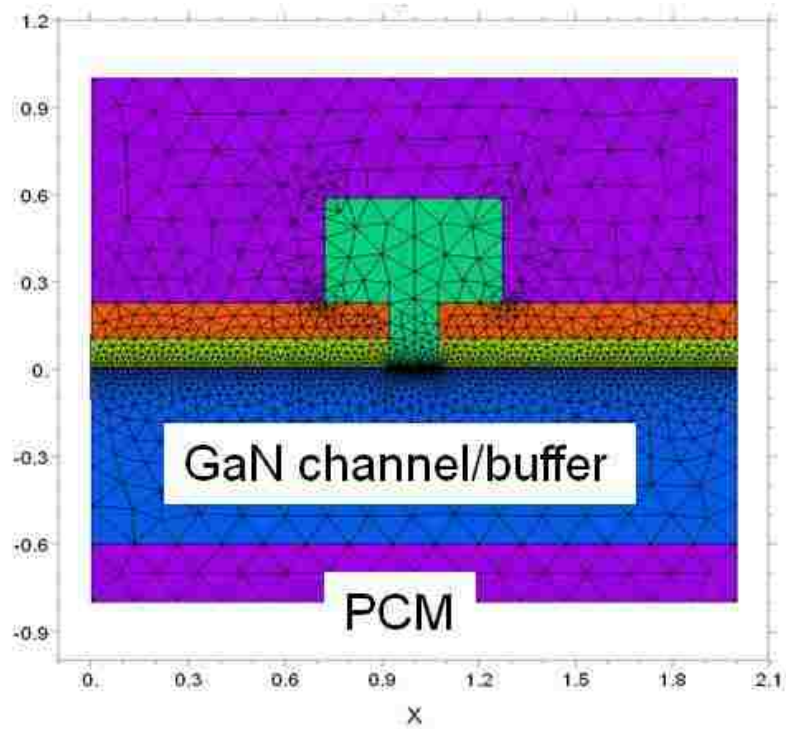


Figure 7.8 Mesh result and material identification for electrostatic potential calculation.

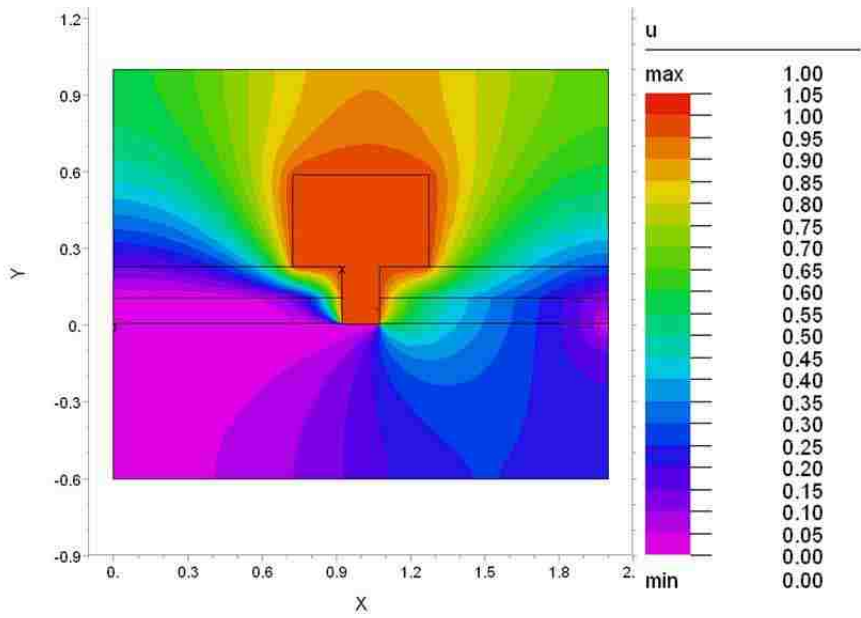


Figure 7.9 Normalized electrostatic potential for baseline case (without PCM).

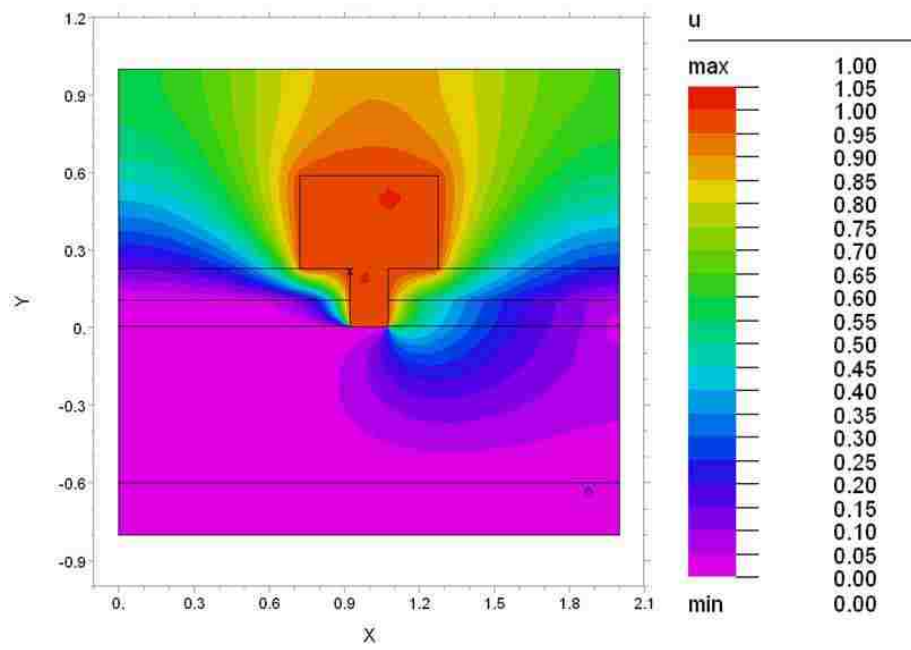


Figure 7.10 Normalized electrostatic potential for case with PCM.

	C_{GS} (pF/mm)	C_{GD} (fF/mm)
No PCM	4.26	109
PCM to GaN Thickness		
2 μm	4.26	109
1 μm	4.26	110
0.1 μm	4.26	118
0.01 μm	4.26	180

Figure 7.11 Parasitic capacitances for the source and drain are tabulated for the baseline case (no PCM) and PCM as a function of distance.

Another possible parasitic capacitance may result due to the overlapping of the PCM and contact pads. Figure 7.12 shows the result of this calculation. Having capacitance as close to zero as possible is desired. To minimize the effect, it is important to make sure that the PCM material does not overlap more than 1 μm or 2 μm with the source and drain pads.

	$C_{\text{pads,PCM}}$ (pF/mm. μm)
PCM to GaN Thickness	
2 μm	0.008
1 μm	0.017
0.1 μm	0.17
0.01 μm	1.7

Figure 7.12 Parasitic capacitances for the between the pad and PCM are tabulated.

7.6 Conclusions and Future Work

This work proposes a new junction level thermal storage technology capable of increasing the maximum thermal power dissipation of pulsed devices by using metallic PCMs. A multiscale model was developed to predict the thermal performance improvement of the junction level thermal storage concept as compared to baseline devices. MD was used to predict the interfacial resistances values. The MD effort involved development of interatomic potential for Si-In interactions, including use of an experimental density profile to fit parameters for an LJ potential. The interfacial resistances predicted by MD were then incorporated in a FEA model to perform transient thermal calculations. The FEA results showed that 26% more power could be dissipated for the groove designed and operating conditions studied. Larger increases in performance are expected for alternative groove designs and operating conditions. Electrical calculations were also performed to evaluate performance degradation mechanisms that the metallic PCM causes during high frequency device operation. Parasitic capacitance predictions indicate the PCM should not interfere with the electrical performance of the device provided that the PCM is located 1 μ m from the junction and contact pads.

Chapter 8

Jet Impingement of Flat Angled Sprays

8.1 Overview

Impingement cooling methods, such as spray cooling and jet impingement have demonstrated the capability of cooling high heat flux surfaces while maintaining a low thermal resistance. Most spray cooling and jet impingement experiments attempt to measure the average heat transfer coefficient, even though it is known that heat transfer coefficients are known to change as a function of distance from the impact zone. Secondly, most experiments are done on thick uniformly heated surfaces although most electronic devices are very thin ($<0.2\text{mm}$) and generate heat very non-uniformly with very large peak heat fluxes ($>1000\text{W}/\text{cm}^2$) over very small areas ($<0.25\text{mm}^2$). In this study an accurate measurement of the uniformity of the spray cooling thermal solution was attained using an Intel® supplied thermal test vehicle [64]. The heater block is a thin silicon chip ($<0.25\text{mm}$ thick and 7cm^2 in surface area) delivering a uniform heat flux to $70\text{W}/\text{cm}^2$. The platform also has the ability to power large peak heat fluxes ($>1000\text{W}/\text{cm}^2$) over small areas ($<0.25\text{mm}^2$). Experiments using jet impingement with flat spray nozzles angled to the surface were conducted with water, methanol, and HFE-7000. The axial heat transfer coefficient variation was measured under uniform heat loading. Finally, the measurements are compared to modified models from the literature with good agreement.

8.2 Nomenclature

α	Angle ($^{\circ}$)
β	Correction factor for angled impingement

ν	Fluid kinematic viscosity (m^2/s)
d	Nozzle diameter (m)
D	Tube Diameter (m)
h	Heat transfer coefficient ($\text{W}/\text{m}^2\text{-K}$)
H	Nozzle to surface distance (m)
k	Fluid thermal conductivity ($\text{W}/\text{m-K}$)
m	Power law factor for single slot nozzle correlation
\overline{Nu}	Spatially averaged Nusselt number for angled flat spray cooling
\overline{Nu}_M	Spatially averaged Nusselt number from Martin Correlation
\overline{Nu}_T	Spatially averaged Nusselt number from Tawfek Correlation
Nu_x	Local Nusselt number for flat angled spray cooling
Pr	Fluid Prandtl number
Re	Jet Reynolds Number
V	Velocity of fluid exiting nozzle
x	Axial position from fluid impact region (m)
y	Transverse direction from nozzle (m)

8.3 Background and Introduction

Single phase jet impingement heat transfer has been given a great deal of attention in the literature due to its ability to dissipate high heat fluxes at low thermal gradients [65]. Jet impingement has been used in many applications ranging from turbine blade cooling to plasma facing components to high density microelectronics applications [66]. Gas impinging jets were first studied with respect to turbine blade cooling. However,

heat transfer coefficients orders of magnitude higher than gas jets can be obtained using liquid jets. For the case of liquid jets, two types exist. One type is a submerged jet. In this case the nozzle ejects water through a pool of liquid. The second type is a free surface jet, where the liquid jets through stagnant air before hitting the surface. The experimental data acquired in this study is of the free surface variety using liquids.

The current study is limited to flat sprays that are angled to the surface (as opposed to spraying normal to the surface). A diagram of the spray cooling system studied is shown in Figure 8.1. The motivation behind this study was unique to a semiconductor debug process, where the back side surface of the chip needs to be accessible while the chip is heated under typical thermal loadings experienced in real world computer processors. The nature of the process requires removal of any heat sink and thermal interface material traditionally used to cool the back side of the silicon chip. Only direct fluid technologies are capable of cooling the chip while the back side of the silicon is accessed. The goal of this study was to measure the local temperature of the chip under thermal loading using the proposed flat angle spray cooling system. To take these local measurements under realistic thermal conditions and chip geometries an Intel® supplied thermal test vehicle was utilized. The thermal test vehicle is unique in its ability to measure accurate real time temperatures, while generating the necessary heat flux through the silicon chip surface. In the required process, the chip junction temperature was required to be controlled within 2°C between -10°C and 110°C. Three fluids were studied using the proposed cooling system to meet the various temperature ranges: water, methanol and HFE-7000.

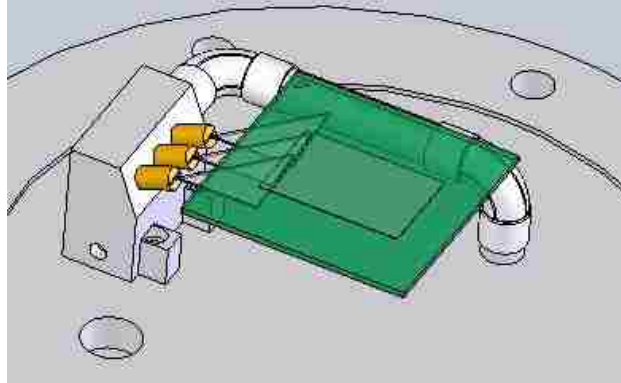


Figure 8.1 A diagram illustrating the spray cooling system studied in this paper is shown. Liquid exits an array of nozzles forming a flat spray. The spray impacts the surface of the silicon chip (shown as semi-transparent) at an angle to the surface, directly on the edge of the chip. The chip itself is held in place by a metal clamp, not shown.

8.4 Modeling of Local Heat Transfer Coefficients with Flat Angled Sprays

Multiple models exist in the literature to predict heat transfer coefficients in jet impingement systems [67; 68; 69]. A well referenced model in the literature, especially for electronics cooling applications, is the Martin correlation for single slot nozzles [70]. The Martin correlation for single slot nozzles is known to work well for predicting average heat transfer coefficient for jet impingement systems [71]. However, some modifications need to be made to the spatially average model to make comparisons to the local heat transfer coefficients measurements acquired in this study. The current study also requires adjustments to be made for the effect of angling the nozzles. The Martin single slot nozzle correlation is for nozzles angled normal to the surface. Tawfek has proposed a correlation for impingement on a tube that includes a power law factor describing the effect on the heat transfer coefficient due to nozzle angle. A model is proposed here to model flat angled spray cooling heat transfer coefficients by combing

the Martin model with the power law angle effect of the Tawfek model. To capture the local heat transfer coefficient variations, the combined model (which is spatially averaged) is then differentiated to calculate local values of the Nusselt number.

A summary of the Martin model for single slot nozzle cooling and its application to the proposed study is described. The Nusselt number for jet impingement is shown in Eq. 8.1. The Nusselt number for the Martin single slot nozzle correlation is calculated using terms for physical property values, flow conditions and geometric considerations as shown in Eq. 8.2. The physical property values are accounted for by a Prandtl number effect. The flow conditions are characterized by the jet Reynolds number, described by Eq. 8.4. The power law factor, m , for the Reynolds number is also a function of geometric considerations as described by Eq. 8.3. The geometric considerations include the length of the heated surface, L , distance between the nozzle and impact zone, H , and the hydraulic diameter of the nozzle, d . It should be noted for slot nozzles the hydraulic diameter is equal to twice the width of the slot. However, in the current study a flat spray nozzle was used with an elliptical shape. An effective hydraulic diameter was used as specified by the nozzle vendor.

$$\text{Eq. 8.1} \quad \overline{Nu} = \frac{hd}{k}$$

$$\text{Eq. 8.2} \quad \frac{\overline{Nu}_M}{Pr^{0.42}} = \frac{3.06}{\frac{x}{d} + \frac{H}{d} + 2.78} Re^m$$

$$\text{Eq. 8.3} \quad m = 0.695 - \left[\left(\frac{x}{2d} \right) + \left(\frac{H}{2d} \right)^{1.33} + 3.06 \right]^{-1}$$

$$\text{Eq. 8.4} \quad \text{Re} = \frac{Vd}{\nu}$$

In the current application, available space allows only an angled solution due to the required access to the chip surface. The jet will not impinge perpendicular to the surface, but at an angle of approximately 20°. The Tawfek correlation provides a power law factor accounting for the angle of the impinging nozzle which must be included [72; 73; 74]. Although the complete Tawfek model is not as accurate as the Martin model for electronics applications, the power law factor was separated from the complete Tawfek correlation and combined with the Martin correlation. The Tawfek correlation containing the angle factor and the range of applicability for the angled factor are shown in Eq. 8.5 and Eq. 8.6.

$$\text{Eq. 8.5} \quad \overline{Nu_T} = 0.142 \text{Re}^{0.71} \alpha^{0.194} \left(\frac{H}{d}\right)^{-0.14} \left(\frac{d}{D}\right)^{-0.35}$$

$$\text{Eq. 8.6} \quad 20^\circ \leq \alpha \leq 90^\circ$$

The complete model for local heat transfer coefficient measurement is described here. The power law factor, β , derived from the Tawfek correlation is shown in Eq. 8.7. The factor is normalized to 90° to match the angle at which the Martin correlation is applicable (normal to the surface). To create a spatially average flat angled spray model, the Nusselt number correlation from Martin is multiplied by the angled factor in Eq. 8.8. Some manipulation of the model was completed to transform the spatially averaged model into a local Nusselt number model. The spatially averaged model is described by

Eq. 8.9 as an integral of the local Nusselt number over the length of the heated surface divided by the total length of the surface. Figure 8.4 diagrams the axial position of the fluid, x . The desired local Nusselt number can be solved for by multiplying by the length, x , and differentiating. The end result is shown in Eq. 8.10. A numerical solution was used to calculate local Nusselt numbers and the corresponding local heat transfer coefficients.

$$\text{Eq. 8.7} \quad \beta = \left(\frac{\alpha}{90^\circ} \right)^{0.194}$$

$$\text{Eq. 8.8} \quad \overline{Nu} = \overline{Nu}_M \beta$$

$$\text{Eq. 8.9} \quad \overline{Nu} = \frac{\int_0^x Nu_x dx}{x - 0}$$

$$\text{Eq. 8.10} \quad Nu_x = \frac{d(\overline{Nux})}{dx}$$

8.5 Test Setup and Thermal Test Vehicle

A spray cooling test section was integrated with an Intel® supplied 34980A thermal test platform to acquire data in this study. The thermal test platform is an integrated thermal testing system including the thermal test vehicle, power supplies, data acquisition system, and Labview interface. The thermal test vehicle (TTV) is a silicon chip with two large embedded resistive heaters, four micro-heaters for delivering peak heat fluxes and 29 resistance temperature detectors (RTD's). The organic substrate measures 37.5 mm by 37.5 mm and the silicon die measures 33 mm by 22 mm. The die is less than 0.25mm thick. The TTV is capable of supplying a uniform heat flux of 70W/cm² across its surface as well as peak heat fluxes over 1000W/cm² over areas less

than 0.25mm^2 at four locations on the die. An Agilent data acquisition system was used to acquire the temperature readings, measure the voltage drop across and current through the resistive heaters in the die and calculate the corresponding uniform heat flux provided to the silicon. Each test vehicle is independently calibrated in a thermal bath filled with fluorocarbon at -10°C , 50°C , and 90°C . The accuracy of the temperature readings of the RTD's are accurate to within 0.1°C .

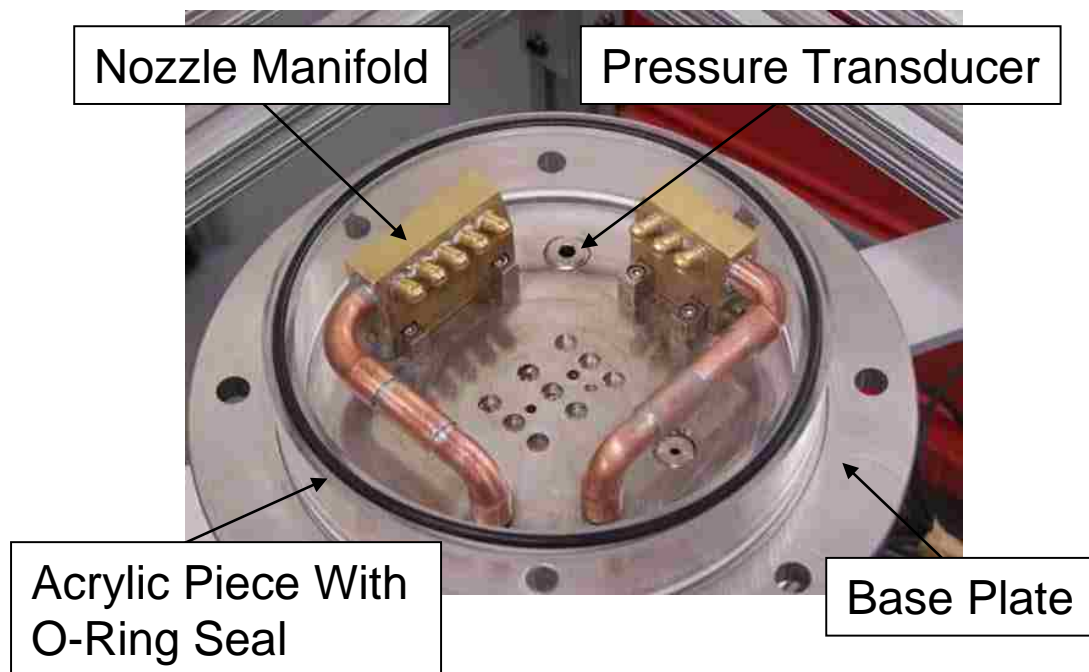


Figure 8.2 Photograph showing spray cooling system hardware. Not shown is the thermal test vehicle which sits above the nozzle arrays centered between the arrays. There is also a plate which created a liquid tight seal around the cooling solution and test vehicle.

The thermal test vehicle sits above a flat angled nozzle array as shown previously in Figure 8.1. The nozzles are at a 20° angle to the TTV. Also shown is the fluid exiting

the nozzles making a flat spray pattern as the fluid impacts the edge of the chip. The nozzles were tilted at a 5° angle (rotational) to avoid the intersection of flow before the spray impacts the chip. The spray exits the flat spray nozzle at a 20° angle to the surface of the chip. The nozzles were overlapped 50% in order to have flow distributed uniformly over the edge of the die. As the fluid exits the die it is collected and recirculated through the system by a pump. A photograph of the cooling system test section is shown in Figure 8.2. The fluid exiting the test section drained to a heat exchanger system to cool the fluid to the desired temperature. The system was capable of cooling the methanol and HFE-7000 fluids to temperatures below -35°C.

8.6 Experimental Data

Local spray cooling heat transfer coefficient test data were acquired at uniform power input for three fluids: water, methanol and HFE-7000. Water was used to test at ambient conditions while HFE-7000 and methanol were tested at sub-ambient conditions. Water is the fluid of choice for its superior physical properties. However, water is limited to keeping the chip at above ambient conditions because of freezing concerns at lower temperatures. Methanol and HFE-7000 were chosen for the sub-ambient conditions because of their low freezing points. Methanol is expected to have higher heat transfer coefficients than HFE-7000, but flammability, toxicity and chemical compatibility make it less attractive as a cooling medium. HFE-7000 has inferior thermophysical properties to methanol, but is inherently safe and chemically compatible with the chip. HFE-7000's dielectric properties are also more attractive for direct cooling of electronic chips.

Water was sprayed at a total flow rate of 1000mL/min through the three 0.020” diameter nozzles at a temperature of 26.7°C. A heat flux of 42W/cm² was applied to the die uniformly. Methanol was sprayed to the chip at a flow rate of 1250mL/min and a -31.6°C inlet temperature. HFE-7000 was sprayed at a total flow rate of 1300mL/min at -29.7°C. The uniform heat flux applied to the die for the methanol and HFE-7000 testing was 14W/cm².

Figure 8.3 shows a plot of the experimental heat transfer coefficient data versus axial position (in the x-direction) away from the impact zone for the three fluids at their respective test conditions. A diagram of the coordinate system used is shown in Figure 8.4. The thermal test vehicle has RTD’s spread across the die at various x-y coordinates. There is expected to be some variation in the heat transfer coefficient in the direction along the impact zone of the spray (y-direction) due to non-uniform velocity profiles. However, this variation is neglected and only variation in the x-direction is studied. Position 0.0cm signifies the location of the impact of the spray. At the impact zone the maximum heat transfer coefficient is measured for all three fluids. The heat transfer coefficient then decreases as the fluid travels away from the impact zone due to the decrease in momentum of the fluid in the boundary layer and resulting increase in thickness of the boundary layer.

The experimental water data are plotted against the local heat transfer coefficient model predictions in Figure 8.5. Overall there was good agreement with water data in terms of both slope and absolute value. However, there was a tendency for the model to over predict most measured values by approximately 25%. At the impact zone, heat

transfer coefficients over $7 \text{ W/cm}^2\text{-}^\circ\text{C}$ were measured. Towards the end of the test chip (3.3cm) heat transfer coefficient values approached $1 \text{ W/cm}^2\text{-}^\circ\text{C}$.

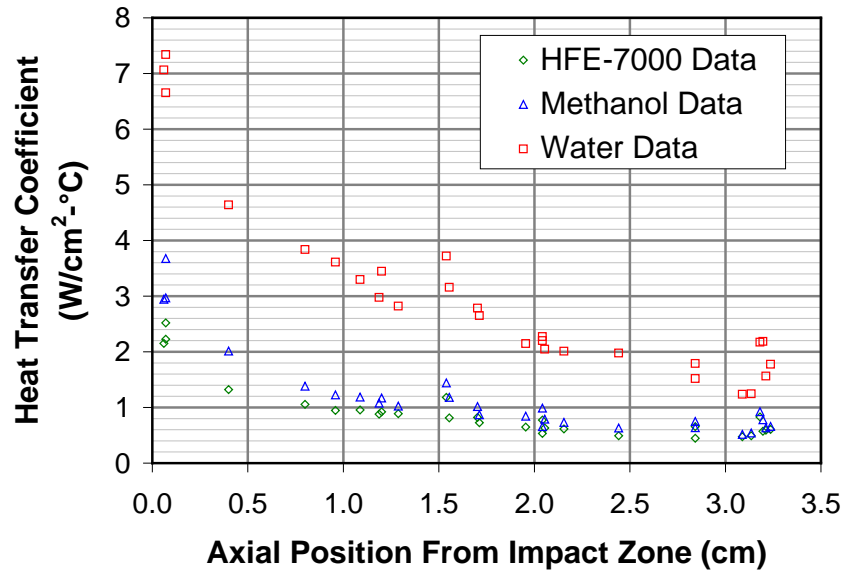


Figure 8.3 Summary plot of experimental local heat transfer coefficients for all three fluids. The highest heat transfer coefficients were measured for water. Methanol heat transfer coefficients were higher than that of HFE-7000 at the impact zone, but matched those of HFE-7000 near the end of the chip surface.

The experimental methanol data are plotted against predictions in Figure 8.6. The model predictions for methanol tended to over predict values by 50%. The maximum heat transfer coefficient in the impact zone was $3.6 \text{ W/cm}^2\text{-}^\circ\text{C}$. The minimum measured heat transfer coefficient was $0.5 \text{ W/cm}^2\text{-}^\circ\text{C}$.

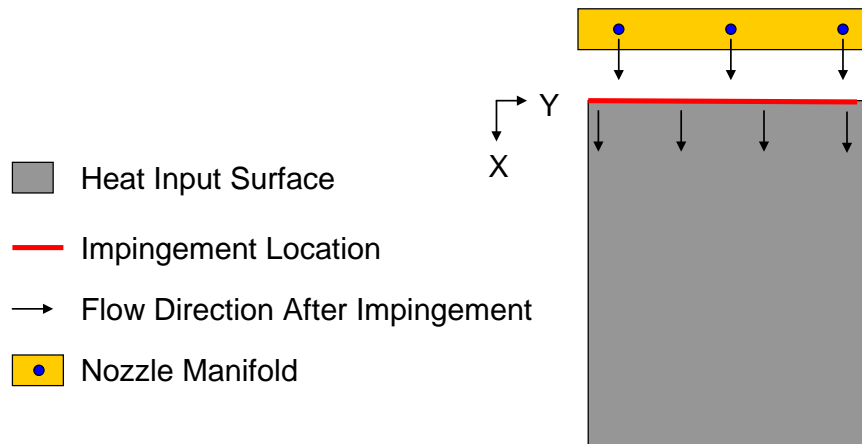


Figure 8.4 Diagram illustrating the impact region location of the spray on the chip surface and direction of resulting flow. The coordinates referred to in Figure 8.3, Figure 8.5, Figure 8.6, and Figure 8.7 are also indicated.

The experimental HFE-7000 data are plotted against predictions in Figure 8.7. The model predictions for HFE-7000 tended to over predict values by 25%. The maximum heat transfer coefficient in the impact zone was $2.5 \text{ W/cm}^2\text{-}^\circ\text{C}$. The minimum measured heat transfer coefficient was $0.45 \text{ W/cm}^2\text{-}^\circ\text{C}$. Interestingly, the measured values for the heat transfer coefficient of HFE-7000 at the end of the chip were very similar to that of methanol, even though methanol had a significantly higher heat transfer coefficient in the impact zone. It is expected that the increased viscosity of methanol causes a faster rate of momentum loss in the boundary layer near the wall compared to HFE-7000. The momentum loss causes a boundary layer thickening and reduction in heat transfer coefficient.

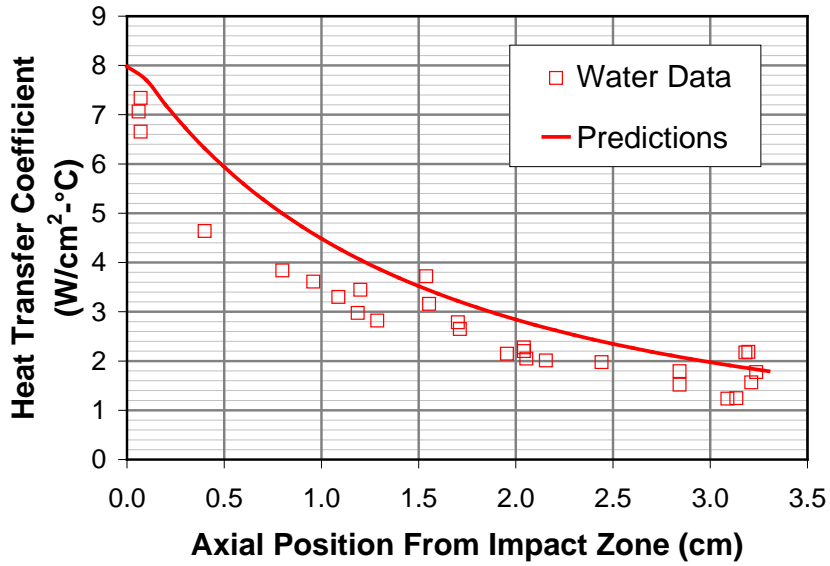


Figure 8.5 Local spray cooling data for water are shown, illustrating the decrease in heat transfer coefficient as a function of length. Comparison to model predictions is also shown.

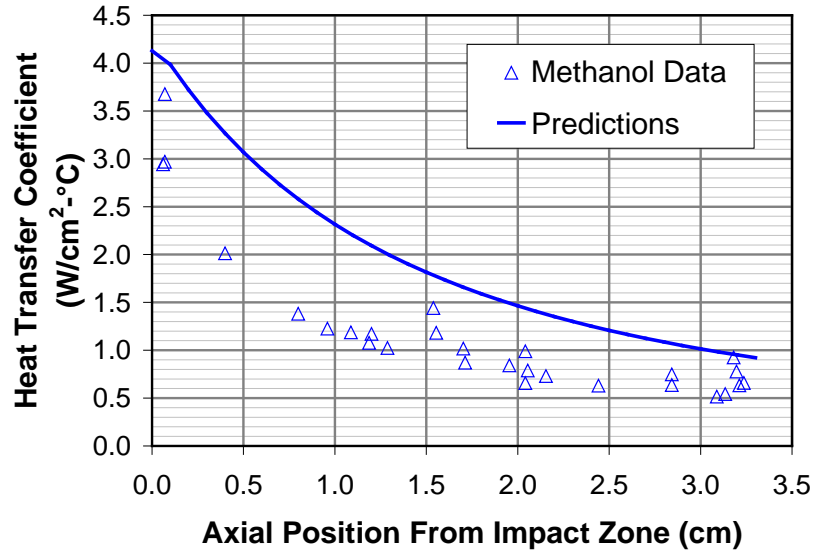


Figure 8.6 Local spray cooling data for methanol are shown, illustrating the decrease in heat transfer coefficient as a function of length. Comparison to model predictions is also shown.

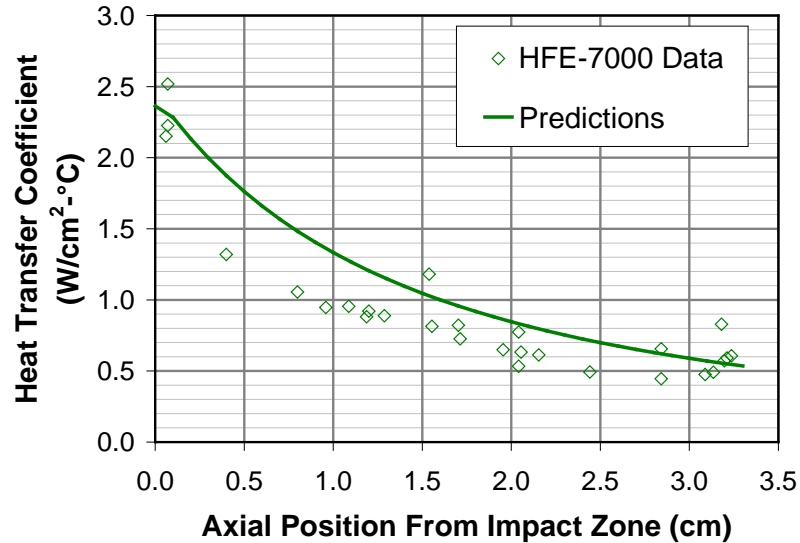


Figure 8.7 Local spray cooling data for HFE-7000 are shown, illustrating the decrease in heat transfer coefficient as a function of length. Comparison to model predictions is also shown.

8.7 Conclusions and Future Work

Experimental data were acquired for a flat spray cooling system with nozzles angled to the surface of a silicon chip. The use of a thermal test vehicle allowed for local accurate measurements of the heat transfer coefficient across the chip. Data was acquired for water, methanol and HFE-7000 at ambient and sub-ambient temperatures. Water performed the best, and would be chosen for applications requiring ambient junction temperatures and above. Methanol slightly outperformed HFE-7000 in the sub-ambient temperature ranges. However, HFE-7000 is the fluid of choice in the cold temperature range because the better performance associated with methanol does not justify its flammability, toxicity and chemical compatibility concerns. A local heat transfer coefficient model for the flat angled spray cooling system was derived by combining a Martin slot nozzle correlation with a Tawfek model for angled impingement. The

spatially averaged model was then differentiated to determine a local heat transfer coefficient model. The model was compared to experimental data with good success.

Bibliography

- [1] Collier, J.G. Thome, J.R., *Convective Boiling and Condensation*,. NY : Oxford University Press, 1994.
- [2] Bejan, A., Kraus, A.D., *Heat Transfer Handbook*. NJ : John Wiley & Sons, 2003.
- [3] Rohsenow, W.M. Hartnett, J.P. Cho, Y.I., *Handbook of Heat Transfer*. NY : McGraw-Hill, 1998.
- [4] Ma, X., Rose, J.R., Xu, D., Lin, J., Wang, B., "Advanced in dropwise condensation heat transfer: Chinese research." *Chemical Engineering Journal*, 2000, pp. 87-93, v78.
- [5] Daniel, S., Chaudhury, M.K., Chen, J.C., 2001, “,” *Science*,., "Fast drop movements resulting from the phase change on a gradient surface." *Science*, 2001, pp. 633-636 v291(5504).
- [6] Das, A. K., Kilty, H .P., et al., "Dropwise Condensation of Steam on Horizontal Corrugated Tubes Using an Organic Self-Assembled Monolayer Coating." *Journal of Enhanced Heat Transfer*, 2000, p. 109–123 v7(2).
- [7] Das, A. K., Kilty, H. P., Marto, P. J., et al., "The use of an organic self-assembled monolayer coating to promote dropwise condensation of steam on horizontal tubes." *ASME. J. Heat Transfer*, 2000, p. 278–286 v122(2).
- [8] Dunn, P.D., Reay, D.A., *Heat Pipes*. Tarrytown, NY : Pergamon, 1994.
- [9] Fan, A., Bonner, R., et al., "An Innovative Passive Cooling Method for High Performance Light-emitting Diodes." San Jose, CA : s.n., 2012. Semi-therm.

- [10] Zuo, J., Anderson, W., Bonner, R., "Advanced Thermal Management Technologies for High Power Automotive Equipment." Troy, Michigan : s.n., 2008. National Defense Industrial Association Ground Vehicle Power and Energy Workshop.
- [11] Bonner III, R.W., "Condensation on Surfaces with Graded Hydrophobicity." San Francisco, Ca. : s.n., 2009. ASME Summer Heat Transfer Conference. pp. 491-495.
- [12] Chaudhury, M.K. and Whitesides, G.M., "How to make water run uphill." *Science*, Jun 1992, Issue 5063, Vol. 256, p. 1539.
- [13] Incropera, F.P., Dewitt, D.P., *Fundamentals of Heat and Mass Transfer*. NY : John Wiley & Sons, 2002.
- [14] Faghri, A., *Heat Pipe Science and Technology*. Washington, DC : Taylor & Francis, 1995.
- [15] Hartenstine, J., Bonner, R., et al., "Loop Thermosyphon Design for Cooling of Large Area, High Heat Flux Sources." Vancouver, Canada : s.n., 2007. InterPACK.
- [16] Schmidt, E., Schurig, W., Sellschopp, W., "Versuche uber die Kondensation in Film- und Tropfenform." *Tech. Mech. Thermodynamik*, 1930, Vol. 1, pp. 53-63.
- [17] Rose, J., "Condensation heat transfer fundamentals." *Chemical Engineering Research and Design*, 1998, Issue A2, Vol. 76, pp. 143-152.
- [18] Rose, J. W., "Dropwise condensation theory and experiment: a review." 2002. *Proceedings Institute of Mechanical Engineers Part A: J. Power and Energy*. pp. 115-128, 216(2).
- [19] Bonner, R.W., "Dropwise Condensation Life Testing of Self-Assembled Monolayers." Washington, D.C. : s.n., 2010. International Heat Transfer Conference.

- [20] Vemuri, S., Kim, K. J., Wood, B. D., et al., " Long term testing for dropwise condensation using self- assembled monolayer coatings of n-octadecyl mercaptan." Applied Thermal Engineering, 2006, p. 421–429 v26(4).
- [21] Bonner, R.,, "Dropwise Condensation on Vapor Chambers." Santa Clara, Ca : s.n., 2010. Semi-therm.
- [22] Daniel, S, Chaudhury, M.K. and Chen, J.C., "Fast drop movements resulting from the phase change on a gradient surface." Science, 2001, pp. 633-636 v291(5504).
- [23] Boreyko, J., et.al., "Planar jumping-drop thermal diodes." Applied Physics Letters, 2011, Issue 23, Vol. 99, p. 234105.
- [24] Chen, L., Liang, S., Yan, R., et al., 2009, “., "n-octadecanethiol Self-Assembled Monolayer Coating with Microscopic Roughness for Dropwise Condensation of Steam." Journal of Thermal Science , 2009, p. 160–165 V18(2) .
- [25] Bonner III, R.W., "Correlation for dropwise condensation heat transfer: Water, organic fluids and inclination." s.l. : International Journal of Heat and Mass Transfer, 2013.
- [26] Le Ferve, E.J., Rose, J., "A theory of heat transfer by dropwise condensation." Chicago, Il. : s.n., 1966. 3rd International Heat Transfer Conference. pp. 362-375.
- [27] Rose, J., "On the mechanism of dropwise condensation." International Journal of Heat and Mass Transfer, 1967, Vol. 10, pp. 755-762.
- [28] Rose, J., Glicksman, L., "Dropwise Condensation - the distribution of drop sizes." International Journal of Heat and Mass Transfer, 1973, Vol. 16, pp. 411-425.
- [29] Zisman, W.A., "Contact Angle, Wettability and Adhesion." Advances in Chemistry Series, 1964, Vol. 43, pp. 1-51.

- [30] Stylianou, S.A. and Rose, J.W., "Dropwise condensation on surfaces having different thermal conductivities." *Journal of Heat Transfer*, August 1980, Issue 3, Vol. 102, pp. 477-482.
- [31] Utaka, Y., et al., "Transition from Dropwise Condensation to Film Condensation of Propylene Glycol, Ethylene Glycol and Glycerol Vapors." Honolulu, HI : s.n., 1987. *Proceedings of the 1987 ASME-JSME Thermal Engineering Joint Conference*. pp. 377-384.
- [32] Koch, G., Zhang, D.C. and Leipertz, A., "Condensation of steam on the surface of hard coated discs." *Warme- und Stoffubertragung Zeitschrift*, 1997, Issue 3, Vol. 32, pp. 149-156.
- [33] Rose, J., "Dropwise Condensation Theory." *International Journal of Heat and Mass Transfer*, 1981, Issue 2, Vol. 24, pp. 191-194.
- [34] Abu-orabi, M., "Modeling of heat transfer in dropwise condensation." *International Journal of Heat and Mass Transfer*, 1997, Issue 1, Vol. 41, pp. 81-87.
- [35] Ge, Z., Cahill, D. G., Braun, P. V., "Thermal conductance of hydrophilic and hydrophobic interfaces." *Physical Review Letters*, 2006, Issue 18, Vol. 96, p. 186101.
- [36] Shenogina, N., Godawat, R., Keblinski, P., Garde, S., "How wetting and adhesion affect thermal conductance of a range of hydrophobic to hydrophilic aqueous interfaces." *Physical Review Letters*, 2009, Issue 15, Vol. 102, p. 156101.
- [37] Gu, Y., et al., "Dropwise condensation heat transfer coefficient on the horizontal surface with gradient surface energy." *Journal of Engineering Thermophysics*, 2005, pp. 820-822 v26(5).

- [38] Liao, Q., et al., "Experimental Investigation of Dropwise Condensation Heat Transfer on the Surface with a Surface Energy Gradient." *Journal of Enhanced Heat Transfer*, 2007, Issue 3, Vol. 14, pp. 243-256.
- [39] Zhao, H. and Beysens, D., "From droplet growth to film growth on a heterogeneous surface. Condensation associated with a wettability gradient." *Langmuir*, 1995, pp. 627-634 v11(2).
- [40] Mehl, D., Dussinger, P., Grubb, K., "Use of vapor chambers for thermal management." 1999. National Electronic Packaging and Production Conference Proceedings of the Technical Program (East and West). pp. 1358-1366, v3.
- [41] Sauciuc, I., Chrysler, G., Mahajan, R., Prasher, R., "Spreading in the heat sink base: Phase change systems or solid metals??" s.l. : IEEE Transactions on Components and Packaging Technologies, 2002, Issue 4, Vol. 25.
- [42] Bonner, R.W., et al., "Passivation coatings for micro-channel coolers." Orlando : Applied Power Electronics Conference and Exposition (APEC), 2012.
- [43] Ashman, S., Kandlikar, S. G., " A review of manufacturing processes for microchannel heat exchanger fabrication." Limerick : s.n., 2006. 4th International Conf. on Nanochannels, Microchannels, and Minichannels.
- [44] Karni, Y., Klumel, G., Levy, M., Berk, Y., & Openhaim, Y., *Active cooling solutions for high power laser diode stacks*. s.l. : 6876 (687604), 2008.
- [45] Truesch, G. e., "Reliability of water cooled high power diode laser modules." 2005. SPIE.

- [46] Feeler, R., Doster, J., Jenghean, J., Kemmer, G., & Stephens, E., *Reliable cooling of high-powe laser diode arrays*. St Charles : Northrop Grumman Cutting Edge Optronics, 2008.
- [47] Reid, M., Punch, J., Galkin, T., Väkeväinen, K., & Stenberg, M., "Oxide Development on Coated Copper Contacts." 2005. 6th Int. Conf. on Thermal, Mechanical, and Multiphysics Simulation and Experiments in Micro-Electronics and Micro-Systems, EuroSim.
- [48] Reid, M., Punch, J., Galkin, T., Vakenevainen, K., & Stenber, T., "Oxide development on coated copper contacts." 2005. IEEE.
- [49] Pinnel, M., & Bennet, J., "Mass diffusion in polycrystalline copper/electroplated gold planar couples." *Met. Trans.*, 1972, Vol. 3, pp. 1989-1997.
- [50] Pinnel, M., & Bennett, J., "Qualitative obervationes on the diffusion of copper and gold through a nickel barrier." *Metallurgical Transactions A*, 1976, Issue 5, Vol. 7, pp. 629-635.
- [51] Corrosion Testing Laboratories, Inc., "Erosion-Corrosion." [Online] 2007. www.corrosionlab.com/papers/erosion-corrosion/erosion-corrosion.htm.
- [52] Technologies, Sundew., *Atomic Layer Deposition*. 2009.
- [53] Bonner, R.W., et al., "Die Level Thermal Storage for Improved Cooling of Pulsed Devices." Santa Clara, Ca : s.n., 2011. Semi-therm.
- [54] Desai, T., Piedra, D., Bonner, R., "Novel Junction Level Cooling in Pulsed GaN Devices." San Diego, CA : s.n., 2012. ITerm.
- [55] Piedra, D., Desai, T., Bonner, R., et al., "Integration of a Phase Change Material for Junction-Level Cooling in GaN Devices." San Jose, CA : s.n., 2012. Semi-therm.

- [56] Tang, X., Bonner, R., Desai, T., Fan, A., "2-D Numerical Study of Micro-Scale Phase Change Material Thermal Storage in GaN Transistor Thermal Management." San Jose, Ca : s.n., 2011. Semi-therm.
- [57] Mishra, U.K., Shen, L., Kazior, T.E., Wu, Y.F., "GaN-based RF power devices and amplifiers." 2008. IEEE.
- [58] Koudymov, A., Hu, X., Simin, K., Simin, G., Ali, M., "Low-Loss High Power RF Switching Using Multifinger AlGaIn/GaN MOSHFETs." IEEE Electron Device Letters, 2002, Issue 449, Vol. 23.
- [59] Oprins, H., Das, J., Ruythooren, W., Vandersmissen, R., Vandeveldel, B., Germain, M., "Thermal Modeling of Multi-Finger AlGaIn/GaN HEMT's." Belgirate, Italy : s.n., 2005. Therminic.
- [60] Mishra, U.K., Parikh, P., Wu, Y.F., "AlGaIn/GaN HEMTs: An overview of device operation and applications." Proceedings of the IEEE, 2002, Issue 6, Vol. 90, pp. 1022-103.
- [61] Shin, S., Kaviany, M., Desai, T., Bonner, R., "Roles of Interfacial Restructuring in Phonon Boundary Resistance." Phys. Rev. B, 2012, Vol. 82, p. 134205.
- [62] Stillinger, F.H, Weber, T.A., Phys. Rev. B., 1985, Vol. 31, p. 5262.
- [63] Denk, M., *Ph.D. Thesis, Structural Investigation of Solid-Liquid Interfaces, Max-Planck-Institut für Metallforschung*. Stuttgart, Germany : Chapter 6, 2006.
- [64] Bonner III, R.W., "Local Heat Transfer Coefficient Measurements of Flat Angles Sprays Using Thermal Test Vehicle." San Jose, CA : s.n., 2008. 24th IEEE Semi-Therm Symposium.

- [65] Incropera, F.P. et al., *Heat transfer in electronic and microelectronic equipment*. New York : A. E. Bergels, Hemisphere Publishing Corporation, 1990, pp. 407-444.
- [66] Lee, D.Y., Vafai, K., "Comparative analysis of jet impingement and microchannel cooling for high heat flux applications." *Int. J. Heat Mass Transfer*, 1999, Vol. 42, pp. 1555-1568.
- [67] Wright, W.B., "An evaluation of jet impingement heat transfer correlations for piccolo tube applications." *AIAA 2004-0062*, 2004, pp. 1-17.
- [68] Ma, C.F., Gan, Y.P, Tian, Y.C., Lei, D.H., Gomi, T., "Liquid jet impingement heat transfer with or without boiling." *J. of Thermal Science*, 1993, Issue 1, Vol. 2, pp. 32-49.
- [69] Wen, M., Jang, K., "An impingement cooling on a flat surface by using circular jet with longitudinal swirling strips." *Int. J. Heat Mass Transfer*, 2003, Vol. 46, pp. 4657-4667.
- [70] Martin, H., "Heat and mass transfer between impinging gas jets and solid surfaces." *Adv. in Heat Transfer*, 1977, Vol. 13, pp. 1-60.
- [71] Bar-Cohen, A., "Thermal management of electronic components with dielectric liquids." *Int. J. JSME*, 1993, Issue 1, Vol. 36, pp. 1-25.
- [72] Tawfek, A.A., "Heat transfer and pressure distributions of an impinging jet on a flat surface." *Heat and Mass Transfer*, 1996, Vol. 32, pp. 49-54.
- [73] Tawfek, A.A., "Heat transfer studies of the oblique impingement of round jets upon a curved surface." *Heat and Mass Transfer*, 2002, Vol. 38, pp. 467-475.
- [74] Yang, G., Choi, M., Lee, J.S., "An experiment study of slot jet impingement cooling on concave surface: effects of nozzle configuration and curvature." *Int. J. Heat Mass Transfer*, 1999, Vol. 42, pp. 2199-2209.

Appendix A

Graphical Comparison of Bonner Model to Dropwise Condensation Data

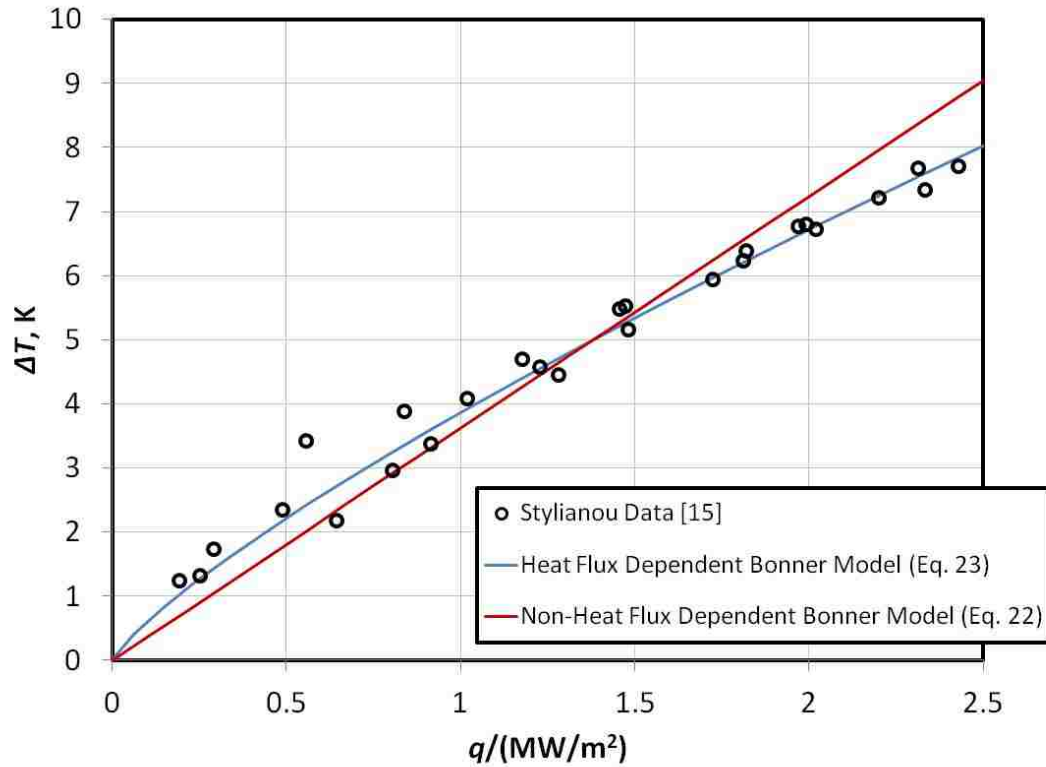


Figure A.1 Predictions from the heat flux and non-heat flux dependent Bonner models are plotted against experimental data acquired by Stylianou for steam at 374 K [30].

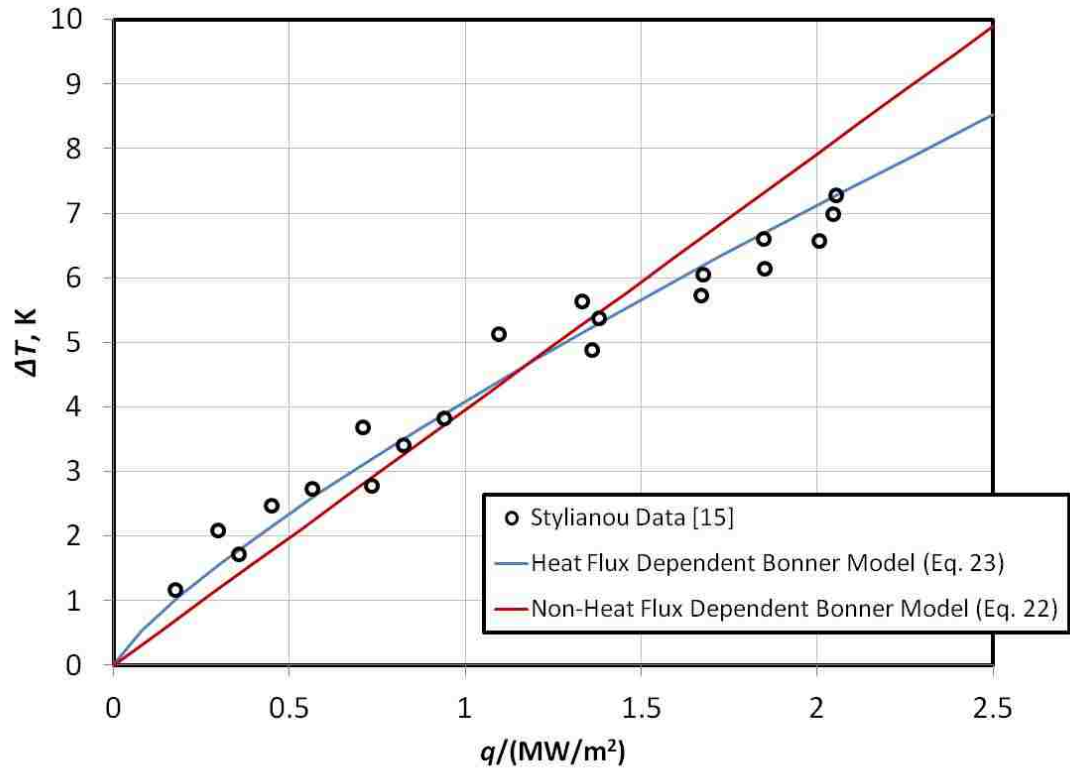


Figure A.2 Predictions from the heat flux and non-heat flux dependent Bonner models are plotted against experimental data acquired by Stylianou for steam at 366 K [30].

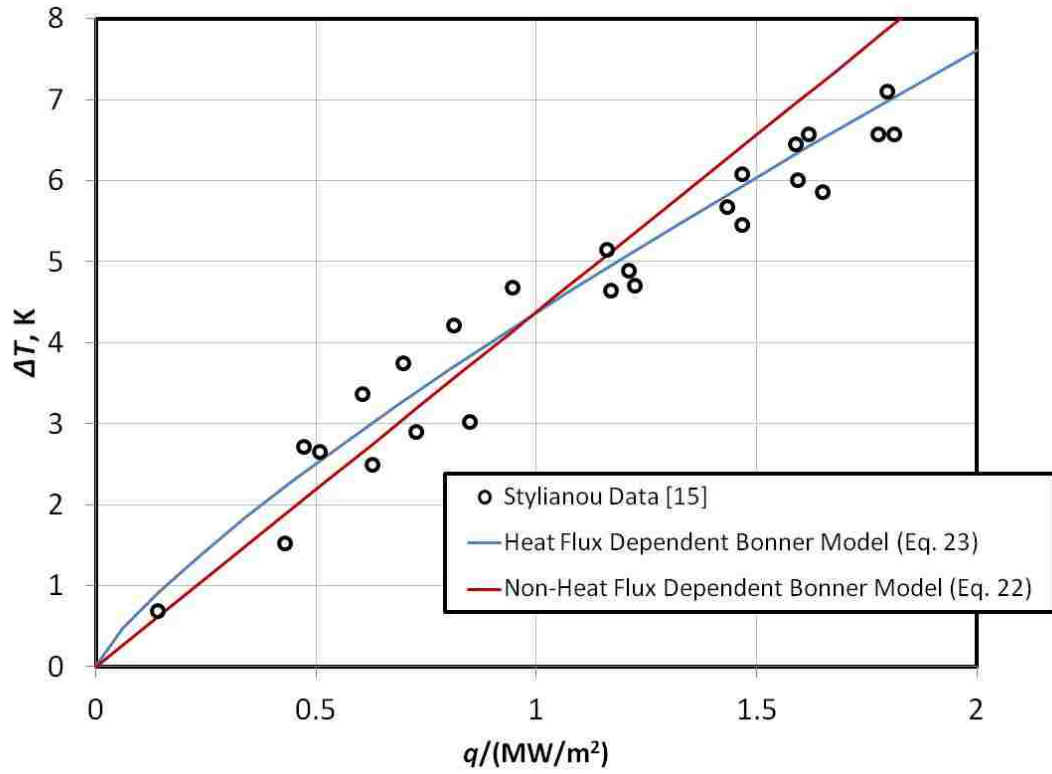


Figure A.3 Predictions from the heat flux and non-heat flux dependent Bonner models are plotted against experimental data acquired by Stylianou for steam at 359 K [30].

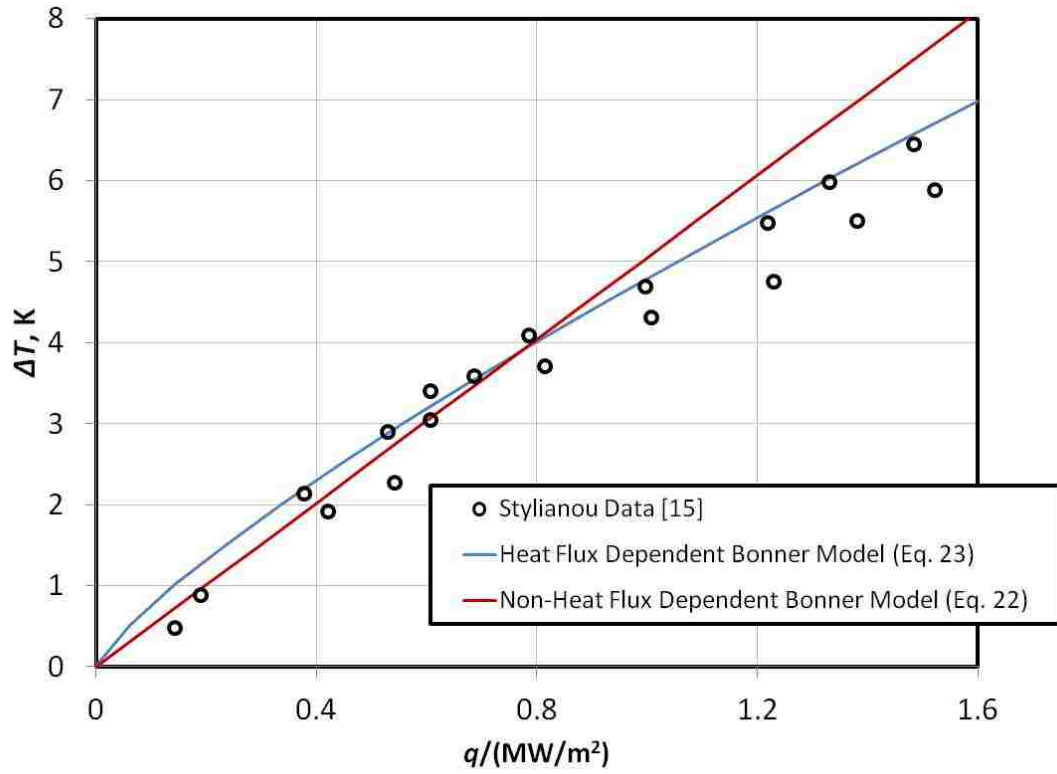


Figure A.4 Predictions from the heat flux and non-heat flux dependent Bonner models are plotted against experimental data acquired by Stylianou for steam at 348 K [30].

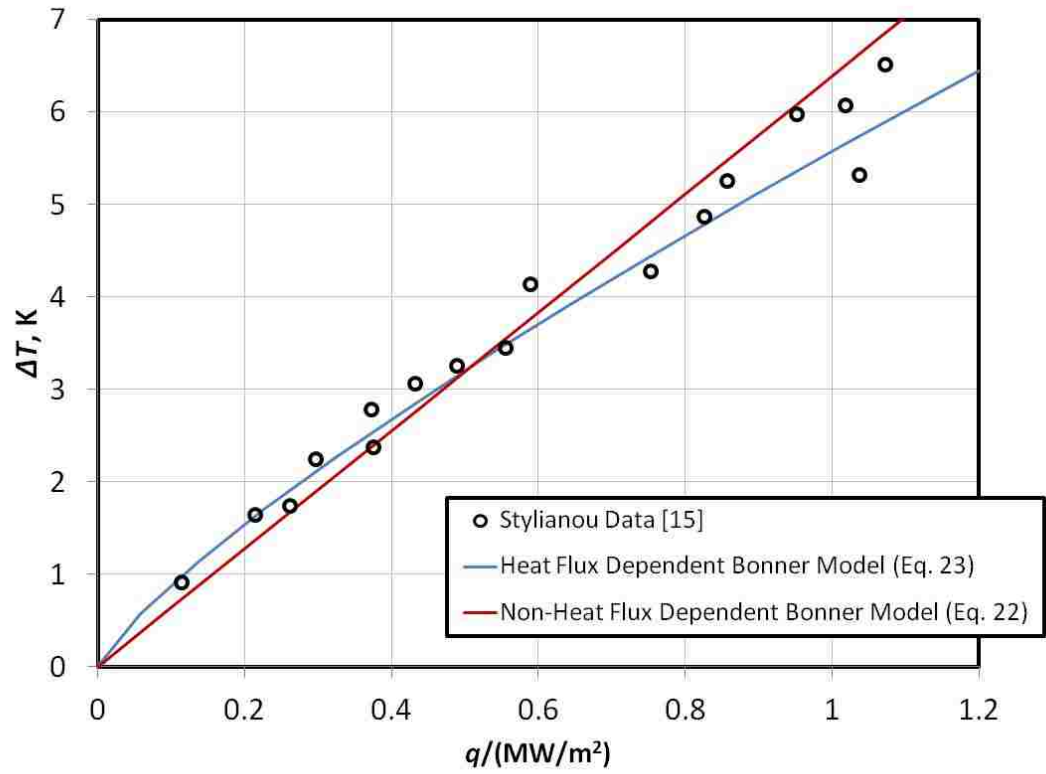


Figure A.5 Predictions from the heat flux and non-heat flux dependent Bonner models are plotted against experimental data acquired by Stylianou for steam at 333K [30].

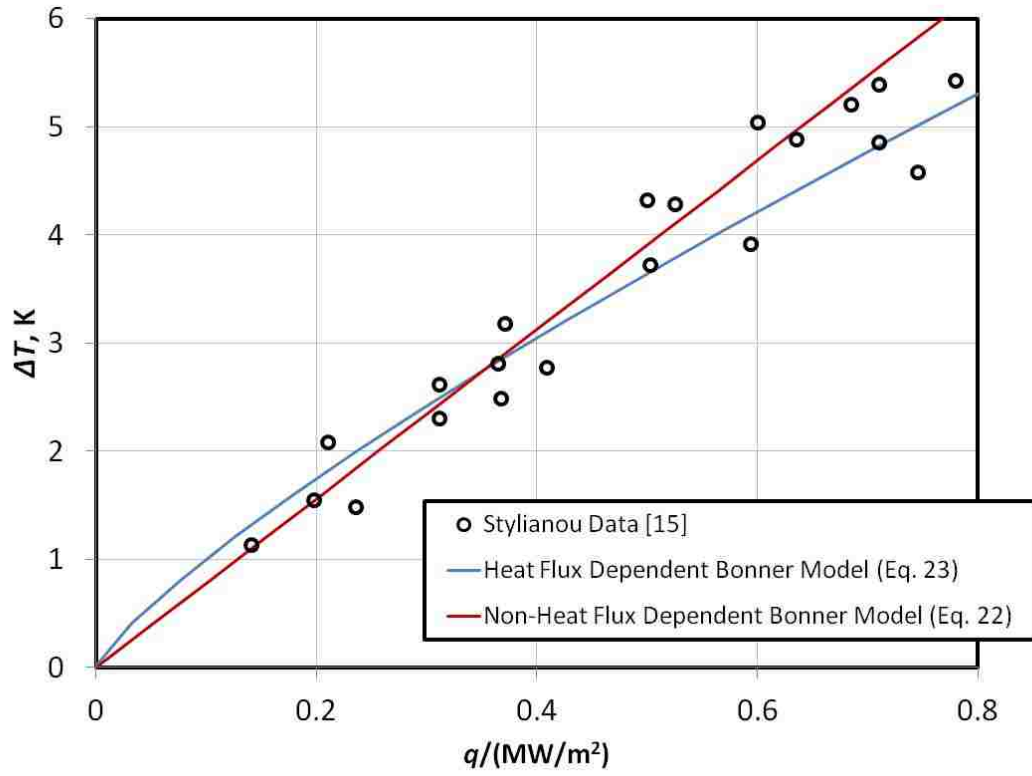


Figure A.6 Predictions from the heat flux and non-heat flux dependent Bonner models are plotted against experimental data acquired by Stylianou for steam at 321 K [30].

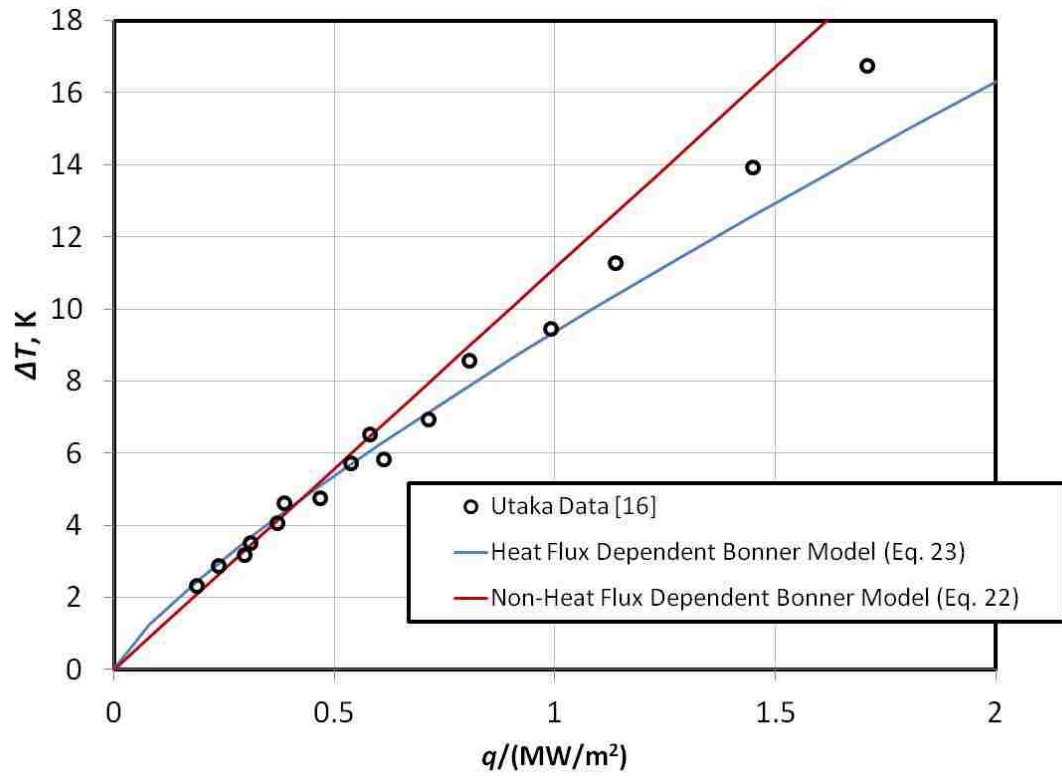


Figure A.7 Predictions from the heat flux and non-heat flux dependent Bonner models are plotted against experimental data acquired by Utaka for ethylene glycol at 428 K [31].

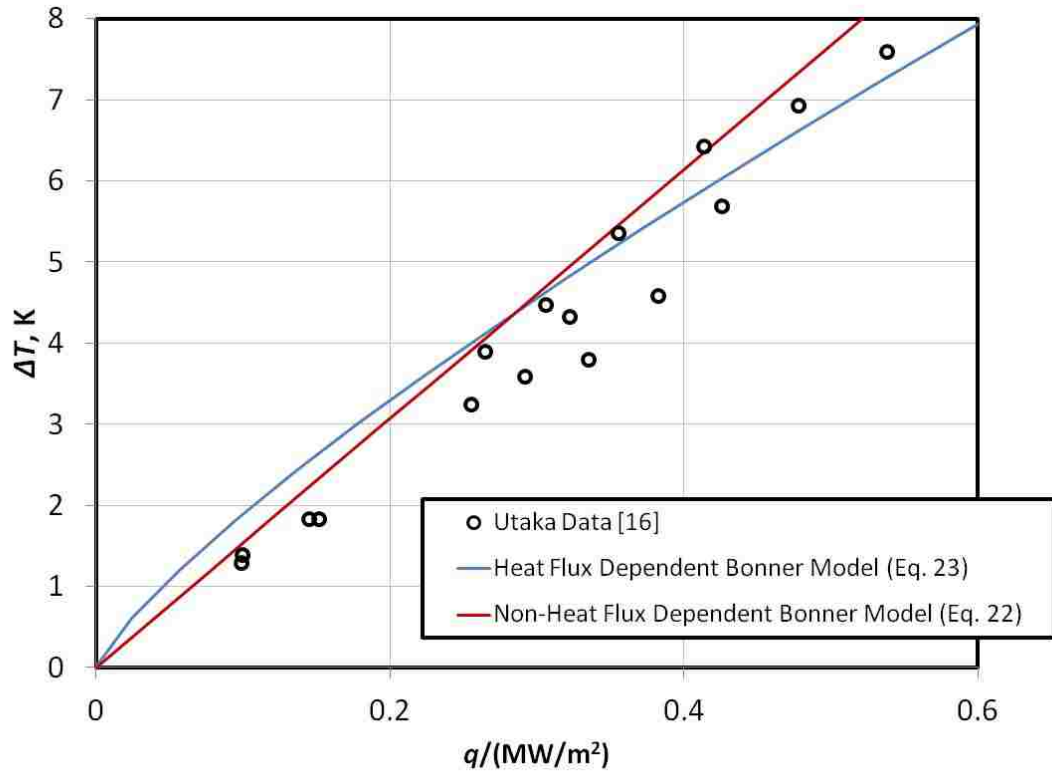


Figure A.8 Predictions from the heat flux and non-heat flux dependent Bonner models are plotted against experimental data acquired by Utaka for propylene glycol at 408 K [31].

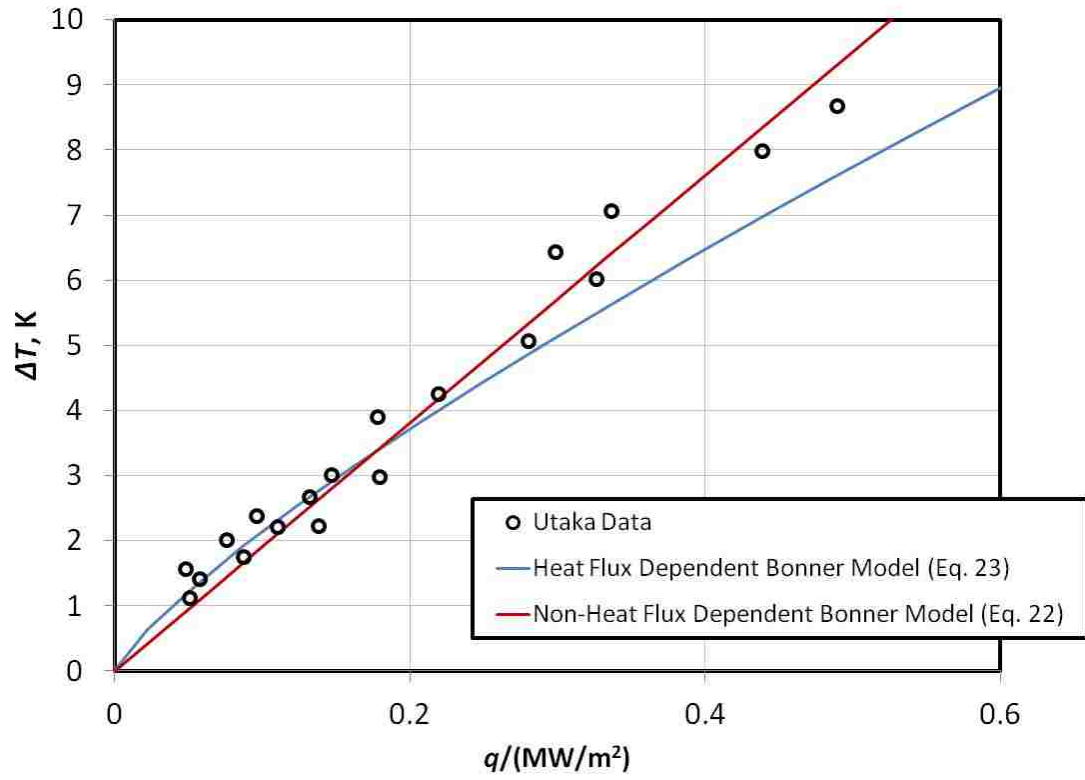


Figure A.9 Predictions from the heat flux and non-heat flux dependent Bonner models are plotted against experimental data acquired by Utaka for propylene glycol at 388 K [31].

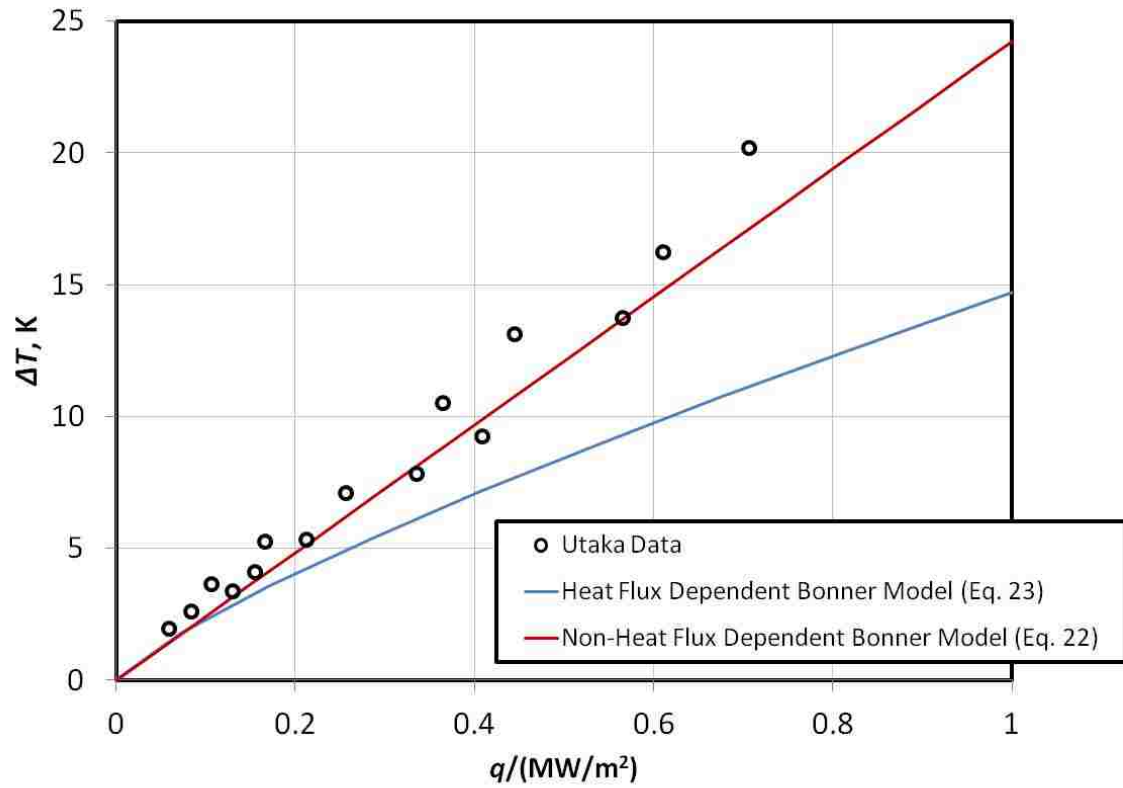


Figure A.10 Predictions from the heat flux and non-heat flux dependent Bonner models are plotted against experimental data acquired by Utaka for ethylene glycol at 368 K [31].

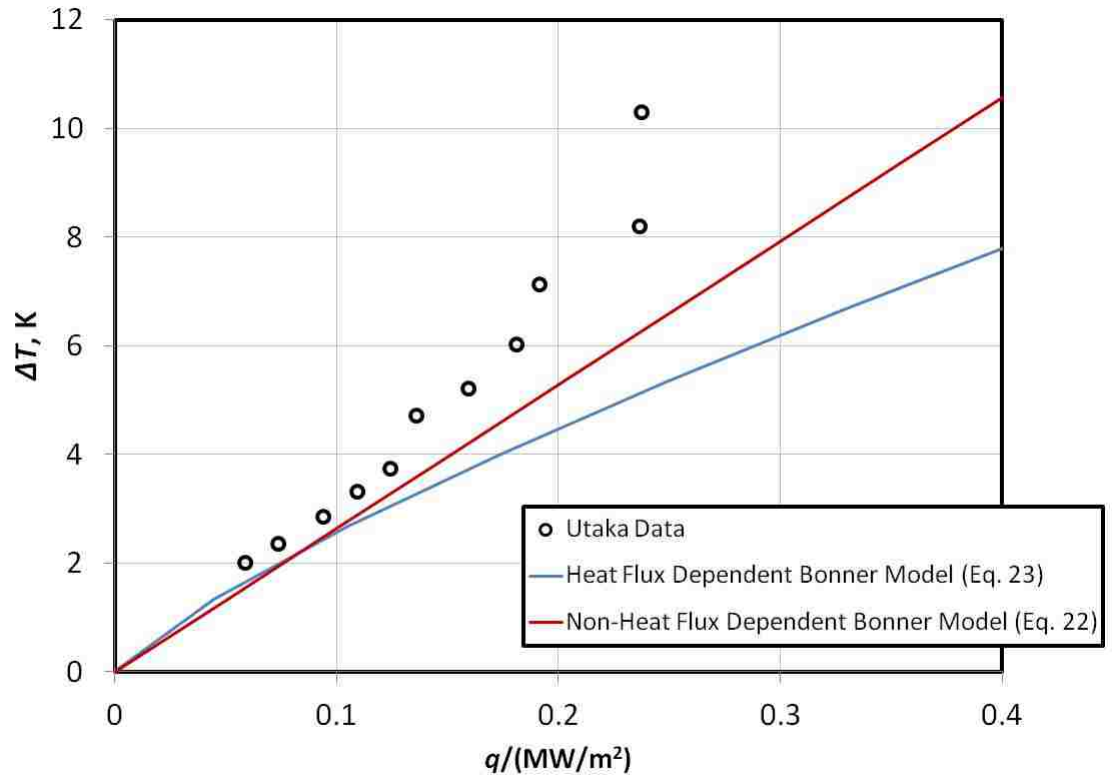


Figure A.11 Predictions from the heat flux and non-heat flux dependent Bonner models are plotted against experimental data acquired by Utaka for propylene glycol at 363 K [31].

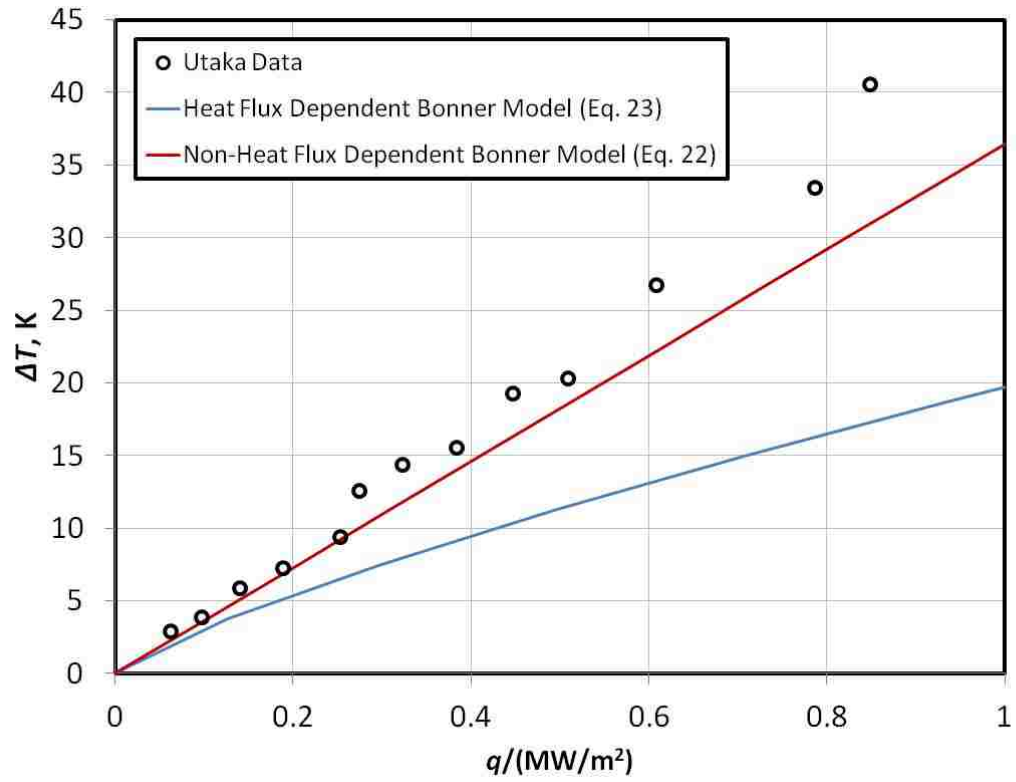


Figure A.12 Predictions from the heat flux and non-heat flux dependent Bonner models are plotted against experimental data acquired by Utaka extracted data for glycerol at 423 K [31].

Biography

Richard William Bonner III was born on November 6, 1982 to Tara and Richard Bonner Jr. in New Brunswick, NJ. He grew up on the Jersey Shore with his sister Dana and brother Bob, and thoroughly enjoyed his summers on the beach. He attended Southern Regional High School in Manahawkin, NJ, graduating in 2001. He ran Cross Country and earned Most Outstanding Player his senior year in baseball. He was a member of the math club and science club, where his greatest achievement was breaking his high school's record for the highest score on the American High School Mathematics Exam. He earned 29 AP credits, which allowed him to graduate from Lehigh's Chemical Engineering program in an accelerated 3 years. At Lehigh he met his wife, Jeanine Bonner, a fellow Lehigh graduate whom he married in May of 2007. He was awarded the Presidential Scholarship which he used to earn a Master's degree. After a few years in industry at Advanced Cooling Technologies, Inc. (ACT), he started his doctoral program after receiving an R&D award through the National Science Foundation, while continuing his employment. He is currently the Manager of Custom Products at ACT, where he leads the development of new and emerging thermal management technologies and products. To date, he has lead over \$6M in government sponsored research projects and co-authored over 20 papers.

Curriculum Vitae

Education

Ph.D. Chemical Engineering, Lehigh University, May 2013

Lehigh University, Bethlehem, Pennsylvania

Dissertation: Advances in heat transfer through coatings and micro-scale features

Advisor: Professor Manoj K. Chaudhury

M.S. Chemical Engineering, May 2007

Lehigh University, Bethlehem, Pennsylvania

Thesis: Heat transfer to viscous fluids

Advisors: Professors John C. Chen and Kemal Tuzla

B.S. Chemical Engineering, May 2004

Lehigh University, Bethlehem, Pennsylvania

Graduated in 3 years with high honors

Work Experience

Advanced Cooling Technologies, Inc., Lancaster, Pennsylvania

Manager, Custom Products, 2012

Lead R&D Engineer, 2008

R&D Engineer, 2005

Astropower, Inc, Newark, Delaware

Summer Intern, 2001

Publications

1. Bonner, R.W.; "Correlation for dropwise condensation heat transfer: Water, organic fluids and inclination," *International Journal of Heat and Mass Transfer*, 2013
2. Lu, K.S.; Pellicone, D.; Bonner, R.; Fleming, E.; Reist, D.; Reber, G.L.; Walker, J.N.; "High-capacity thermoelectric heat exchanger," *Thermal and Thermo-mechanical Phenomena in Electronic Systems (ITherm)*, 2012 13th IEEE Intersociety Conference, pp.78-85, May 30 2012-June 1 2012
3. Desai, T., Piedra, D., Bonner, R., et al., "Novel Junction Level Cooling in Pulsed GaN Devices," *ITherm*, San Diego, CA, May 30, 2012
4. Piedra, D., Desai, T., Bonner, R., et al., "Integration of a Phase Change Material for Junction-Level Cooling in GaN Devices," *Semi-therm*, San Jose, CA, March 2012
5. Fan, A., Bonner, R., et al., "An Innovative Passive Cooling Method for High Performance Light-emitting Diodes," *Semi-therm*, San Jose, CA, March 2012
6. Bonner, R.W.; Weyant, J.; Fleming, E.; Lu, K.; Reist, D.; , "Passivation coatings for micro-channel coolers," *Applied Power Electronics Conference and Exposition (APEC)*, 2012 Twenty-Seventh Annual IEEE , pp.498-502, 5-9 Feb. 2012

7. Bonner, R., et al., March 2011, "Die Level Thermal Storage for Improved Cooling of Pulsed Devices," Semitherm, Santa Clara, Ca.
8. Tang, X., Bonner, R., et al., "A 2-D Numerical Study of Micro-scale Phase Change Material Thermal Storage for GaN Transistor Thermal Management," Semi-therm, San Jose, CA, March 2011
9. Bonner, R., August 2010, "Dropwise Condensation Life Testing of Self-Assembled Monolayers", 2010 International Heat Transfer Conference, Washington, DC.
10. Bonner, R., March 2010, "Dropwise Condensation on Vapor Chambers," 2010, Semi-therm, Santa Clara, Ca.
11. Shin, S., Kaviani, M., Desai, T., Bonner, R., "Roles of Atomic Restructuring in Interfacial Phonon Transport," Physical Review B, 82, 081302 (2010)
12. Bonner, R., July 2009, "Condensation on Surfaces with Graded Hydrophobicity," 2009 ASME Summer Heat Transfer Conference, San Francisco, Ca.
13. Zuo, J., Anderson, W., Bonner, R. "Advanced Thermal Management Technologies for High Power Automotive Equipment," National Defense Industrial Association Ground Vehicle Power and Energy Workshop, Troy, Michigan, November 2008
14. Bonner, R., November 2008, "Passive Heat Exchanger Temperature Control Variable Conductance Heat Pipes," 2008 AIChE Annual Meeting, Philadelphia, Pa.
15. Bonner, R., et al., March 2008 "Local Heat Transfer Coefficient Measurements of Flat Angles Sprays Using Thermal Test Vehicle," 24th IEEE Semi-Therm Symposium, San Jose, California.
16. Hartenstine, J., Anderson, W., Bonner, R., "Titanium Loop Heat Pipes for Space Nuclear Power Systems," Space Technology and Applications International Forum (STAIF), Albuquerque, New Mexico, February 2008
17. Hartenstine, J., Bonner, R., et al., "Loop Thermosyphon Design for Cooling of Large Area, High Heat Flux Sources," InterPACK 2007, Vancouver, Canada, July 2007.
18. Anderson, W., Bonner, R., et al. Intermediate Temperature Fluids Life Tests - Experiments, et al., 2007 International Energy Conversion Engineering Conference, St. Louis, MO, June 2007.
19. Sarraf, D., and Bonner, R., "Passive Thermal Management for a Fuel Cell Reforming Process," 2006 International Energy Conversion Engineering Conference, San Diego, CA, June 2006
20. Anderson, W., Dussinger, P., Bonner, R. et al., "High Temperature Titanium-Water and Monel-Water Heat Pipes," 2006 International Energy Conversion Engineering Conference, San Diego, CA, June 2006.
21. Bonner, R., Chen, J.C., Tuzla, K., 2004 "Heat Transfer to Viscous Solutions," 2004 AIChE Annual Meeting, 198e, Austin, Texas.

Patents

1. U.S. Patent Application - Semiconductor Having Integrally-Formed Enhanced Thermal Management

Government Sponsored R&D Projects

- Die Level Thermal Storage for Temperature Stabilization and Minimization (\$1M) (funded by NRO)
- Condensation on Gradient Surfaces, \$660k (funded by NSF and Sun Microsystems)
- Dropwise Condensation on Hydrophobic Wick Structures \$100k (funded by OSD/ONR)
- Heat Pipe Cooling of Acoustic Transducers \$70k (funded by Navy)
- Stabilization of Nanofluids Using Self-Assembled Monolayers \$875k (funded by DOE)
- Thermoelectric Heat Exchanger for the E-2D Hawkeye \$900k (funded by Navy)
- Dielectric Planar Thermosyphons for LED Cooling \$1.1M (funded by DOE)
- Ceramic Coatings for Corrosion Resistance in Micro-channel Coolers \$900k (DARPA)
- Integrated Thermal Storage and Refrigeration System \$1M (MDA)

Awards

1. APEC Best Presentation Award for "Passivation coatings for micro-channel coolers" February, 2012
2. Lehigh University Presidential Scholarship

Presentations

1. Passivation coatings for micro-channel coolers, 2012, APEC
2. Dielectric Planar Thermosyphons for LED Cooling, 2012, DOE SSL Workshop
3. Die Level Thermal Storage for Improved Cooling of Pulsed Devices, 2011, Semi-therm
4. Dropwise Condensation on Vapor Chambers, 2010, Semi-therm
5. Dropwise Condensation Life Testing of Self-Assembled Monolayers, 2010, International Heat Transfer Conference
6. Condensation on Gradient Surfaces, 2010, SBIR National Science Foundation Grantees Workshop
7. Advanced Coatings for Condenser Enhancement and Corrosion Prevention, 2010, International Two-Phase Spacecraft Thermal Control Workshop
8. Advanced Cooling Systems Inc., 2010, Lockheed Martin SBIR Industry Workshop
9. Condensation on Surfaces with Graded Hydrophobicity, 2009, ASME Summer Heat Transfer Conference
10. Advanced Thermal Management for OTM SATCOM Antennas, 2009, SATCOM Technologies Workshop
11. Passive Heat Exchanger Temperature Control Variable Conductance Heat Pipes, 2008, AIChE
12. Local Heat Transfer Coefficient Measurements of Flat Angles Sprays Using Thermal Test Vehicle, 2008, Semi-therm
13. Heat Transfer to Viscous Solutions, 2004, AIChE